Understanding the p-d and d-p Radiative Capture Reactions Near Threshold Using Polarization Observables

by

Eric A. Wulf

Department of Physics
Duke University

Date

Approved:

Henry R. Weller, Supervisor

Arthur E. Champagne

Ashutosh Kotwal

Patrick G. O'Shea

M. Ronen Plesser

Dissertation submitted in partial fulfillment of
the requirements for the degree of
Doctor of Philosophy in the Department of
Physics in the Graduate School
of Duke University

1999

Abstract

(Physics – TUNL)

Understanding the p-d and d-p Radiative Capture Reactions Near Threshold Using Polarization Observables

by

Eric A. Wulf

Department of Physics
Duke University

Date

Approved:

Henry R. Weller, Supervisor

Arthur E. Champagne

Ashutosh Kotwal

Patrick G. O'Shea

M. Ronen Plesser

An abstract of a dissertation submitted in partial
fulfillment of the requirements for the degree
of Doctor of Philosophy in the Department
of Physics in the Graduate School
of Duke University

1999

Abstract

Understanding the p-d and d-p Radiative Capture Reactions Near Threshold Using Polarization Observables

The ^{2}H$(\vec{\mathrm{p}},\gamma)^3$He and ^{1}H$(\vec{\mathrm{d}},\gamma)^3$He reactions have been examined in the energy range of E_p(lab) = 40-0 keV and E_d(lab) = 80-0 keV ($E_{c.m.}$ = 26.7-0 keV). The cross-section, $\sigma(\theta)$, the vector analyzing power for ^{2}H$(\vec{\mathrm{p}},\gamma)^3$He, $A_y(\theta)$, the vector analyzing power for ^{1}H$(\vec{\mathrm{d}},\gamma)^3$He, $iT_{11}(\theta)$, the tensor analyzing powers, $T_{20}(\theta)$, $T_{21}(\theta)$, and $T_{22}(\theta)$, the γ-ray polarization, P_γ, and the γ-ray polarization analyzing power, A_γ were all measured. This experiment is an extension of the work started by [Sch95, Sch97]. The primary goal of this work is to extract the Transition Matrix Elements (TMEs) underlying the reaction to high precision and to use them to examine the physics of the three-body system. The determination of the TMEs will allow comparisons to the recent theoretical work of Viviani *et al.* [Viv96] who calculated the TMEs for this reaction. The calculated values of $A_y(\theta)$ reveal the "A_y Puzzle" where the theory undercalculates $A_y(\theta)$ by about 30% at 90°. The TMEs determined by the experiment will also allow calculation of interesting quantities such as the quartet to doublet ratio of the magnetic dipole terms, which is sensitive to Meson Exchange

Currents. The D- to S-state asymptotic ratio, which is sensitive to the tensor force, can also be determined. Finally, the Gerasimov-Drell-Hearn sum rule integral can be evaluated in the vicinity of threshold and compared to theoretical predictions.

Acknowledgements

I could not have finished this project without help from many sources. If it were not for the all of the groundwork done by Greg Schmid in his thesis I would probably still be writing now. His attention to detail and writing skills are greatly appreciated. My advisor, Henry Weller, has helped me throughout my career at Duke and has helped me make sense of what is happening. The Capture group in all of its incarnations over the past few years has been indispensable. Mark Godwin, Bryan Rice, Eric Schreiber, Shane Canon, Konstantin Sabouro and Steve Nelson helped with many shifts and many laughs. Chip Laymon, John "Ned" Kelley, and Sally Gaff have been great helps as post-docs for the group. They have always had good ideas and have contributed down in the lab. Dick Prior has always been available for advice and is "Mr. Fix-it" on experiments. If something needs to be built for an experiment, you can always count on him. Last but not least, Ron Tilley has always been there for the group, listening to our talks, sitting shifts, and offering help.

I would like to thank my parents because without their patience and help I would not be where I am now. And last, but not least, I would like to thank Christiane Meyer who has helped to make the past few months, if not quite fun, than at least bearable.

Contents

List of Figures

List of Tables

Chapter 1

Introduction

A detailed study of ^{2}H($\vec{\mathrm{p}}, \gamma$)^{3}He and ^{1}H($\vec{\mathrm{d}}, \gamma$)^{3}He radiative capture reactions at E_p(lab) = 40-0 keV is presented in this thesis. This study was first motivated by successful *ab initio* three-body calculations of the ^{2}H(p, γ)^{3}He reactions that include explicit Meson Exchange Currents (MECs) and a full treatment of the Coulomb interaction [Fri91, Viv96]. Further motivation came from interest in a determination of the astrophysical S-factor at thermal energies for use in astrophysics, investigation of meson exchange current effects, and determination of the transition matrix elements for use in calculating other interesting physical quantities.

1.1 Background

A radiative capture reaction occurs when the incident particle is "captured" by the target nucleus with the emission of electromagnetic radiation: γ-rays. In the present case of the ^{2}H(p, γ)^{3}He reaction, the incident particle's spin, s, couples with

the relative angular momentum of the proton and deuteron, ℓ, to form the total single particle angular momentum, j. The complex transition matrix element (TME) is defined as $\mathrm{T} = \langle \Psi_f | \mathrm{H} | \Psi_i \rangle$ where Ψ_f is the final state wavefunction, Ψ_i is the initial scattering state wavefunction, and H is the interaction Hamiltonian responsible for the transition. All of the experimental observables can be expanded in terms of the TMEs of the reaction. Each TME is specified by the s, ℓ, and j of the initial scattering state and the multipolarity of the electromagnetic transition to the final state. The current experiment uses six TMEs described in Table 6.2. Determining the TMEs for the reaction reveals the physics underlying the reaction and allow for comparison to theoretically calculated TMEs.

The three-body theoretical calculations are carried out using nucleon-nucleon, NN, potentials (see Section 2.1.1) that are determined by fitting all of the available two-body NN data. The calculations also include three-body forces to correct for the underbinding of the bound state of ^{3}He and ^{3}H predicted by NN potentials alone.

The electromagnetic operator H is given by

$$H = -\frac{1}{c} \int \vec{J}(\vec{r}) \cdot \vec{A}(\vec{r}) d\vec{r} \tag{1.1}$$

where $\vec{J}$ is the nuclear current density, $\vec{A}$ is the vector potential in the radiation gauge, and $\vec{r}$ is the relative position vector of the two particles. This operator can be expanded into multipoles of which the dominant terms are electric dipole (E1), magnetic dipole (M1), and electric quadrapole (E2). The nuclear current density for electric radiation can be replaced by the charge density using Siegert's theorem. There is no similar simplification for magnetic radiation.

When the cross section for np and other NN scattering reactions is calculated, the cross section at energies in the 1 through 30 MeV region is dominated by electric

radiation. The electric terms are calculated using Siegert's theorem so the effect of meson exchange currents, the exchange of π, ρ, and ω mesons between two nucleons, is not explicitly seen. When the cross section of np scattering is calculated at thermal energies using only the electromagnetic operator acting on one nucleon, the impulse approximation, it is underpredicted by 10%. As will be discussed in Section 2.2, this 10% discrepancy was corrected by the addition of explicit meson exchange currents (MECs) in the magnetic radiation terms [Fri90]. This was the first time that effects from MECs were able to be explicitly calculated and observed [Fri90].

1.2 Motivation

Stringent tests of three-body theoretical calculations done at these energies require precision experimental determination of the observables for these reactions. Nuclear astrophysicists are also interested in these reactions because they play a central role in the stellar proton-proton chain and protostellar evolution [Rol88].

Deuterium is produced in a star by fusion of two protons, but this reaction is a weak reaction because it produces a positron and neutrino along with the deuteron. The ^{2}H(p, γ)^{3}He reaction occurs due to the electromagnetic interaction and is therefore much more likely. It is also the next step in the proton-proton chain, but its rate has almost no effect on stellar energy production because it is "bottlenecked" by the production of deuterium by the weak interaction.

The ^{2}H(p, γ)^{3}He reaction plays a more important role in protostellar evolution, the collapse of interstellar gas to eventually form a star. The first nuclear reaction to occur in this collapse is the burning of primordial deuterium, deuterium produced by the Big Bang, in the ^{2}H(p, γ)^{3}He reaction. The burning has the effect of acting

like a thermostat and maintaining the temperature in low mass protostar of about 10^6 K, the threshold temperature for the reaction [Sta88]. This places a constraint on the mass-radius relation for the protostar which in turn constrains the stellar birthline, the locus of points on a luminosity vs. surface temperature curve where protostars first become luminous. The theoretical development of the stellar birthline is based partly on the determination of the cross section of the ^{2}H(p,γ)^{3}He reaction at thermal energies. The typical manner used to determine the cross section at thermal energies is to measure the cross section at higher energies and then extrapolate to thermal energies using the astrophysical S-factor. The S-factor (see Equation 4.5) removes the Coulomb dependence of the cross section and is assumed to be linear as a function of energy away from resonances. Therefore, accurate determination of the cross section at low energies and extrapolation to thermal energies is needed.

Another motivation for the experiment is that there are large contributions to the cross section at low energies by s-waves, ℓ=0. For the ^{2}H(p,γ)^{3}He and ^{1}H(d,γ)^{3}He reactions, s-wave radiative capture produces magnetic dipole, M1, radiation which is dominated by Meson Exchange Currents (MECs). The M1 transitions are dominated by MEC because the normally dominant one-body operator is greatly diminished by the orthoginality of the initial and final state (see Section 2.1.3). Given s-wave, ℓ=0, capture for this reaction you have two possibilities for the total spin; j=1/2 or 3/2. The relative strength of these two components is determined by MEC. Therefore, determinations of the s-wave strengths at low energies will enable us to study MEC effects.

Another interesting feature of the ^{2}H(p,γ)^{3}He and ^{1}H(d,γ)^{3}He reactions below the breakup threshold of deuterium, E_p(lab) $\leq$ 3.33 MeV, is that Watson's theorem can be employed (see Section 1.5.1). Watson's theorem allows the elastic scattering

phases to be related to the phases of the TMEs for the capture reaction. This is because at low energies the only allowed reaction channels are elastic scattering and radiative capture. This can be used to simplify the analysis of the data, as will be shown later.

Finally, the measured observables can been used for determination of the Transition Matrix Elements (TMEs) found in this reaction and these can then be used to calculate other interesting physical quantities and for a detailed comparison with theoretical predictions.

1.3 Previous Measurements

There are two previous measurements of the ^{2}H(p, γ)^{3}He reaction at low energies E$_p$(lab) $<$ 50 keV, one by Griffiths *et al.* [Gri63] and one by Schmid *et al.* [Sch95, Sch97]. The experiment performed by [Gri63] was a determination of the cross section as a function of energy at low energies. The measured cross section data determines the astrophysical S-factor using Equation 4.5. An extrapolation of the S-factor to zero energy was performed but, since the experiment was not accurate enough to determine the slope of the S-factor, the slope was taken from direct capture theory (see Figure 1.1). A verification of these conclusions was the main motivation behind the Schmid *et al.* [Sch95, Sch97] experiment. It measured the cross section, the vector analyzing power (the left-right asymmetry in cross section when measuring the reaction with a vector polarized proton beam, see Section 4.2 and Section 3.1), and the γ-ray polarization of this reaction (see Section 5.1). The cross section was determined as a function of energy by binning the accumulated γ-ray spectrum as a function of energy as well as by a continuous deconvolution procedure (see Section 4.3.1). Using this

data, an extrapolation of the S-factor to zero energy was accomplished (see Figure 1.1) in a completely model independent manner.

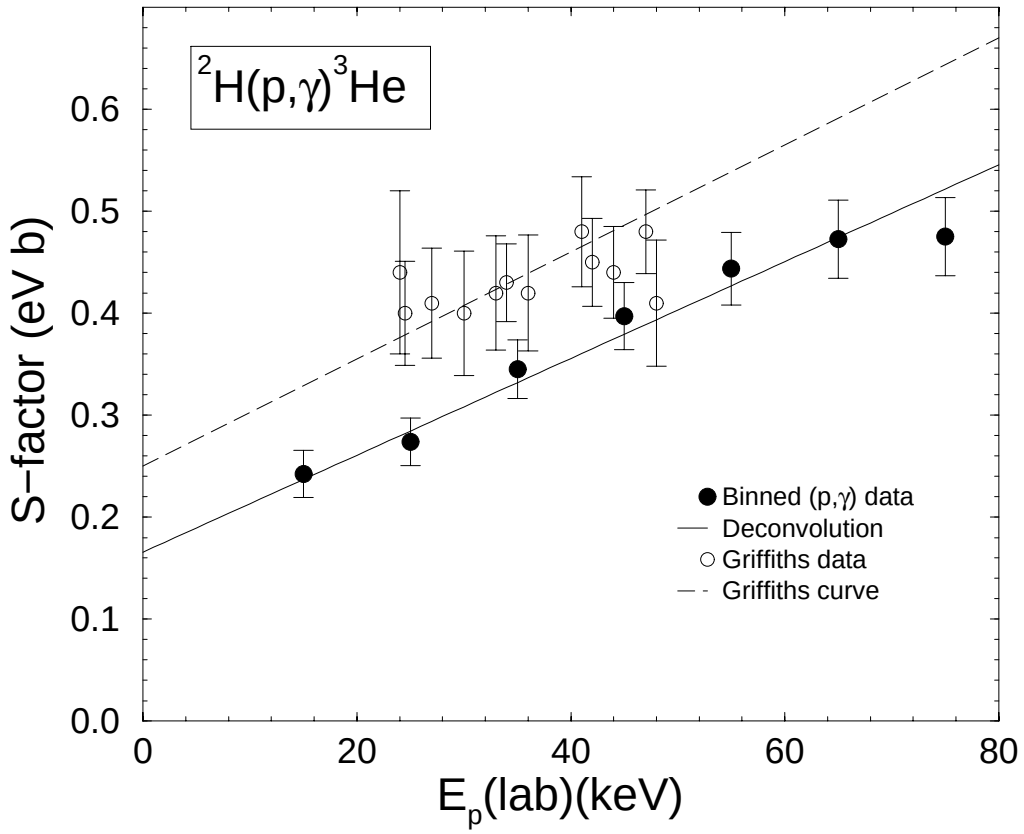

Figure 1.1: The astrophysical S-factor as determined by Schmid *et al.* [Sch97] and Griffiths *et al.* [Gri63]. The extrapolated S-factor at zero energy is reduced from [Gri63] by about 25%.

The vector analyzing power, $A_y(\theta)$, for $^2\mathrm{H}(\vec{\mathrm{p}},\gamma)^3\mathrm{He}$ was also determined as a function of angle and energy. That, combined with angular distribution data for the cross-section, yielded the magnetic dipole (M1) strength as a function of energy. The γ-ray polarization was also measured, which helped to determine the M1 strength, although this information was never determined as a function of energy due to limited

statistics. Finally, the tensor analyzing power, $T_{20}(\theta)$, for $^1H(\vec{d},\gamma)^3He$ reaction was measured. $T_{20}(\theta)$ (see Section 4.4.2) is the difference in cross section for tensor polarized beams (see Section 3.1) that have spin projections parallel and anti-parallel to the spin symmetry axis (set along the beam direction). From this the asymptotic D- to S-state ratio was determined [Ric97a] (see Section 1.5.4).

The previous experiment [Sch95, Sch97] left room for improvement. More precise data on the measured observables was called for, as well as new data. The observables that needed to be measured included the vector analyzing power for a vector polarized deuteron beam, iT_{11} (see Section 4.4.1), the other tensor analyzing powers, T_{21} (see Section 4.4.3) and T_{22} (see Section 4.4.4), and the γ-ray polarization analyzing power which is the difference in γ-ray polarization for a protons polarized in opposite directions (see Section 5.2). One can expand all of the measured observables in terms of TMEs and one can fit the observed data to determine the TMEs underlying the reaction. The data set collected in [Sch97] was not sufficient to determine the strength of all of the M1 and E1 TMEs. The TME fit to the data of Schmid *et al.* [Sch97] only included one p-wave, ℓ=1 (E1), and one s-wave, ℓ=0 (M1), TME and a relative phase between them.

Rice *et al.* [Ric97b] added measurements of the $^2H(\vec{p},\gamma)^3He$ reaction's vector analyzing power, $iT_{11}(\theta)$. This allowed the s-wave TME to be broken into an M1 doublet (s=1/2 and j=1/2) and M1 quartet (s=3/2 and j=3/2) term so that their cross section ratio could be determined and compared to theory (see Section 1.5.3).

1.4 Current Experiment

The current experiment is a continuation of [Sch95] which includes measurements of the tensor analyzing powers for the inverse ^{1}H(d, γ)^{3}He reaction, the γ-ray Polarization Analyzing Power, and new data points in previously measured observables. The main goal is to acquire a complete and accurate data set of all the observables for the ^{2}H($\vec{\mathrm{p}}, \gamma$)^{3}He and ^{1}H($\vec{\mathrm{d}}, \gamma$)^{3}He reactions in order to provide a stringent test bed for recent and emerging three-body calculations. These other observables will also allow a Transition Matrix Element (TME) analysis that would determine more TMEs in a free fit than the two TMEs used by Schmid *et al.* [Sch95, Sch97] or the constrained fit done in [Ric97b]. From the TMEs fit to the experimentally measured observables, other interesting quantities can be calculated.

1.5 Interesting Topics and Quantities

Accurate determination of the TMEs for the reaction allows not only an examination of the physics underlying the reaction, but also a look at other quantities and topics of interest. Watson's theorem relates the phases determined from elastic scattering to the phases of the TMEs for the capture reaction. Using Watson's theorem for our analysis allows us to constrain the phases of the TMEs to those determined by elastic scattering which allows for a more physical result and smaller uncertainties in the TME amplitudes. The "$A_y(\theta)$ Puzzle" is the inability of modern three-body calculations to describe the experimentally measured vector analyzing power even though the calculations can reproduce the other measured observables. The puzzle also exists for these capture reaction and is a topic that will be examined. Quantities to be calculated include the ratio of the Doublet to Quartet M1 strengths, the

asymptotic D- to S-state ratio, and the Gerasimov-Drell-Hearn sum rule integral, as described in the next few sections.

1.5.1 Watson's Theorem

In 1954, Watson [Wat54] shows that the phases of the capture reaction are simply related to the phase shifts from elastic scattering. This relationship is based on the unitarity of the S-matrix and time-reversal invariance. The phases for the capture reaction are the phases, ϕ, of the TMEs, $|R|e^{i\phi}$. For elastic scattering, the observables can be expanded in terms of phase shifts and then the phase shifts can be determined by fitting them to the measured data. At low energies, where the only inelastic channel open is radiative capture, the scattering phase shifts and the mixing between the different scattering amplitudes, specified by so-called mixing parameter in the phase shift analysis, give the phases of the capture TMEs. This allows a simplification of the fitting to the data. At the energies of the current experiment, the mixing of the ℓ and s quantum numbers are negligible. As a further verification of this, theoretical calculations of the mixing between states with the same s and different j show negligible mixing. Therefore, the difference between the scattering phase shifts give the relative phases of the capture TMEs. As an example, suppose that the M1 s=1/2 and the M1 s=3/2 scattering phases are 1° and 11° respectively. The capture TME phases will differ by 10° as well, but the actual phase angle is arbitrary because all of the capture observables use only the differences between TME phases.

Unfortunately, there is no scattering data taken at our energies since Coulomb repulsion makes it nearly impossible. Therefore, the only phase analysis has to come from theoretical calculations of the scattering phase shifts. Using the theoretically calculated phases can reduce the number of free parameters by a factor of two by

eliminating the need to fit the phases of the TMEs [Knu99]. This is only true if one believes that the theoretical calculations of the phases are accurate. In the present case, however, the phase shifts due to the nuclear force are extremely small ($\leq 0.5^\circ$) while the fit to the data is only sensitive enough to determine the TME phases to at most 3°. Therefore, even if the theory is off by a factor of six we would still not be sensitive to it. The dominant effect in the phase arises from the Coulomb effect which gives a relative phase between the s- and p-waves of 42° at $E_p(\text{lab}) = 31$ keV.

1.5.2 "$A_y(\theta)$ Puzzle"

The vector analyzing power puzzle is the inability of full three-body calculations to reproduce the experimentally determined vector analyzing power data for a nucleon scattering off a deuteron, Nd. The same calculations can reproduce the cross section and tensor analyzing powers (see Section 4.4), but not the vector analyzing power (the left-right difference in cross section to a vector polarized proton or neutron beam, see Section 4.2). In fact, in the years since the first calculations, no three-body calculations have been able to predict $A_y(\theta)$ for Nd scattering below 30 MeV. This is shown in Figure 1.2 which is from [Tor98a]. The deuteron vector analyzing power, iT_{11}, for a vector polarized deuteron scattering off a nucleon, also shows a large discrepancy between theory and data. The same discrepancies in the vector analyzing powers and agreements in the cross section and tensor analyzing powers have been seen in low energy capture in the $^2\text{H}(\vec{\text{p}},\gamma)^3\text{He}$ and $^1\text{H}(\vec{\text{d}},\gamma)^3\text{He}$ reactions [Sch97, Ric97a].

This puzzle and some possibilities for solutions are discussed in detail in [Hüb98]. For elastic scattering data, the cross section and other observables can be expanded in terms of the phase shifts of the reaction. The phase shifts can be determined by

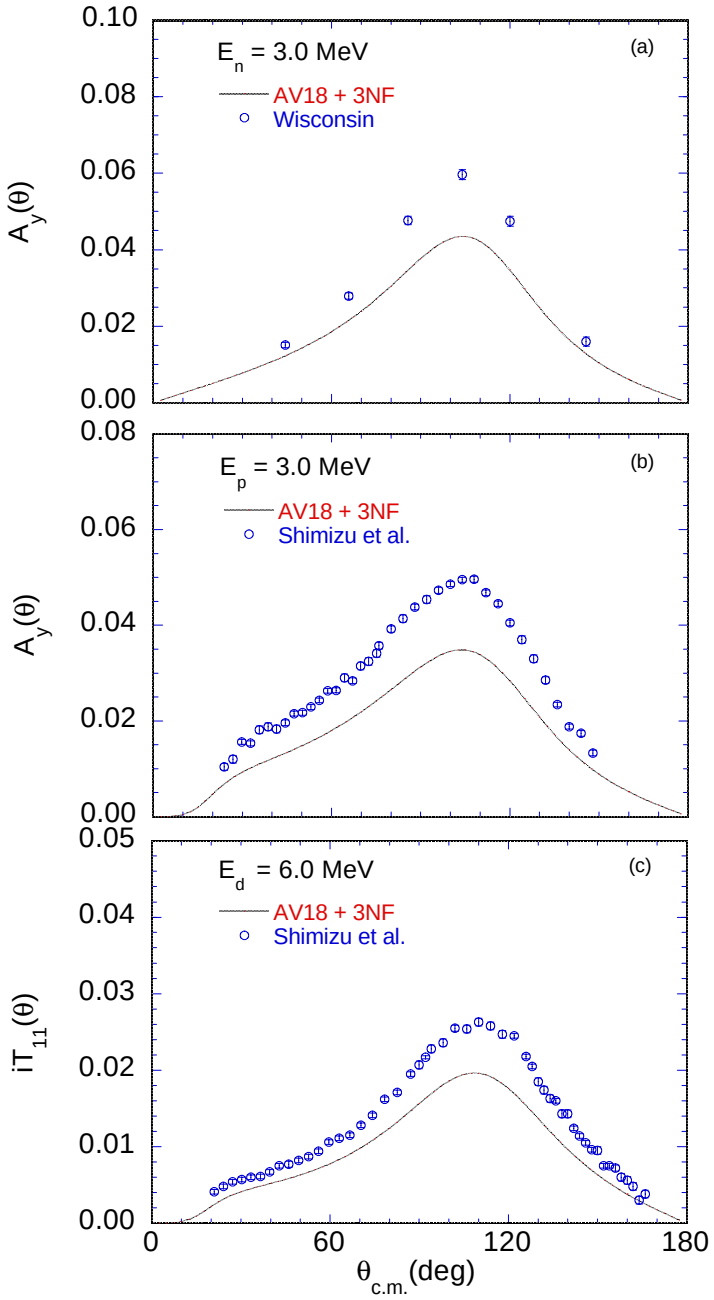

Figure 1.2: The analyzing power puzzle: (a) Comparison of rigorous three-body calculations [Kie95] and data [McA94] for the n-d analyzing power $A_y(\theta)$ at $E_n = 3$ MeV; (b) Comparison of rigorous three-body calculations [Kie95] and data [Shi95] for the p-d analyzing power $A_y(\theta)$ at $E_p = 3$ MeV; (c) Comparison of rigorous calculations [Kie96] and data [Shi95] for the deuteron vector analyzing power $iT_{11}(\theta)$. In the calculations the Argonne v_{18} (AV18) NN potential and the Urbana three-nucleon force (3NF) is used [Wir95].

finding the phase shifts that yield the best fit to the data. The theoretical calculations of these three-body phase shifts are done using a nucleon-nucleon, NN, potential (see Section 2.1.1) that is determined by fitting all of the two-body NN data. $A_y(\theta)$ for pd scattering is found to be most sensitive to the ^4P_j, s=3/2 and ℓ=1, phase shifts. The question becomes: can these phases be changed enough to account for the differences in $A_y(\theta)$ without changing the two-body NN potential's ability to fit the two-body data from which it was derived? The conclusion reached by [Hüb98] is that the NN potential can not be changed in such a way that the it reproduces both $A_y(\theta)$ and the two-body data. They therefore conclude that explicit three-body effects must be examined to solve the puzzle.

The current experiment should allow us to investigate which TMEs are causing the "$A_y(\theta)$ Puzzle" for the capture reaction. And, in the future, this should allow the testing and improvement of theoretical models.

1.5.3 Doublet to Quartet Strength (MEC)

The M1 s-wave s=1/2, doublet, to s=3/2, quartet, strength in the $^2H(p,\gamma)^3He$ reaction has been a topic of great debate over the past 40 years and is discussed by Friar *et al.* [Fri91]. In 1960, it was argued by Cohen, Judd, and Riddell [Coh60] that the quartet, s=3/2, s-wave state did not contribute to the capture reaction. The so called "no-quartet theorem", argued that the spin of the nucleons in the quartet state are aligned and that the Pauli principle forbids the protons from being in a relative s-wave state. In truth, this argument is true only if one neglects the mixed-symmetry components of the quartet state [Fri91]. Unfortunately, the paper was influential and analysis of data was done without inclusion of the quartet state. This became important in the study of muon-catalyzed fusion which was first discussed

in [Fra47] and later measured by [Alv57]. Precision studies of the μ-p-d fusion cycle were carried out by [Pet91]. This experiment employed the Wolfenstein-Gerstein effect [Ger61] which allows one to vary the amount of s=1/2 and s=3/2 spins prior to fusion by varying the deuterium concentration. This allows the experimenter to separate out the doublet and quartet fusion rates. Accurate atomic calculations [Mat61] disagree with the experimental results if the "no-quartet theorem" is true. This is called the Wolfenstein-Gerstein anomaly which was resolved by [Fri91]. Their calculations [Fri91] of the fusion rates for the doublet $0.37(1) \times 10^6$ sec^{-1} and for the quartet $0.107(6) \times 10^6$ sec^{-1} agree well with the experimental values of [Pet91] for the doublet $0.35(2) \times 10^6$ sec^{-1} and for the quartet $0.11(1) \times 10^6$ sec^{-1}. Furthermore, [Fri91] showed that the quartet capture is dominated by the Impulse Approximation (the electromagnetic operator affecting only one of the interacting nucleons) while the doublet capture has strong contributions from meson exchange currents (the two nucleons interacting by exchange of mesons).

In a paper published by Rice *et al.* [Ric97b], a determination of the ratio of quartet to doublet cross section strength was performed from the measurement of the ^{2}H$(\vec{\mathrm{p}},\gamma)^3$He and ^{1}H$(\vec{\mathrm{d}},\gamma)^3$He reactions. A TME fit to the experimentally measured $\sigma(\theta)$, $\mathrm{A}_y(\theta)$, $i\mathrm{T}_{11}(\theta)$, and $\mathrm{T}_{20}(\theta)$ data was performed. These measurements were carried out at $\mathrm{E}_{c.m.} = 27$-0 keV, but the measured doublet to quartet ratio is expected to be similar to that measured in the fusion reactions at thermal energies. This is because of calculations done by [Viv96] which show that the ratio is nearly constant in this energy regime.

The previous fit to the data of Rice *et al.* [Ric97a] was done with six TMEs (the same ones discussed in Section 6.2.1) with the constraint that the phase of the M1 s-wave TMEs are equal [Ric97a]. This yielded a ratio of s=3/2 to s=1/2 M1 cross

section strength of 0.49 ± 0.04. The calculated ratio by Friar *et al.* [Fri91] at thermal energies is 0.58. The calculations of [Viv96] (see Section 2.3) found for AV18/IX a ratio of 0.512 and that AV14/VIII gives a ratio of 0.456. The AV14 nucleon-nucleon potential has a stronger tensor force component than the AV18 NN potential which increases the doublet strength which decreases the ratio. Energy weighting the values calculated from AV18/IX [Viv96] (see Section 6.3.1) from $E_{c.m.} = 0$ to 27 keV yields a value of 0.48 which agrees with the value obtained from experiment. The ratio is strongly affected by two-body currents as shown by the value of 1.95 calculated by [Viv96] for the Impulse Approximation (no two-body currents).

The experimentally determined values [Ric97a] of the TME amplitudes can be converted to cross sections using the information from [Sch97]. The values are for doublet M1 capture 13.77 ± 0.66 nb and for quartet M1 capture 6.74 ± 0.44 nb. This agrees with the values calculated by [Viv96] which were 14.6 nb and 6.9 nb.

The current experiment's more detailed data set should allow for a completely unconstrained fit to the data and an even more accurate determination of the ratio.

1.5.4 D-State Mixing

The tensor force in nucleon-nucleon interactions is one of the central issues in understanding nuclear reactions. For the three-nucleon system, the observable η, the asymptotic D- to S-state ratio, is directly related to the tensor force. As discussed in [Ric97a], the value of η can be determined from $T_{20}(\theta)$. The reason $T_{20}(\theta)$ is sensitive to the D-state is discussed in [Wel88] and below.

The asymptotic form of the bound state of ^{3}He is given below when the system is treated as proton or deuteron separated by a distance, r, and having orbital angular

momentum, ℓ. The D-state is for ℓ=2 and the S-state for $\ell = 0$. From the solution of the Schrödinger equation including the Coulomb potential, the radial portion of the proton-deuteron wave function, $u_\ell(r)$ in the limit of $r \to \infty$ [Fri82] is given by

$$u_\ell(r) \underset{r\to\infty}{\longrightarrow} C_\ell^C N_W \frac{W_{-\kappa,\ell+1/2}(2\beta r)}{r}, \tag{1.2}$$

where $W_{-\kappa,\ell+1/2}$ is a Whittaker function. The Coulomb parameter, κ, is given by

$$\kappa = \frac{2M}{3\beta}\alpha \tag{1.3}$$

where the wave number, β, is given by

$$\beta^2 = \frac{4}{3}M\left[B(^3\mathrm{He}) - B(^3\mathrm{H})\right] \simeq 0.1766 fm^{-2}. \tag{1.4}$$

The zero-range asymptotic normalization, N_W, is defined by

$$N_W^{-2} = \int_0^\infty \left[W_{-\kappa,\ell+1/2}(2\beta r)\right]^2. \tag{1.5}$$

C_ℓ^C is the ℓ-wave Coulomb asymptotic normalization constant. Therefore, the asymptotic D- to S-state ratio, η is defined to be C_D^C/C_S^C. The D-state arises from non-central forces and its strength provides information about the tensor force in the nuclear interactions.

The formalism for spherical tensor analyzing powers, T_{20}, T_{21}, and T_{22} (see Section 4.4), involves a Racah coefficient W(xsxs′;a2), where s and s′ correspond to the values of the total (channel) spin of the state, x is the spin of the projectile, and a is the spin of the target. The formalism for the tensor analyzing powers involve products of pairs of TMEs one having s and the other s′, with s and s′ taking on all of the allowed values of the total channel spin. This coefficient is zero, and the same is therefore true for all spherical tensor analyzing powers, unless s, s′, and 2 triangulate. For pure electric dipole (E1) radiation, Δs=0, neglecting the small spin-dependent

part of the E1 operator. The simplest p+d model of the ground state of ^{3}He is the S-state given by $\ell = 0$, s=1/2, $j^\pi = 1/2^+$. This means that for capture to this S-state, E1 s=1/2 radiation will dominate. This type of capture is expected to give a zero value for $T_{20}(\theta)$ because s, s′, and 2 do not triangulate. For the D-state ground state with $\ell = 2$, s=3/2, $j^\pi = 1/2^+$ we expect the E1 s=3/2 radiation to dominate which is expected to give a non-zero value for $T_{20}(\theta)$ since (s=1/2, s′=3/2 or s=3/2, s′=1/2 or s=3/2, s′=3/2) s, s′, and 2 triangulate. Capture to the S-state and D-state components of the ground state should interfere (1/2,3/2 or 3/2,1/2 from above) to produce a non-zero value of $T_{20}(90°)$. The M1 doublet and quartet s-wave terms can capture to both of these ground state components as well. Therefore, the E1 s=1/2, s=3/2 and the M1 doublet (s=1/2) and quartet (s=3/2) TMEs interfering should be the main contributors to T_{20}.

The asymptotic form of the ground state wave function can be used for the study of the D-state because at the low energy of the present experiment the capture actually occurs at large distances. This means that the wave function is relatively insensitive to the details of the nuclear force [Arr84] and the extraction of η is model independent. It has also been shown that T_{20} scales linearly with η [Fri82].

The method for determining η is described in Section 6.7. Using this method the final value determined by [Ric97a] was $\eta = -0.0399 \pm 0.0091^{+0.0012}_{-0.0019}$. This compares well with the distorted-wave Born approximation extraction of $\eta = -0.0386 \pm 0.0046 \pm 0.0012$ from [Aye95]. Friar *et al.* [Fri88] also calculated $\eta = -0.0430 \pm 0.001$ using a full three-body Faddeev calculation.

The increased data set of this experiment should allow a more accurate determination of this value.

1.5.5 Gerasimov-Drell-Hearn Sum Rule

Studies of the spin dependent structure functions in deep inelastic scattering have raised interest in measurements to determine the accuracy of the Gerasimov-Drell-Hearn (GDH) Sum Rule [Are88, Ack98]. From the data gathered in this experiment, a determination of the GDH sum rule for $^3\vec{\mathrm{H}}\mathrm{e}(\vec{\gamma},\mathrm{d})\mathrm{H}$ in the vicinity of threshold will be possible. The sum rule relates the following

$$\mathrm{I}_{GDH} = \int_{\mathrm{E}_{th}}^{\infty} \frac{\sigma_{\rightrightarrows}(k) - \sigma_{\rightleftarrows}(k)}{k} \mathrm{d}k = 4\pi\alpha s \left(\frac{\kappa\hbar c}{Mc^2}\right)^2, \tag{1.6}$$

where E_{th} is the threshold photon energy for inelastic processes, $\sigma_{\rightrightarrows}$ is the total photo-absorption cross section for circularly polarized light and a polarized target with the spins aligned and $\sigma_{\rightleftarrows}$ for the spins anti-parallel, α is the fine structure constant, κ is the anomalous magnetic moment of the nucleus or nucleon, s is its spin, and M is its mass. The sum rule shows that the energy weighted difference between the spin aligned and anti-aligned cross section is related to the anomalous magnetic moment of the nucleus or nucleon. It was originally derived by [Ger66] and independently by [Dre66]. The derivation is based on the dispersion relation for forward Compton scattering, the optical theorem, and the low energy theorem. The anomalous magnetic moment, κ is related to the total magnetic moment of the particle, M

$$M = (Q + \kappa)\frac{e}{m}s \tag{1.7}$$

where s is the spin of the nucleon or nuclei and Q is the charge. Originally, this sum rule was derived for nucleons only and was later shown to be valid for nuclei as well. A non-zero κ implies that there is an internal dynamic structure for the system being studied. Table 1.1 shows the various κ values and the associated values for the GDH sum rule.

Nucleus	κ	I_{GDH} (μb)
proton	1.973	204.785
neutron	1.913	232.521
deuteron	0.14	0.625
^{3}He	-8.364	496

Table 1.1: The anomalous magnetic moments for different nucleons and nuclei along with the GDH sum rule.

The lower limit of the GDH sum rule integral is E_{th} = 5.494 MeV which is the photodisintegration threshold value. The integral can be broken into two parts, the first from photodisintegration threshold to pion threshold, the energy at which free pions can be created, and the second from pion threshold to infinity. The second part of the integral is expected to have the same strength as the neutron for the ^{3}He S-state (the two protons have opposite spin and cancel). The correction of this value for the ^{3}He D-state changes the value from 232.5 to 230.4 μb. This value neglects two- and three-body photodisintegration, as well as coherent π^0 production, which are expected to be small at these energies, and gives the value of the integral below pion threshold to be 236.5 μb.

The current experiment does not measure the photoproduction cross section of the $^3\vec{\mathrm{H}}\mathrm{e}(\vec{\gamma},\mathrm{d})\mathrm{H}$ reaction directly. However, these polarized photoproduction cross section can be determined by determining the Transition Matrix Elements (TMEs) for the $^2\mathrm{H}(\vec{\mathrm{p}},\gamma)^3\mathrm{He}$ and $^1\mathrm{H}(\vec{\mathrm{d}},\gamma)^3\mathrm{He}$ reactions. The two reactions can be related by the principle of detailed balance (see Section 6.8). The data of the present work therefore allows for the evaluation of the I_{GDH} integral from threshold (5.494 MeV) up to the excitation energy corresponding to E_p(lab) = 80 keV (5.547 MeV). The value obtained will be the first experimentally determined value of the GDH integral for ^{3}He and can be compared to the theoretical estimate of this quantity [Viv96].

1.6 Goals of the Experiment

First and foremost, this experiment aims to accurately determine all of the polarized observables for the $^2\mathrm{H}(\vec{\mathrm{p}},\gamma)^3\mathrm{He}$ and $^1\mathrm{H}(\vec{\mathrm{d}},\gamma)^3\mathrm{He}$ reactions. From this data, the underlying TMEs of the reaction will be determined and compared to the *ab initio*, no parameter, three-body calculations of the Pisa group [Viv96]. The experimentally determined TMEs will also be used to investigate the origin of the "A_y Puzzle" in this reaction, the asymptotic D- to S-state ratio, the M1 doublet to quartet ratio, and the GDH sum rule.

Chapter 2

Theory

Theoretical calculations have finally reached the point where a "first principle" parameter free calculation of the ^{1}H(d, γ)^{3}He and ^{2}H(p, γ)^{3}He reactions can be performed. These calculations take into account explicit meson exchange currents, the Pauli principle, and the associated issues of three-body unitarity. They use a two-body nucleon-nucleon (NN) potential to describe the nuclear force, treat the Coulomb interaction "exactly", and can include various three-body forces. The first calculation was a three-body Faddeev calculation at thermal energies [Fri91], while the newer calculations [Viv96] use a variational technique and work at energies above thermal energy, but below two-body breakup threshold.

2.1 Three Nucleon Physics

The Schrödinger equation can be solved exactly for one and two body systems for both the bound and scattering states. How many nucleons can be included in the cal-

culation and still have an "exact" calculation? The three-body system, despite much recent progress [Fri91, Viv96], still does not have a complete and precise theoretical description. The Coulomb effect in the three-body system is non-trivial and its role in the theoretical models will be discussed later (see Section 2.1.2). The addition of meson exchange currents (MEC) to the theoretical models provide a much more complete description of the reactions. Finally, how valid are the two-body nucleon-nucleon potential models in the three-body system?

2.1.1 Nucleon-Nucleon Potentials

The nucleon-nucleon (NN) potential used for the full calculations, which are compared to the measured data, is the Argonne ν_{18} (AV18) [Wir95]. This is a state-of-the-art potential that fits both np and pp scattering data as well as low energy nn scattering parameters and deuteron properties. Most older potentials, such as Argonne ν_{14} (AV14) [Wir84] and most of the Bonn potentials [Mac87, Mac89], fit only the np or pp scattering data which leads to a poor description of the data set that was not fit. This is due to charge-independence breaking by the strong force [Wir95]. For AV18, The strong interaction potential is projected into a 14 operator charge-independent (CI) part and a charge-independence breaking (CIB) part that contains three charge-dependent and one charge-asymmetric operators. A complete electromagnetic potential containing Coulomb, Darwins-Foldy, vacuum polarization, and magnetic moment terms is also included. The CIB part of the AV18 potential is an improvement over AV14 and allows the potential to fit both the pp and np data sets. The final potential reproduces 4301 np and pp data points over an energy region of 0-350 MeV with a χ^2 per datum of 1.09 [Wir95].

Can this "realistic" two-body potential describe the three-body system as well?

Only within this decade has it become possible to answer this question due to computing power increases that have allowed the three-body Schrödinger equation to be accurately calculated in both the continuum and bound states. The answer to this question is that the two-body NN potentials are not able to model the three-body system by themselves. They underpredict the binding energy of the three-body systems (^{3}He) by 1 MeV [Fri91].

To solve this problem with the binding energy, [Fri91] resorts to a three-body nuclear force (TBF). The canonical example of a TBF is the earth-moon-satellite system. The simplest view of the force on the satellite would be the vector sum of the earth's force and the moon's force. This is not completely accurate because the earth is deformed by the presence of the moon, especially the oceans, which changes the earth's attraction of the satellite. So the system cannot be explained by simple vector sums of the forces, but needs a TBF to include the deformability of the earth. Nucleons have internal structure and "deformability" in the form of Δ-isobars, so a nuclear TBF is reasonable. The TBF added by Friar *et al.* [Fri91] uses two pion exchange and along with the AV14 NN potential gives close to the correct binding energy. This calculations is sensitive to the short-range behavior of the TBF which is not well known [Fri91].

The three-body scattering system needs to be described as well. Theoretical treatment of the elastic scattering experiments yields fairly good results for unpolarized observables [Kie94], but the polarized observables have some difficulties (see Section 1.5.2). The wavefunctions derived from the NN potential models in the elastic-scattering process should also be valid for the continuum wavefunctions in radiative capture. This means that these same NN potentials can be used to calculate the ^{2}H(p, γ)^{3}He and ^{1}H(d, γ)^{3}He reactions. The question is: can the ^{3}He wavefunctions

from these potentials yield accurate descriptions of the ^{2}H($\vec{p},\gamma$)^{3}He and ^{1}H($\vec{d},\gamma$)^{3}He reactions? This will be explored in Chapter 6.

2.1.2 Three-body System Coulomb Effects

The first exact calculation of the Coulomb interaction at thermal energies in the three-body system was carried out in 1991 [Fri91]. The Coulomb interaction, in p-d scattering, polarizes the deuteron and produces a dipole moment, at long range, due to the charge of the incident proton. Because this effect has a long range, the expansion of the potential into partial waves is slow to converge and makes the calculations susceptible to series truncation errors. The three-body system has now been approached using a new method [Viv96] that does not expand the Coulomb terms into partial waves (see Section 2.3).

2.1.3 Meson Exchange Currents

The nuclear force is believed to be mediated by the exchange of mesons. The exchange of charged mesons between nucleons gives rise to what are called Meson Exchange Currents (MECs). MECs are treated phenomenologically in modern two-body NN potentials to transmit the nuclear force: at large distances (r $\geq$ 2 fm) by one pion exchange, in the middle range (1 fm $<$ r $<$ 2 fm) by multiple pion exchange and heavier mesons, and at short range (r $\simeq$ 1 fm) by a hard-core repulsion of the two nucleons due to the Pauli principle. The interaction at medium to short ranges is the least well known and is where the different NN potentials differ. For electric transitions, the current operator can be rewritten in terms of charge density by use of Siegert's theorem (see Section 1.1). The MECs in electric radiation are

therefore not explicit and are masked in the ^{2}H(p,γ)^{3}He reaction by the large one-body current terms. The magnetic terms of the electromagnetic operator have no similar simplification and MEC have to be explicitly inserted. Therefore, reactions that have large magnetic radiation terms are more sensitive to explicit MEC effects. Some three-body radiative capture reactions are particularly sensitive to MECs at low energies. The ^{2}H(p,γ)^{3}He and ^{1}H(d,γ)^{3}He reactions at energies just above threshold are two reactions that have large magnetic dipole (M1) contributions and have large effects due to MEC, as is described below.

In 1950, the large discrepancies between theory and experiment, for the cross section of the ^{1}H(n,γ)^{2}H reaction, motivated an examination of MECs in the reaction [Fri90, Bet50]. This reaction is dominated by magnetic dipole (M1) transitions at thermal energies and the addition of explicit MECs to the M1 terms was found to account for the missing 10% of the cross section [Fri90]. The ^{2}H($\vec{\mathrm{p}}$,γ)^{3}He and ^{1}H($\vec{\mathrm{d}}$,γ)^{3}He reactions at low energies have even larger M1 contributions and are more sensitive to MECs. The reason that these reactions are sensitive to MECs is the fact that the dominant symmetric S-states (ℓ=0) of ^{3}He and ^{3}H are eigenfunctions of the one-body M1 operator. This means that the usually dominant one-body M1 S-state strength vanishes due to the orthogonality of the initial and final states and only M1 strength due to explicit MECs terms and the D-state (ℓ=2) survives. Therefore, the role of the usually small MECs and D-state is greatly enhanced.

Theoretical studies of MECs in three-body systems have usually focused on thermal energies because M1 transitions are typically most important in this region and MEC effects should be most noticeable. The ^{2}H(n,γ)^{3}H reaction is driven mostly by M1 transitions and has a large thermal cross section of 0.508 mb [Jur82] and has therefore been the most thoroughly studied reaction. According to theoretical calcu-

lations by [Tor83] and [Fri90], the inclusion of MECs increases the cross section by a factor of 2.6 and 1.6 respectively. The ^{2}H(p, γ)^{3}He and ^{1}H(d, γ)^{3}He reactions have the Coulomb interaction included since both the target and projectile are charged. The repulsion of the protons lowers the cross section by several orders of magnitude and complicates the calculations with the Coulomb effects. The study of these reactions leads to another check of the effect of MECs and the theoretical treatment of MECs and the Coulomb interaction. Of course, unlike ^{2}H(n, γ)^{3}H, measurements of these reactions cannot be carried out at thermal energies because the ^{1}H(d, γ)^{3}He cross section is so small. Therefore, the experiments presently have to be carried out at tens of keV where the cross section is large enough to allow for accurate measurements on a reasonable time scale. The data can then be extrapolated to thermal energies using the astrophysical S-factor (see Equation 4.5). The other major difference between n-d and p-d capture is that in the limit of E = 0, p-waves vanish for n-d capture but not for p-d capture due to the Coulomb interaction. This is important to our experiment since in the absence of p-wave capture the vector analyzing powers are identically zero.

2.2 Faddeev Calculations

Friar *et al.* published a paper in 1991 [Fri91] that detailed their success in calculating the ^{2}H(p, γ)^{3}He reaction at thermal energies using the Faddeev technique. This reaction had not been studied theoretically before because an exact treatment of the Coulomb interaction was unavailable. The success of [Fri91] motivated the present work in order to check the predictions. Friar *et al.* [Fri91] used the AV14 NN potential to determine the bound and scattering states. Because calculations using only

NN potentials consistently underbind the bound states of ^{3}He and ^{3}H, three-body forces were included in the calculation using the Brazilian (BR) three-nucleon force [Coe83]. The transition rates and S-factor for M1 transitions were calculated using the electromagnetic operator. This work was important because it was the first to rigorously treat the Coulomb effects and the MECs in the $^2\mathrm{H}(\mathrm{p},\gamma)^3\mathrm{He}$. The explicit inclusion of MECs is dominated by three interactions shown in the Feynman diagrams in Figure 2.1 [Tor83, Fri91]. The "Seagull" interaction has a γ-ray, a nucleon and a pion interacting at the same point. The next has a pion and γ-ray interacting at some non-localized point. And finally, a γ-ray excites a nucleon into a Δ-isobar which decays by emitting a pion. There are higher order interactions that include the heavier ρ and ω mesons, but these interactions are much less important because of the higher mass of the mediating mesons and the smaller coupling constants [Tor83].

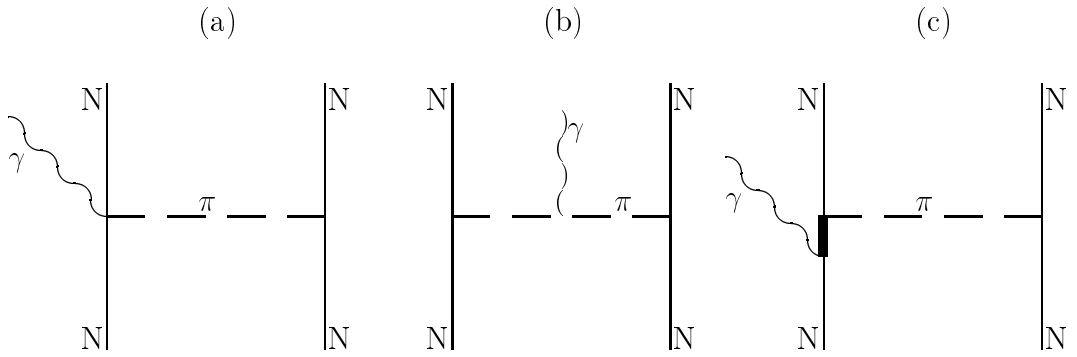

Figure 2.1: The dominant Feynman diagrams used to include MECs in the calculations. The diagram in (a) is called the "Seagull" diagram where a photon, nucleon, and pion interact at a vertex, (b) is for a photon interacting with a pion, and (c) shows a photon exciting a nucleon to a Δ-isobar state that decays by a pion [Fri91, Tor83].

Friar *et al.* [Fri91] used the Faddeev technique to calculate observables for this reaction. The Faddeev technique solves the three-body Schrödinger equation for a given potential. To calculate the $^1\mathrm{H}(\mathrm{d},\gamma)^3\mathrm{He}$ and $^2\mathrm{H}(\mathrm{p},\gamma)^3\mathrm{He}$ reactions the AV14 realistic NN potential was used. This is considered an "exact" technique because the

equations are actually solved to obtain the wavefunctions. The specific solution of nucleon-deuteron scattering is handled in [Che91]. The three-body Faddeev approach derives from the technique used to solve the two-body Schrödinger equation and is used to break the three-body equation into three coupled equations.

The two-body Schrödinger equation is solved most simply by transforming to the center of mass frame [Fri91] and then applying appropriate boundary conditions; one takes $E < 0$ and assumes well behaved wave functions. It is convenient to put the Schrödinger equation into integral form, known as the Lippmann-Schwinger equation

$$|\Psi\rangle = |\phi\rangle + \frac{V}{E - T}|\Psi\rangle \tag{2.1}$$

where $|\Psi\rangle$ is the total wave function, T is the kinetic energy operator, V is the potential, and $|\phi\rangle$ is a plane wave. Thus, Equation 2.1 gives $|\Psi\rangle = |\phi\rangle$ when $V = 0$ which is just the free particle solution. Equation 2.1 can be solved numerically to give a unique solution.

This treatment does not work for the three-body system since there is no unique solution to Equation 2.1 in three-body scattering [Fol57]. This is because the two-body boundary conditions are not specified for the three-body scattering state. The problem is that in three-body scattering there are different channels available due to rearrangement of the channels. Faddeev, in [Fad60], proposed a solution by breaking up the three-body Schrödinger equation as outlined in [Pay86]

$$(E - T - V_1 - V_2 - V_3)|\Psi\rangle = 0 \tag{2.2}$$

where V_i is equivalent to the two-body potential $V(\vec{x}_1)$ where $\vec{x}_1$ is the position vector between particles j and k. The wavefunction is then decomposed into

$$|\Psi\rangle = |\Psi_1\rangle + |\Psi_2\rangle + |\Psi_3\rangle, \tag{2.3}$$

where the Faddeev wavefunctions, $|\Psi_i\rangle$, are defined by

$$(\mathrm{E} - \mathrm{T})\,|\Psi_i\rangle = \mathrm{V}_i\,|\Psi\rangle\,. \tag{2.4}$$

Therefore, each Faddeev wavefunction deals with one of the three possible rearrangement channels.

Substituting the Faddeev wavefunctions, Equation 2.3, into the three-body Schrödinger, Equation 2.2, one gets the equations

$$\begin{aligned}
(\mathrm{E} - \mathrm{T})\,|\Psi_1\rangle &= \mathrm{V}_1\,(|\Psi_2\rangle + |\Psi_3\rangle)\,, \\
(\mathrm{E} - \mathrm{T})\,|\Psi_2\rangle &= \mathrm{V}_2\,(|\Psi_1\rangle + |\Psi_3\rangle)\,, \\
(\mathrm{E} - \mathrm{T})\,|\Psi_3\rangle &= \mathrm{V}_3\,(|\Psi_1\rangle + |\Psi_2\rangle)\,.
\end{aligned} \tag{2.5}$$

These three coupled equations are the Faddeev equations.

To solve the Faddeev equations one must choose a representation from the choices of momentum space, coordinate space or a combination of the two. To expand in momentum space, the Faddeev wavefunctions $|\Psi_i\rangle$ are expanded in terms of momentum "channels" [Pay86]. The potential, V_i, is expanded into channels as well. Unfortunately, the potential for the $^2\mathrm{H}(\mathrm{p},\gamma)^3\mathrm{He}$ and $^1\mathrm{H}(\mathrm{d},\gamma)^3\mathrm{He}$ reactions contains a Coulomb component. As discussed in [Kie94] the expansion of the Coulomb part of the potential is very slow to converge. In fact, to correctly calculate the $^2\mathrm{H}(\mathrm{p},\gamma)^3\mathrm{He}$ reaction in [Fri91], the correct determination of the Coulomb strength required help from variational methods; methods which are employed extensively by the Pisa group [Viv96].

2.3 Variational Calculation

The Pisa group used a slightly different approach to calculate the wavefunctions for the reaction. This approach is described in [Sch95, Viv96] and in this section. The Rayleigh-Ritz variational principle was used to calculate the bound state and the Kohn variational principle was used to determine the scattering state [Del72]. The Argonne ν_{14} (AV14) and AV18 NN potentials [Wir84, Wir95] were used in this calculation. The three nucleon interaction was added to the AV14 potential by use of the Urbana model-VIII three nucleon interaction [Wir91] (AV14/VIII) and for AV18 by use of the Urbana model-IX [Pud95] (AV18/IX). The transition rates and observables were then determined from the electromagnetic operator. Explicit MEC effects were included in the calculation [Sch92, Wir91] and a new method for handling the Δ-isobars was added.

This method solves the Faddeev calculation problem of slow convergence of the partial waves due to the Coulomb terms. This is because the variational method only expands the wavefunctions into channels and not the potentials. Therefore, the Coulomb terms do not slow the convergence in this method.

The variational principle starts out by assuming a parameterized form for the wavefunction, Ψ. A function, $\mathrm{F}[\Psi]$, is defined to be stationary with respect to all of the relevant parameters. The variational principle is therefore defined by [Del72]

$$\frac{\partial \mathrm{F}[\Psi]}{\partial \rho_i} = 0, \tag{2.6}$$

where ρ_i are the parameters being varied.

The second part of the variational principle is identifying an appropriate $\mathrm{F}[\Psi]$. We can use the Rayleigh quotient, $\mathrm{E}[\Psi]$, for the ^{3}He bound state which is defined by

[Bra69]

$$\mathrm{F}[\Psi] = \mathrm{E}[\Psi] = \frac{\langle \Psi | \mathrm{H} | \Psi \rangle}{\langle \Psi | \Psi \rangle}, \tag{2.7}$$

where H is the three-body Hamiltonian. Substituting Equation 2.7 into Equation 2.6, and using the known form of H, we can solve for the parameters ρ_i which gives us the ground state eigenfunctions.

The current calculation does not actually solve these equations directly. Instead, the Rayleigh-Ritz variational method is used to approximate the solution. The basic equation behind this method is [Del72]

$$\mathrm{E}[\Psi] \geq \mathrm{E}_0 \tag{2.8}$$

where E_0 is the ground state eigenvalue. The book [Bra69] shows how to derive this inequality: the first step is to expand the wavefunction in terms of the eigenfunctions of H, ϕ_m

$$|\Psi\rangle = \sum_m \mathrm{a}_m |\phi_m\rangle \,, \tag{2.9}$$

where the eigenfunctions are defined by

$$\mathrm{H}|\phi_m\rangle = \mathrm{E}_m |\phi_m\rangle \,. \tag{2.10}$$

Now substituting Equation 2.9 into Equation 2.7 one gets

$$\mathrm{E}[\Psi] = \frac{\sum_m |\mathrm{a}_m|^2 \, \mathrm{E}_m}{\sum_m |\mathrm{a}_m|^2}. \tag{2.11}$$

Now, if E_0 is subtracted from both sides one gets

$$\mathrm{E}[\Psi] - \mathrm{E}_0 = \frac{\sum_m |\mathrm{a}_m|^2 \, \mathrm{E}_m}{\sum_m |\mathrm{a}_m|^2} - \frac{\sum_m |\mathrm{a}_m|^2 \, \mathrm{E}_0}{\sum_m |\mathrm{a}_m|^2} = \frac{\sum_m |\mathrm{a}_m|^2 \, (\mathrm{E}_m - \mathrm{E}_0)}{\sum_m |\mathrm{a}_m|^2}. \tag{2.12}$$

E_0 is the lowest energy eigenvalue, so the right hand side of Equation 2.12 is always greater than or equal to zero which proves Equation 2.8.

Using the inequality of Equation 2.8, a Monte Carlo search of parameter space to find the values that minimize $E[\Psi]$ is undertaken. When $E[\Psi]$ is minimized, E_0 is found and all the ρ_i are determined which determines Ψ as well.

The calculation of the bound state wavefunction is described for the $^2H(p,\gamma)^3He$ and $^1H(d,\gamma)^3He$ reactions in [Sch96a, Kie93, Kie94]. First, the ground state wavefunction was expanded in Faddeev components like Equation 2.3. The Faddeev wavefunction Ψ_i is then expanded by channel into a product of angular, Y_α, and radial, Φ_α, functions

$$\Psi_i(\vec{x_i},\vec{y_i}) = \sum_a \Phi_\alpha(x_i,y_i)Y_\alpha(jk,i), \tag{2.13}$$

where x_i and y_i are the Jacobi coordinates and (jk,i) is the angular momentum coupling of the three particles (j, k and i). The radial wavefunction is expanded into correlated hyperspherical harmonics [Kie93, Kie94]

$$\Phi_\alpha(x_i,y_i) = \rho^{\ell_\alpha+L_\alpha}F_\alpha(x_i)\left[\sum_K u_K^\alpha(\rho)P_k\right] \tag{2.14}$$

where ρ is the hyperradius, the $F_\alpha(x_i)$ are the correlation functions, the $u_K^\alpha(\rho)$ are the hyperradial functions, and the P_k are the hyperspherical polynomials, all of which are defined in [Kie93]. The correlation functions, $F_\alpha(x_i)$, are obtained by solving the two-body Schrödinger equation as outlined in [Kie93]. They take into account the strong state-dependent correlations due to the NN interaction and improve the behavior of the wavefunction at small interparticle distances. This accelerates the convergence of the wavefunction and reduces the number of basis functions needed [Viv96]. The correlation functions improve the hyperspherical harmonic expansion and make it possible to calculate systems, such as nuclei, that have strong repulsive interactions

at short distances. The quantities that are "solved" for by the Rayleigh-Ritz technique are the hyperradial functions $u_K^\alpha(\rho)$. This technique yields a calculated ^{3}He binding energy that is correct to within 1%.

The Kohn variational method [Del72] was used to calculate the continuum wavefunction. This method is the same as the Rayleigh-Ritz variational method except a different function is used for F[Ψ]. The continuum wavefunction is written as [Kie94]

$$\Psi = \Psi_C + \Psi_A \tag{2.15}$$

where Ψ_C is the "core" wavefunction which is important at small internuclear separations and Ψ_A is the "asymptotic" wavefunction which is important at large internuclear separations. The "core" wavefunction is decomposed into Faddeev components like Equation 2.13. The "asymptotic" wavefunction is decomposed into Faddeev components, $\Omega_{LSJ}(\vec{x}_i, \vec{y}_i)$, which are

$$\Omega_{LSJ}(\vec{x}_i, \vec{y}_i) = \Omega^R_{LSJ}(\vec{x}_i, \vec{y}_i) + \sum_{L'S'} R^{SS'}_{LL'} \Omega^I_{L'S'J}(\vec{x}_i, \vec{y}_i) \tag{2.16}$$

where each Ω_{LSJ} function is expanded as a product of deuteron and two-body Coulomb scattering wavefunctions [Kie94]. The Ω^R_{LSJ} and Ω^I_{LSJ} are functions which use the regular and irregular Coulomb functions respectively. The matrix elements $R^{SS'}_{LL'}$ give the relative weight between regular and irregular components [Kie94]. The subscript L is the relative orbital angular momentum of the deuteron and proton, the subscript S is the channel spin (the vectorial combination of the incident and target particles' spin), and J is the vector sum of L and S.

The total continuum wavefunction, which corresponds to an asymptotic state LSJ, can be written

$$\Psi_{LSJ} = \sum_{i=1,3} \left[\Psi_C(\vec{x}_i, \vec{y}_i) + \Omega^R_{LSJ}(\vec{x}_i, \vec{y}_i) + \sum_{L'S'} R^{SS'}_{LL'} \Omega^I_{L'S'J}(\vec{x}_i, \vec{y}_i) \right] \tag{2.17}$$

where the quantities to be determined are the hyperradial function Ψ_C and the $\mathrm{R}_{LL'}^{SS'}$ matrix elements. The variational method determines these values by finding the stationary value of

$$\mathrm{F}[\Psi] = \mathrm{R}_{LL'}^{SS'} - \left\langle \Psi_{L'S'J} \left| \frac{M}{2\sqrt{3}\hbar^2}(\mathrm{H} - \mathrm{E}) \right| \Psi_{LSJ} \right\rangle \tag{2.18}$$

where H is the Hamiltonian and E is the total energy.

A rigorous comparison of the Faddeev calculations and the variational method has been undertaken recently [Kie98]. They found that the two methods agreed nearly exactly for the nd scattering phase shifts. Currently, the largest restriction on the variational method is that it does not work above the breakup threshold of the deuteron, which corresponds to a $\mathrm{E}_p(\mathrm{lab}) = 3.33$ MeV in the case of $^2\mathrm{H}(\mathrm{p},\gamma)^3\mathrm{He}$ reaction.

Chapter 3

Instruments and Methods

Measurements of the $^2\mathrm{H}(\vec{\mathrm{p}},\gamma)^3\mathrm{He}$ and $^1\mathrm{H}(\vec{\mathrm{d}},\gamma)^3\mathrm{He}$ reactions were carried out at the Triangle University Nuclear Laboratory (TUNL) using the Atomic Beam Polarized Ion Source (ABPIS). The ABPIS produces both vector polarized protons and vector and tensor polarized deuterons at a maximum energy of 80 keV. The beam is focused onto an ice target made of either regular water (H_2O) or deuterated water (D_2O) depending on the reaction. The γ-rays from the resulting reaction are measured as a function of the polarization of the beam using several High Purity Germanium (HPGe) detectors. These measurements determine the polarization observables as a function of angle for the reaction.

3.1 Polarized Beams

Measurements of the polarization observables in the $^2\mathrm{H}(\vec{\mathrm{p}},\gamma)^3\mathrm{He}$ and $^1\mathrm{H}(\vec{\mathrm{d}},\gamma)^3\mathrm{He}$ reactions require both a vector polarized proton and deuteron beam as well as a tensor

polarized deuteron beam. An unpolarized beam means that the ions in the beam have their spins pointing in random directions so that the average number of spins pointing in any direction is equal.

3.1.1 Polarized Protons

A vector polarized beam means that the ions are prepared in such a way that more ions have their spin oriented in one direction. This means that there is an excess population of ions in either the $m_I = 1/2$ or $m_I = -1/2$ angular momentum state for protons. For a given polarization axis, $\hat{\zeta}$, the vector polarization p_ζ is defined as

$$p_\zeta = N_+ - N_- \tag{3.1}$$

where N_+ is the fraction of particles with $m_I = 1/2$ and N_- is the for $m_I = -1/2$ and $N_+ + N_- = 1$. For example, to measure the vector analyzing power $A_y(\theta)$ (see Equation 4.3), $\hat{\zeta}$ is along $\hat{y}$ or $-\hat{y}$ which is shown in Figure 3.1. The cases of $\hat{\zeta}$ along $\hat{x}$ or $\hat{z}$ would give A_x or A_z respectively, but are not of interest since they are required to be zero by parity conservation [Wol49].

The proton beams used for this experiment were polarized along the $\hat{y}$ and are represented by p_y. If $p_y = 0$ then there is no spin excess along the $\hat{y}$ axis. And if the $p_y = \pm 1$ then all proton spins are aligned along the $\pm\,\hat{y}$ axis, respectively.

3.1.2 Polarized Deuterons

Deuterons are more complicated because they are bosons with a spin of 1 which means that a polarized deuteron beam has both vector and tensor moments. The vector and tensor polarization of a spin 1 beam is defined in terms of expectation

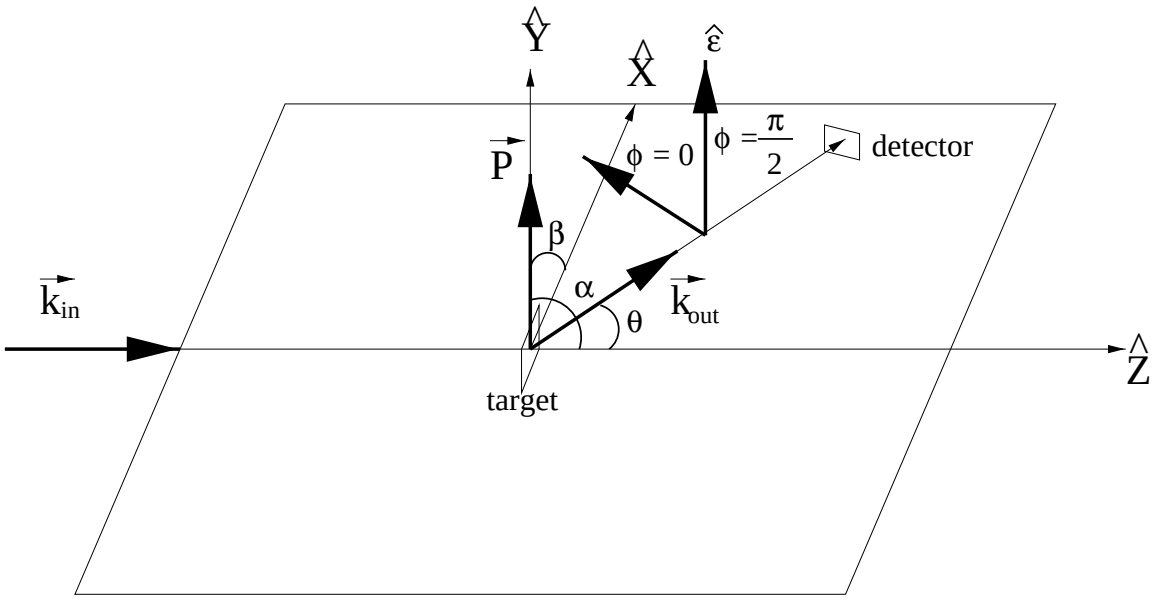

Figure 3.1: This right handed coordinate system for capture reactions uses the Madison Convention [BH71] where $\vec{k}_{in}$ is the incident beam direction and $\vec{k}_{out}$ is the direction of the outgoing γ-ray. The direction $\hat{y} = \vec{k}_{in} \times \vec{k}_{out}$, $\hat{x}$ is along $\vec{k}_{in}$, and the $\hat{x} - \hat{z}$ plane is formed by $\vec{k}_{in}$ and $\vec{k}_{out}$. The angle θ is between the $\hat{z}$ and $\vec{k}_{out}$. The polarization vector $\hat{P}$ is along the $\hat{y}$ axis and is measured by the angles α and β which are both 90° in this case. Finally, the polarization of the outgoing γ-ray is indicated by $\hat{\epsilon}$ which is measured by the angle ϕ.

values of the spin operator **S**

$$p_i = \langle S_i \rangle \tag{3.2}$$

and

$$p_{ij} = \frac{3}{2} \langle S_i S_j + S_j S_i \rangle - 2\delta_{ij}, \tag{3.3}$$

where $i,j = x,y,z$.

The polarized beams produced by the polarized ion source are along the $\hat{z}$ axis. The polarization state of the beam can be represented by the sum of the particles with spin along $+z$, particles with spin along $-z$, and particles with spin distributed in a plane perpendicular to z. These three states correspond to the magnetic substates

$m_I = +1$, $m_I = -1$, and $m_I = 0$, respectively. Using this representation, only the beam moments p_z and p_{zz} are non-zero. As above, let N_+ be the fraction of beam particles with $m_I = +1$, N_- be the fraction with $m_I = -1$, and N_0 be the fraction with $m_I = 0$. Using this

$$p_z = N_+ - N_- \tag{3.4}$$

and

$$p_{zz} = 1 - 3N_0, \tag{3.5}$$

where $N_+ + N_- + N_0 = 1$.

3.1.3 Polarized Ion Source

The Atomic Beam Polarized Ion Source (ABPIS) [Cle90] produces polarized proton and deuteron beams for TUNL. There are four main parts of the ABPIS: the production of the atomic beam, the nuclear spin polarization of the atomic beam, the ionization of the atomic beam, and the extraction and spin precession of the ion beam (see Figure 3.2).

The atomic beam is created by dissociating pure hydrogen or deuterium gas by an RF discharge. The neutral atomic gas is then forced out of the dissassociator through a copper nozzle cooled to 30-35 K and coated in nitrogen to prevent recombination. The cooled atomic beam has less kinetic energy and therefore spends more time in the polarizing regions of the source.

The nuclear spin polarization region of the ABPIS consists of two Stern-Gerlach sextupole magnets and three rf transition units. The magnetic field from the sextupoles focuses atoms with their electron spin projection $m_j = 1/2$ along the beam

Figure 3.2: A diagram of the internal parts of the TUNL ABPIS. A description of the sections can be found in the text. The Spin Filter Polarimeter is not shown in this drawing, but it is located between the Accelerator Tube and the Cesium Oven.

axis while bending the atoms with $m_j = -1/2$ out of the beam so that the beam exiting from the sextupoles is almost pure $m_j = 1/2$. To have a nuclear polarized proton beam one needs to have the nuclear spin states, m_I, selectively populated. This is accomplished by passing the atomic beam through three rf transitions units tuned to selectively populate certain hyperfine splitting states which results in a nuclear spin polarized beam. The technique used is called the adiabatic passage method [Phi87] which uses population inversion between pairs of hyperfine states when the conditions for the static and rf magnetic fields are met.

The hyperfine states of the $1s$ energy level of hydrogen and deuterium can be seen in the Breit-Rabi diagram shown in Figure 3.3. Applying a magnetic field to the atoms causes energy splitting between states of different m_j quantum numbers (Zeeman effect) and splitting of the m_I states within the m_j state (hyperfine splitting). The energy axis of the diagrams is measured in units of zero-field hyperfine splitting ΔW which is 5.875 $\times 10^{-6}$ eV (or multiplying by h it is 1420.4 MHz) for hydrogen and 1.354 $\times 10^{-6}$ eV (327.4 MHz) for deuterium. The magnetic field axis is given in units of the critical field $B_c = \frac{\Delta W}{(g_I - g_J)\mu_B}$ where $g_I = -3.04 \times 10^{-3}$ and $g_J = 2.002$ and μ_B is the Bohr magneton. This gives values of B_c of 50.7 mT for hydrogen and 6.3 mT for deuterium.

For magnetic fields where B is less than B_c, the weak-field region, the good quantum numbers are F and m_F because the magnetic field applied is smaller than the magnetic field at the electron generated by the proton. The total angular momentum for the proton electron system is represented by F and $m_F = m_j + m_I$. The weak-field breaks the degeneracy of the m_F sub-states and a transition in this region inverts the populations of the m_F sub-states, i.e. $m_F \leftrightarrow -m_F$. When the field is greater than B_c, the strong-field region, the good quantum numbers are m_j and m_I.

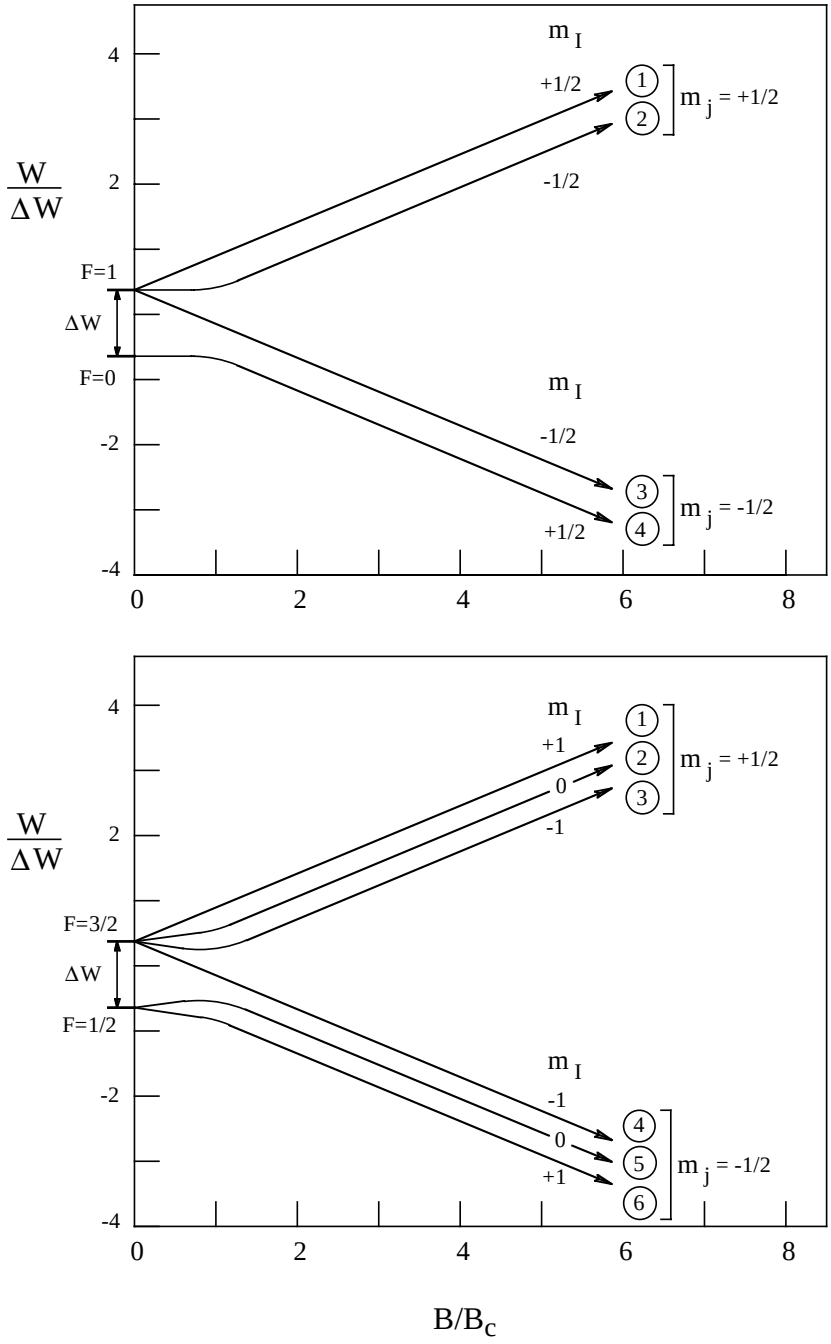

Figure 3.3: This figure shows the energy separation of electron spin substates in hydrogen for increasing magnetic field. The applied magnetic field χ is given in terms of the "critical field", the strength of the magnetic field from the proton at the electron B_c. The energy separation is given in terms of ΔW, the zero field splitting. The four hyperfine levels for protons and the six hyperfine levels for deuterium are numbered in the circles.

An example of how to polarize the atomic beam will be given for hydrogen and deuterium. For hydrogen, a weak-field region and a strong field region are created in two of the rf transition areas. The beam from the sextupoles is nearly pure $m_j = 1/2$. To create a proton polarization of $p_z = -1$, a weak-field and an rf source tuned to the energy between hyperfine states 1 and 3 (see Figure 3.3) leaves the beam in states 2 and 3. For $p_z = +1$, a strong-field and an rf source tuned to the energy split between the 2 and 4 states results in a beam in states 1 and 4. These are in Table 3.1 on lines numbered 1 and 2.

For a deuterium beam with $p_z = \pm 1$ and $p_{zz} = 1$, three transition units and both sextupoles are required. The beam is in states 1, 2, and 3 from the first sextupole and then passes through a region tuned to the transition between states 3 and 4 leaving the beam in states 1, 2, and 4. The beam then passes through a second quadrupole which removes the 4 state. This removes 1/3 of the beam and therefore, the intensity of the beam leaving the source is 2/3 of normal. For a $p_z = +1$ beam the final transition is in the weak-field region between staes 1 and 4 as well as 2 and 3 which leaves the beam in states 3 and 4. While for $p_z = -1$ beam the final transition is in a strong-field region between states 2 and 6 leaving the beam in states 1 and 6. This example is number 9 and 10 in Table 3.1 which also contains all of the states used in this experiment. A description of each observable and the states used to measure it can be found in Chapter 4.

In practice a polarized beam that can quickly switch (10 Hz) between spin states is desirable since this can be used to average over systematic changes in the experiment. This is accomplished by switching the RF sources for the transitions units on and off resulting in a quickly switching beam polarization. The sequence of transition states used is $+ - + + - + --$ which cancels out the first and second order systematic

Num	Nuc	MF1	States	MF2	States	SF	Final	P_z	P_{zz}	I
1	p	off	1,2	off	1,2	$2 \leftrightarrow 4$	1,4	1	–	1
2	p	off	1,2	$1 \leftrightarrow 3$	2,3	off	2,3	-1	–	1
3	d	off	1,2,3	off	1,2,3	off	1,2,3	0	0	1
4	d	off	1,2,3	off	1,2,3	$3 \leftrightarrow 6$	1,2,6	2/3	0	1
5	d	off	1,2,3	$1 \leftrightarrow 4$	2,3,4	off	2,3,4	-2/3	0	1
6	d	off	1,2,3	off	1,2,3	$3 \leftrightarrow 5$	1,2,5	1/3	-1	1
7	d	off	1,2,3	$2 \leftrightarrow 4$	1,3,4	off	1,3,4	-1/3	1	1
8	d	off	1,2,3	off	1,2,3	$2 \leftrightarrow 6$	1,3,6	1/3	1	1
9	d	$3 \leftrightarrow 4$	1,2	off	1,2	$2 \leftrightarrow 6$	1,6	1	1	2/3
10	d	$3 \leftrightarrow 4$	1,2	WF	3,4	off	3,4	-1	1	2/3
11	d	$1 \leftrightarrow 4$	2,3	$1 \leftrightarrow 3$	1,3	off	1,3	0	1	2/3
12	d	$1 \leftrightarrow 4$	2,3	off	2,3	$3 \leftrightarrow 5$	2,5	0	-2	2/3

Table 3.1: The polarization states used in the ABPIS. "Num" is the reference number used in the text to show which transition was used.

asymmetries. During a switch between spin states the polarization of the beam is in an indeterminate state and data taking is stopped for 7 ms (see Section 3.3.1).

The polarized atoms coming out of the transition regions cannot be accelerated because they are neutral. Therefore, the atoms pass through an Electron Cyclotron Resonance (ECR) ionizer that removes the electron from the atoms by collisions with a hot nitrogen plasma. The positive beam is extracted from this region by electrostatic lens whose applied voltage is adjusted for maximum beam transmission. The beam then passes into the Cesium oven which is filled with Cs vapor. The beam can have two electrons added by charge exchange with the Cs vapor resulting in a negatively charged beam. For all of our experiments the positive beam was used because charge exchange is only 10% efficient and high beam currents were necessary. The Cs oven also converts up to 30% of the positive ion beam into atoms which can be in the $2s$ metastable state. The hyperfine population of these atoms can reflect the polarization of the beam under the right conditions. The Spin-Filter Polarimeter (SFP) rf cavity

is located downstream from the Cs oven to measure these metastable atoms. Details of the SFP operation are in Section 3.1.4. Under normal operating conditions the SFP is not used and the cavity is used as an electrostatic lens.

After passing through the SFP, the ions are accelerated to 27 keV and then pass through a Wein-filter spin precessor. The filter has crossed $\vec{E}$ and $\vec{B}$ fields that will only allow ions of a specific velocity to pass along the beam axis undeflected. The polarized beam entering the filter is polarized along the beam direction $\hat{z}$, but the Wein-filter can rotate the beam polarization axis so that it points in any direction. Typically for protons the field and rotation angle were set to leave the beam polarized in the $\hat{y}$ direction for $A_y(\theta)$ measurements. This had the added simplification of no beam precession in the bending magnets because the polarization is parallel (anti-parallel) to the magnetic field. After leaving the Wein-filter, the beam is acclerated to 80 keV and then passes through two electrostatic quadrupoles and into the inflection magnet.

3.1.4 Spin Filter Polarimeter

To create a polarized beam with arbitrary polarization states, the ABPIS has to have the spin transition tuned. The ABPIS has fixed frequencies for spin transitions and then has adjustable magnetic fields to tune to the exact transition. Tuning the source involves changing a magnetic field setting and then measuring its effect on the polarization states. Before the SFP was installed, this was done by sending the beam through the tandem accelerator and measuring the polarization of the beam with a high energy polarimeter. This is a tedious chore and is especially painful for experiments running in the low-energy bay because the beam had to be tuned through the tandem to measure and tune the polarization. These higher energy polarimeters

also need a few minutes of data to yield a reasonable measurement of the polarization. With the installation of the SFP, the beam polarization is measured after tuning the beam onto the experimental target whether it is through the tandem or not. It also allows for immediate feedback for tuning the transition units.

The SFP works by measuring the number of metastable atoms created in the Cs oven that are in a certain hyperfine state. The SFP rf cavity filters out all but one particular nuclear magnetic substate m_I. A specifically tuned rf electric field is established and then an axial magnetic field is varied so that the different m_I substates of hydrogen and deuterium are allowed through the cavity. The atoms that pass through the cavity are then quenched by the removal of the electric field and the resulting photons are detected in a photomultiplier tube. Therefore, the current of the photomultiplier tube as a function of the magnetic field yields peaks at each of the m_I substates for hydrogen and deuterium. The polarization for protons is given by $p_z = \frac{N_+ - N_-}{N_+ + N_-}$ where N_+ is the area of the peak for hydrogen with $m_I = +1/2$ and N_- is for $m_I = -1/2$. For deuterons the same equation holds true for the vector polarization except N_+ is for $m_I = +1$ and N_- is for $m_I = -1$. To measure the tensor polarization of the beam you also need N_0 which is the area of the peak correspnding to $m_I = 0$ and using $p_{zz} = \frac{1-3N_0}{N_+ + N_0 + N_-}$.

Each measurement of the polarization takes about two minutes after all of the different power supplies are set properly, a task that takes about a minute. Unfortunately, when using a positive beam out of ABPIS, the Cs oven has to be heated to get accurate polarization measurements. Heating the Cs oven takes 15-20 minutes and it takes that long to cool down too. Even so, it takes a total of 50-60 minutes to measure the polarization of the beam which is far faster than tuning the beam through the tandem and onto a polarimeter. The SFP software also offers a fixed

magnetic field mode for tuning the transition units. The magnetic field is set to a m_I substate transition and then the transition units are set to maximize that m_I substate. This makes tuning the transition units much easier.

The SFP has been calibrated with respect to the high energy polarimeters at the lab. The SFP typically indicates polarizations 5-10% larger than actually measured by other polarimeters. This discrepency is still not completely understood, but in practice the SFP measurements were used for the polarization of the beam, but 10% was subtracted from the measured values and a 5% error was assigned to the measurement.

3.2 Beam Transport

The 80 keV beam from the ABPIS enters an inflection magnet that was used to deflect the beam by 60° so that it went down our beam line. Directly after the magnet is an electrostatic quadrupole that matches the one on the source before the magnet. The beam is then steered by a steering coil wrapped around the beam line and passes through another quadrupole. A pair of horizontal and vertical slits set to 1" remove any beam that diverges too far from the center of the beam. After the slits is a turbomolecular pump which has a deuteron polarimeter mounted above it. This polarimeter has a deuterated titanium foil for a target and two Silicon detectors mounted at 110° to measure the $^2\mathrm{H}(\mathrm{d},\mathrm{p})^3\mathrm{H}$ reaction (see Section 3.4). The polarimeter was pulled up and out of the beam for most of the experiment, but could be lowered to measure the polarization. After the polarimeter is a cold trap that is kept at 77 K by a liquid nitrogen reservoir. This helped to condense materials in the beam so that they would not accumulate on the target. A final collimator located

approximately 6" before the target defined a beam spot of about 0.5" (see Figure 3.4).

3.2.1 Ice Target

An ice target was used for both the proton and deuteron target. Both a gas jet target and a solid deuterated foil target were considered, but the gas jet was too costly and the deuterated foil target would have been slowly damaged due to beam implantation. Another disadvantage is that they are both rather thin and give relatively low count rates for the 80 keV beam. An ice target, on the other hand, benefits from being easy and cheap to produce and the top layers are slowly vaporized by the beam which reduces problems with implantation. For a proton beam stopping completely in the deuterated ice target you expect the deuterium areal density to be about 10^{18} atoms/cm^2 while for the foil target you expect an order of magnitude decrease and a three orders of magnitude decrease for a gas jet.

The target was produced in a vacuum chamber containing a copper disc thermally coupled to a liquid nitrogen dewar (see Figure 3.5). A nozzle pointed at the copper disc was connected by a valve to a bottle containing either regular or deuterated water. When the valve was opened, the water from the bottle boiled in the vacuum and quickly froze on the copper disc. The target was made about 0.5 mm thick which stopped the beam completely. Only about 1 μm is needed to stop the 80 keV proton beam completely, but the thicker target was necessary to keep the beam from creating holes in the target. When using protons on deuterated ice, a new layer was added to the target every 12 hours to fill in gaps formed by the beam. Targets were made every 4 hours when running deuterons on an regular ice target because the target quickly became deuterated and the $^2\mathrm{H}(\mathrm{d},\mathrm{n})^3\mathrm{He}$ reaction increased the background

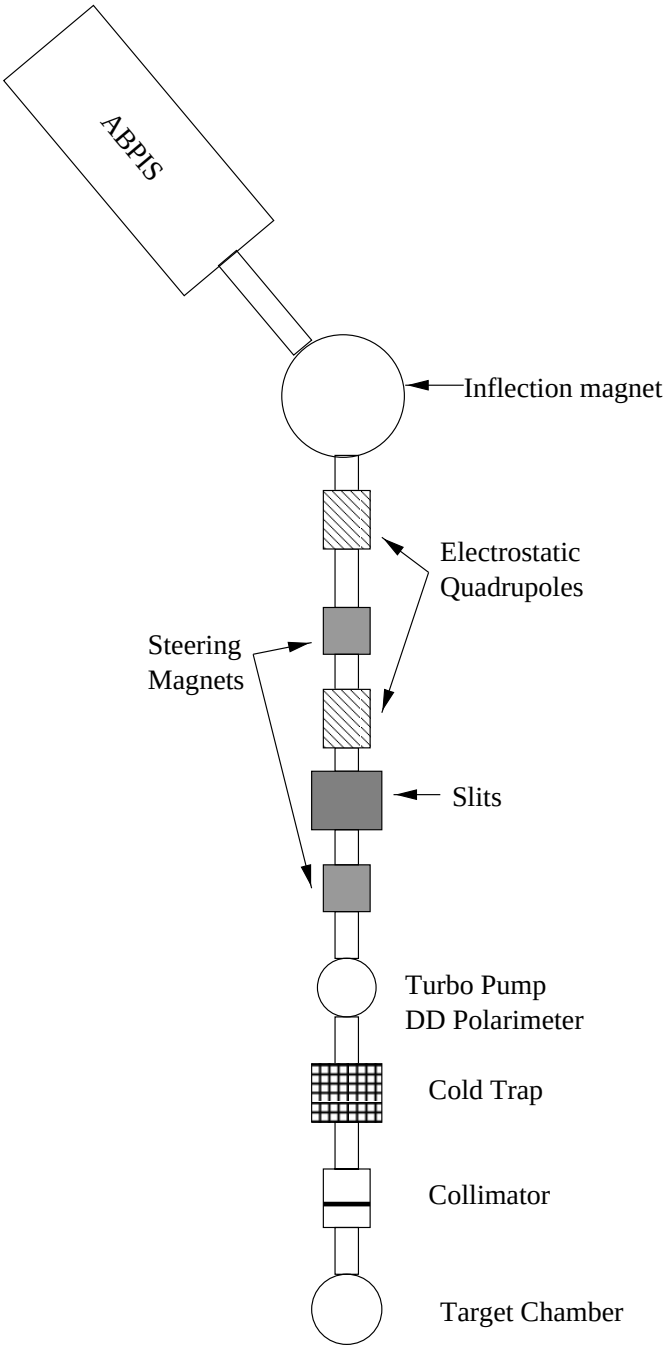

Figure 3.4: The beam line from the ABPIS to the ice target.

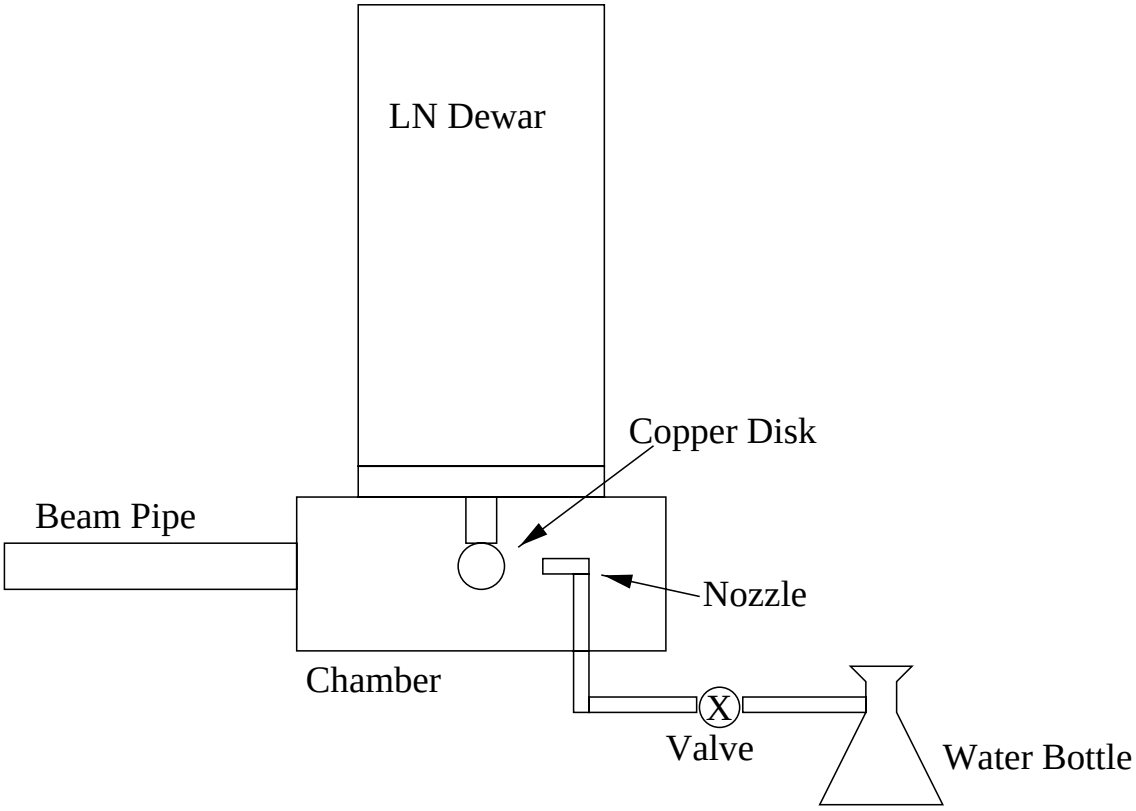

Figure 3.5: The target chamber and other hardware for making an ice target.

(see Section 3.4).

3.2.2 Beam Integration

Accurate determination of the number of protons or deuterons incident on the target is necessary for the measurements of the cross section. This was accomplished by integrating the charge incident on the target with a model 1000 Brookhaven Instruments Beam Current Integrator (BCI) which has an accuracy of 1%. When a current is fed into the BCI, the BCI produces logic pulses which can be counted and the total number of pulses is proportinal to the integrated current.

Secondary electrons leaving the target produce an effective positive current which yields an erroneously high integrated BCI. Therefore, the target is held at +90V to attract any electrons freed from the target. Electrons can also be produced when the beam strikes metal in the beam pipe, i.e. slits and collimator. Electrons from other parts of the beam pipe will be attracted to the positively biased target and will give erroneously low integrated BCI. To reduce these free electrons, the slits and collimator are held at +90V to attract any electrons freed from these surfaces. Batteries with potentials of 90V biased the surfaces by connecting the positive terminal to the surface and the negative terminal to the BCI.

Typically, the measured BCI rises as the bias on the target is increased because fewer electrons are freed from the surface [Sch95]. With the ice targets this effect is not seen due to the high ionization energy and low Z of ice [And77].

3.3 HPGe Detectors

All of the γ-ray measurements were performed using coaxial High Purity Germanium (HPGe) detectors. The HPGe detectors have the advantage of excellent energy resolution at the expense of lower γ-ray detection efficiencies than NaI. For these experiments, both p-type and n-type HPGe detectors were employed. The p-type HPGe is the standard detector which is a Ge crystal doped with Gallium to create extra holes in the crystal. These crystals are called p-type HPGe for the positive charge of the charge carrying holes. This type of HPGe has a high voltage lead running axially down the crystal with the outside of the crystal surrounded by a thin aluminum can that functions as ground. The n-type crystal is doped with Arsenic to produce extra electrons in the crystal and is much harder to manufacture because the outer can is

biased to high voltage and used for current measurement. For both the n-type and p-type crystals a large bias (2400-3500 V) is placed across the crystal to deplete the entire crystal. For the p-type detectors this bias is positive while for the n-type it is negative. A γ-ray incident on the crystal creates electron-hole pairs that are accelerated by the bias and create more electrons and holes as they cascade through the crystal. This cascade produces a current pulse whose charge is proportional to the energy that the γ-ray deposited in the crystal.

The crystal is kept at $\simeq$100 K by putting it in thermal contact with a liquid nitrogen dewar. It is cooled for two reasons; to reduce the number of thermally produced electron-hole pairs and to reduce the noise in the Field Effect Transistor (FET) used as a preamp. The preamp is connected to the high voltage lead of the crystal and converts the crystal's current pulse into a proportionate voltage pulse. Two outputs from the preamp carry the voltage signal to other electronics. In addition, the preamp has a test input for supplying pulses from a pulser to use as an online test of the preamp, amplification, and digitization systems. The final output from of the crystal will shut off the high voltage from a compliant power supply if the crystal warms up.

The HPGe and associated electronics (see Section 3.3.1) yield an energy resolution of 1.5 keV at the 1.33 MeV ^{60}Co line and 4.2 keV resolution at the 5.5 MeV γ-ray from these reactions [Sch95]. The measurement of the γ-rays for this experiment were performed using two p-type HPGe detectors that have efficiencies of 128% and 142% at 1.33 MeV in comparison to a 3" $\times$ 3" NaI crystal with a ^{60}Co source 25 cm from the front face of the crystal. By using multiple detectors we were able to measure several angles at the same time. During some of the experimental runs, an array of four 60% HPGe n-type detectors were used in addition to the two larger detectors

described above. These four smaller crystals, along with the 128% p-type crystal, were used in the Compton Polarimeter which will be discussed in Section 5.3.

A typical HPGe spectrum is shown in Figure 3.6. The highest energy peak, 5.549 MeV, is the photo-peak which is widened by the response of the crystal and because the proton beam was stopped completely in the target which makes the peak 53.3 keV wide. From this spectrum one can observe the three ways that γ-rays interact with a material. At low energies, below 200 keV, the photo-electric effect dominates (see Figure 3.7). In the photo-electric effect, a γ-ray is absorbed by an atom along with the emission of an electron with energy equal to the γ-ray energy minus the binding energy of the electron.

As the photo-electric effect cross section drops, the Compton scattering cross section becomes the dominant process for γ-ray interaction. In Compton scattering, the incident γ-ray, with energy E, scatters at an angle θ off of an electron, with mass m_e, in the crystal and out of the reaction comes a new γ-ray, with energy E$'$ and the electron with a new energy. The equation below relates these quantities.

$$E' = \frac{E}{1 + \frac{E}{m_e c^2}(1 - \cos\theta)} \tag{3.6}$$

The peak at 5.305 MeV is the Compton edge which occurs when the incident γ-ray Compton scatters and the outgoing γ-ray goes back in the same direction as that the incident γ-ray came from, $\theta = 180°$. The Compton scattered γ-rays range in energy from 5.305 MeV down to 0.2443 MeV.

At a γ-ray energy of 1.022 MeV, the γ-ray is energetic enough to produce an electron-positron pair, but this process does not dominate until after 8 MeV. When pair production occurs, the electron and positron are emitted 180° from each other in the center of mass frame. The electron quickly loses its energy to other electrons

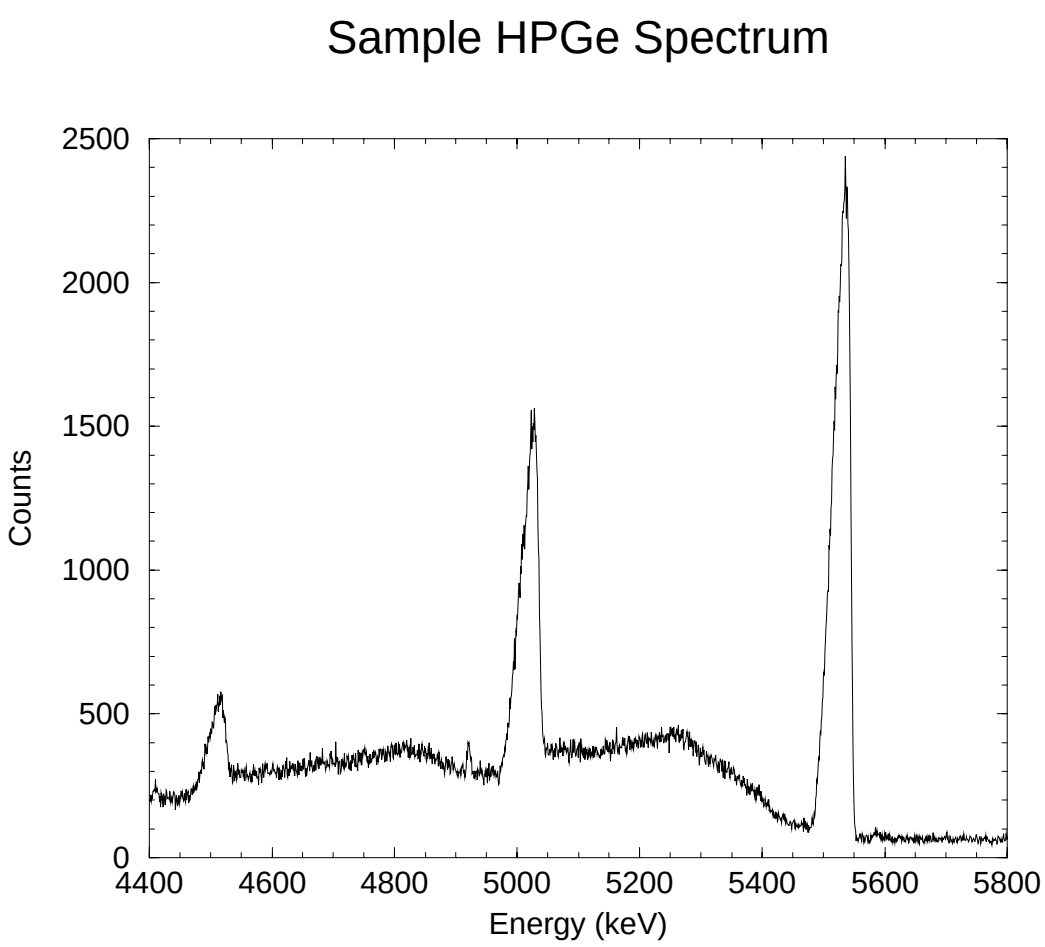

Figure 3.6: Typical spectrum for a HPGe for the ^{2}H(p, γ)^{3}He reaction. The photopeak, Compton edge, and the first and second escape peaks are visible.

in the crystal until it is caught in the crystal. The positron loses its energy to the crystal in much the same way the electron does, but when it has no kinetic or angular momentum left it annihilates with an electron. This produces two 511 keV γ-rays which move in opposite directions in the center of mass frame. The large peak at 5.038 MeV is called the first escape peak which occurs when one of the annihilation γ-rays escapes from the crystal before being detected. The smaller peak at 4.527 MeV is the second escape peak which occurs when both γ-rays escape.

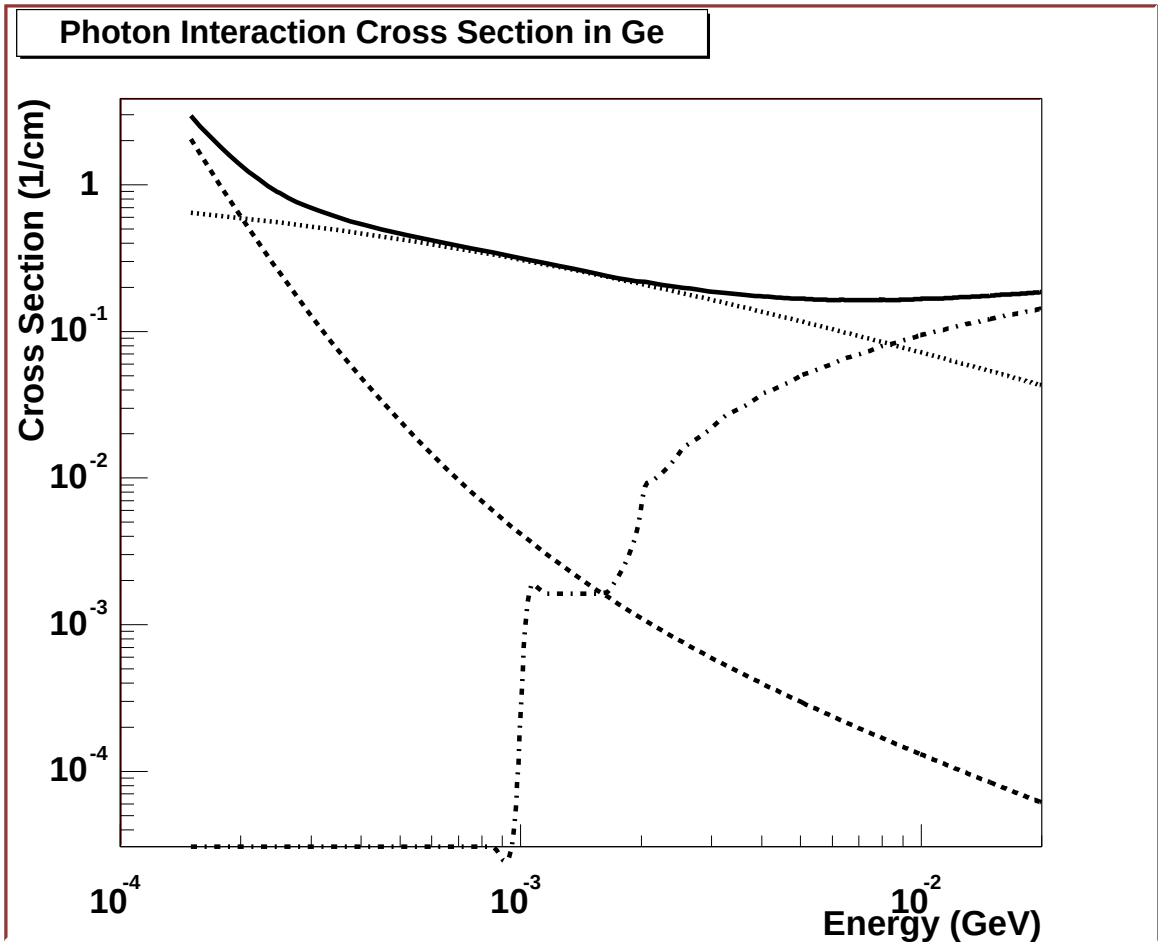

Figure 3.7: This figure shows the photo-absorption cross section for Germanium. The solid line is the total cross section, the dashed line is the photo-electric effect, the dotted line is the Compton cross section, and the dashed dotted line is from pair production.

The main disadvantage of the HPGe detectors is that they are much less efficient at detecting γ-rays in comparison to a comparably sized NaI detector. This is mainly due to the fact that Ge is a lower Z material than NaI. At low energies this is not too much of a problem, but at energies over about 2.5 MeV the difference increases to two orders of magnitude.

3.3.1 Electronics

The electronics for the HPGe detectors are relatively straightforward (see Figure 3.8). The two preamp outputs from the detector are fed into a spectroscopy amplifier and a timing filter amplifier. The voltage signal from the preamplifier output is proportional to the amount of energy deposited in the crystal, but it has to be amplified and shaped in order for an Analog to Digital Converter (ADC) to digitize the signal. The spectroscopy amplifier amplifies the signal and produces a Gaussian shaped signal for input to the ADC. The spectroscopy amplifier is set to a 6 μsec shaping time and the amplification is set to put $\simeq$6.5 MeV as the upper energy from the amplifier which corresponds to a 10 V output pulse. The unipolar output of the spectroscopy amplifier was then sent directly to an Ortec ADC for digitization.

The other output from the preamp is fed into a Timing Filter Amplifier (TFA) that integrates and differentiates the first 200ns of the signal. From this an estimate of the total height of the input pulse is formed and a proportional output pulse is produced. The output of the TFA is connected to the input of a Constant Fraction Discriminator (CFD). The CFD takes the input signal and delays a copy of it by 100ns. The undelayed and delayed signals are summed and a logic pulse is produced after the summed signal crosses zero and rises above a discrimination threshold. The discriminator level and the TFA amplification were set so that the lower energy cut off was 200 keV. The logic signal from the CFD is sent into a Fan Out that is vetoed by the spin flip veto for 7 ms. This signal is from the spin state controller and is used to disable data taking while the spin of the beam is changing from one state to the other. The output of the vetoed fan is sent to a scaler and is also stretched using a gate and delay generator and used as a gate for the ADC and the input register. The scaler keeps track of the number of events seen by the electronics and

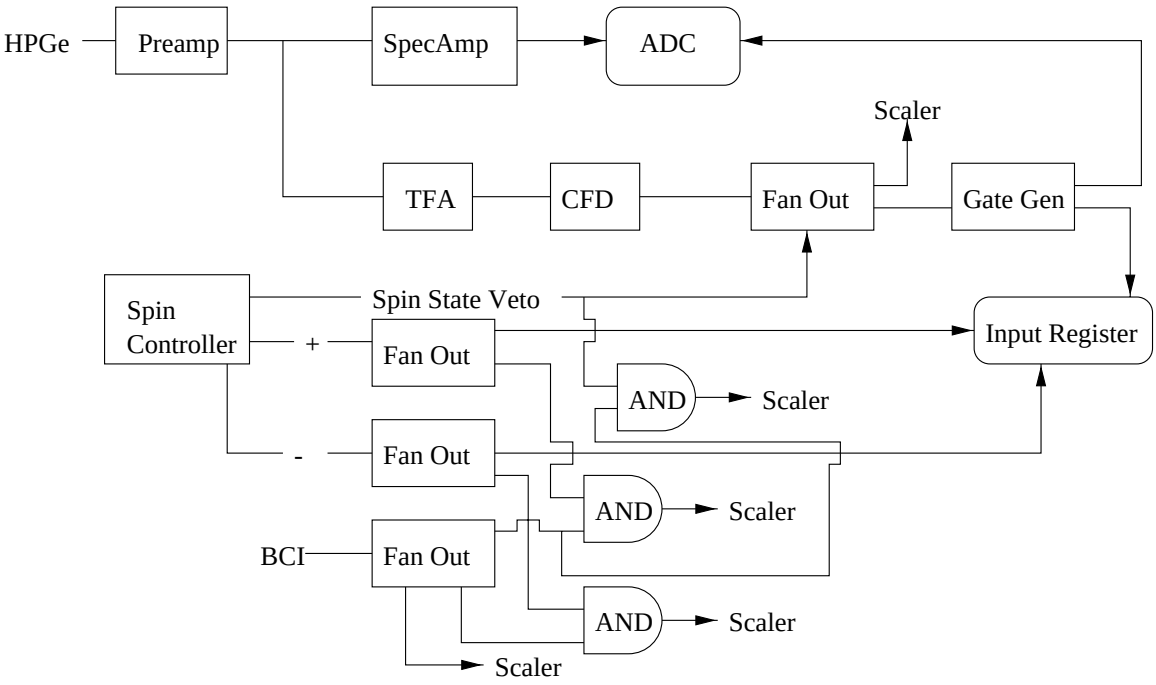

Figure 3.8: Typical electronics for use with a HPGe. A description of the electronics is found in the text.

can be compared to the number of digitized events in the computer which yields the computer dead time. The input register is used to record which spin state the beam was in at the time of the event. The + spin state and − spin state signals from the spin state controller are fed into the input register and every time there is a signal from the gate generator the state of the inputs is recorded.

To keep track of the total beam current on target the logic pulses from the BCI are fed into different scalers. The pulses are fed into a fan out and is then fed through three different ANDs with the three different state signals from the spin state controller. This yields the BCI in each of the different spin states and is used to correct the yield in each spin state for calculating the spin observables.

3.3.2 Computer Interface

The Ortec ADC is located in a CAMAC crate along with other ADCs, scalers, and other electronics. The CAMAC crate is controlled by a Microprogrammed Branch Driver (MBD) that is programmed by a MicroVAX 3200 computer. The software that controls the data acquisition and analysis is called TUNL XSYS. Essentially, the MBD looks for interrupts on 8 different channels. Whenever a channel gets an interrupt a code for that channel is run that performs whatever read out and set up is necessary for the CAMAC event that caused the interrupt. The MBD is connected to the VAX and dumps the data that it acquires into a buffer. The VAX has an analysis program that sorts the events in the buffer, saves them to disk, and displays them in histograms. The XSYS package allows the data to be displayed and analyzed as the data is coming. It also saves the histograms to disk files for offline analysis.

3.4 d+d Reaction

The d+d reactions are both a help and a hindrance for this experiment. To measure the polarization of the deuteron beam, the ^{2}H(d, p)^{3}H reaction was used. The ^{2}H(d, p)^{3}H reaction at 80 keV has well known vector and tensor analyzing powers as a function of angle. Previous measurements [Kra92] of ^{2}H(d, p)^{3}H at 80-0 keV give $A_y(110^\circ) = 0.193 \pm 0.022$ and $A_{yy}(110^\circ) = 0.296 \pm 0.022$. These analyzing powers can be easily measured using two silicon detectors located symmetrically around the beam axis at 110°. The equations can be turned around and the measured asymmetry can give you the vector and tensor polarization of the deuteron beam. The integrated cross section for this reaction is 9.237 mb and 0.6354 mb/sr at 70 keV [Bro90] and the beam polarization can be measured in 5 minutes. Unfortunately, there is no similar

reaction for protons at low energies and so their polarization has to be measured with the SFP or at high energies through the tandem accelerator.

The regular ice target used for $^{1}\mathrm{H}(\mathrm{d},\gamma)^{3}\mathrm{He}$ becomes deuterated as deuterons from the beam become implanted in the ice. The $^{2}\mathrm{H}(\mathrm{d},\mathrm{n})^{3}\mathrm{He}$ reaction has a cross section of 11.38 mb at $\mathrm{E}_{d} = 80$ keV [Bro90] and even with small numbers of deuterons in the target the number of neutrons produced can be substantial. The neutrons interact with the HPGe detector and produce background events (see Figure 3.9). Compare Figure 3.9 to Figure 3.6 and notice the much larger background for the $^{1}\mathrm{H}(\mathrm{d},\gamma)^{3}\mathrm{He}$ reaction. With 30 μA of beam on the water target, a new layer of ice was deposited on the target every 4 hours because the background became so large. This was monitored by comparing the number of events seen in equal width gates at 6 MeV and at 5.547 MeV. When the ratio of counts around the area of interest over the background area became close to the same, a new target was made.

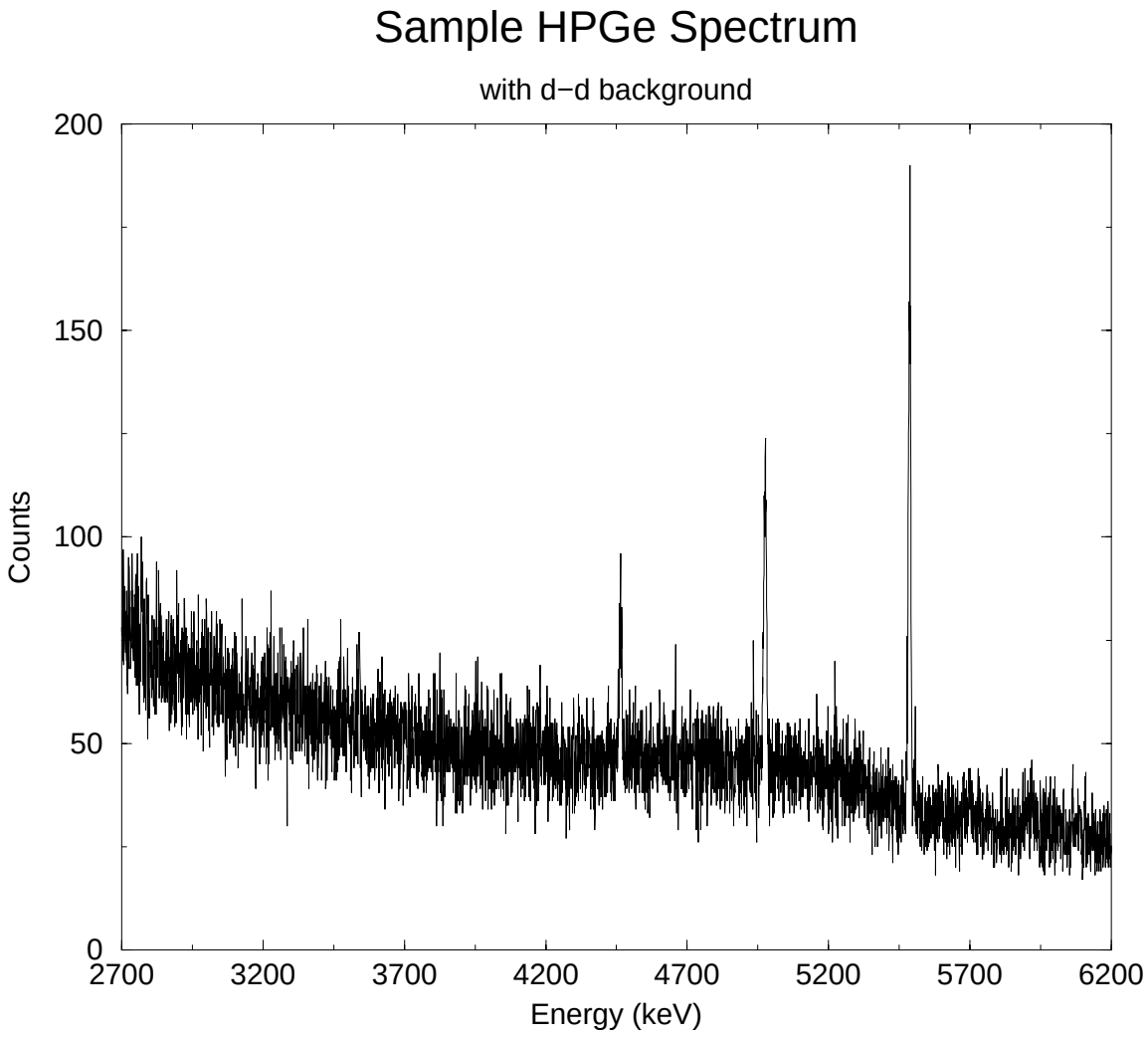

Figure 3.9: Typical spectrum for a HPGe for the $^{1}\mathrm{H}(\mathrm{d},\gamma)^{3}\mathrm{He}$ reaction. The large amounts of background are caused by the neutrons produced in the $^{2}\mathrm{H}(\mathrm{d},\mathrm{n})^{3}\mathrm{He}$ reaction.

Chapter 4

Analysis of Observables

The HPGe spectra acquired from measurements of ^{2}H($\vec{\mathrm{p}}, \gamma$)^{3}He and ^{1}H($\vec{\mathrm{d}}, \gamma$)^{3}He were done at $\mathrm{E}_p = \mathrm{E}_d = 80$ keV and these beams were stopped completely in the ice targets. The observables for the experiment were extracted from the yields determined from these spectra.

This chapter describes most of the different observables that were measured during this experiment: the differential cross section $\sigma(\theta)$, the vector analyzing power $\mathrm{A}_y(\theta)$ and the related factor $i\mathrm{T}_{11}(\theta)$, the tensor moments $\mathrm{T}_{20}(\theta)$, $\mathrm{T}_{21}(\theta)$ and $\mathrm{T}_{22}(\theta)$, as well as the γ-ray polarization $\mathrm{P}_\gamma(\theta)$, and the γ-ray polarization analyzing power $\mathrm{A}_\gamma(\theta)$. All of the observables will be discussed in this section except for the γ-ray observables which are in Chapter 5.

4.1 Differential Cross Section

The differential cross section and absolute cross section measurement were measured for both the ^{2}H(p,γ)^{3}He and ^{1}H(d,γ)^{3}He reactions [Sch95, Sch97]. The thick target data for the proton was deconvoluted (see Section 4.3) to give the cross section for $E_p = 40 - 0$ keV which corresponds to $E_d = 80 - 0$ keV because the proton weighs half as much as the deuteron. The cross section data is given for deuteron data (^{1}H(d,γ)^{3}He) at forward angles. The data from the ^{2}H(p,γ)^{3}He reaction gives the backward angles because one can rotate the ^{2}H(p,γ)^{3}He reaction by 180° in the center of mass system to get the ^{1}H(d,γ)^{3}He reaction. Here it should be pointed out that the center of mass and lab frame angles differ by less than 0.3°. There are some overlapping points between the two measurements which are a good check of the deconvolution analysis as discussed in Section 4.3. The measurements of the cross section were done by Greg Schmid *et al.* and are discussed in his thesis [Sch95] and later publications [Sch97]. The data are presented here in Figure 4.1 and Table 4.1 for completeness because they are used in the TME analysis described in Chapter 6.

4.2 Vector Analyzing Power

The vector analyzing power, $A_y(\theta)$, is measured with a vector polarized beam using the ^{2}H($\vec{p}$,γ)^{3}He reaction. The vector analyzing power $\vec{A}(\theta)$ relates the polarized beam cross section, σ_p, to the unpolarized cross section, σ_0, by the vector polarization of the beam p_ζ (see Equation 3.1) [Sey79]

$$\sigma_p(\theta) = \sigma_0(\theta)\left[1 + \vec{p_\zeta} \cdot \vec{A}(\theta)\right] \tag{4.1}$$

$\theta_{c.m.}$	$\frac{d\sigma}{d\Omega}(\theta)$(nb)	$\Delta\sigma(\theta)$
0.0	1.2590	0.0848
30.14	1.9083	0.0970
45.2	2.5809	0.1290
60.24	3.0411	0.1520
75.27	3.8048	0.1902
90.28	4.2584	0.2129
180.0	1.01	0.05
149.9	1.75	0.09
119.8	3.26	0.16
89.3	4.00	0.20
60.2	3.28	0.16
75.2	4.30	0.33

Table 4.1: The measured cross section data from the ^{1}H(d, γ)^{3}He reaction at E_d = 80-0 keV for the first 6 angles. The next 6 angles are from the ^{2}H(p, γ)^{3}He reaction at E_p = 40-0 keV. The error on the measurement is statistical in nature.

The proton beam is aligned along the $\hat{y}$ direction which leaves us with

$$\sigma_p(\theta) = \sigma_0(\theta)\left[1 + p_y A_y(\theta)\right]. \tag{4.2}$$

The polarization states used from the ABPIS were numbered 1 and 2 as described in Table 3.1. These states yield vector polarized protons along the $+\hat{z}$ and $-\hat{z}$ direction in the ABPIS. The Wein filter is then set to align the spin axis along the $\hat{y}$ axis. Fast spin flipping was used to change the polarization of the beam from along $+\hat{y}$ with polarization p_y^+ to along the $-\hat{y}$ with polarization p_y^-. Typical values for the polarization were around 0.7. Letting p_y^+ and p_y^- be positive values between 0 and 1 and combining this with Equation 4.2 gives

$$A_y(\theta) = \frac{Y_+(\theta) - Y_-(\theta)}{Y_+(\theta)p_y^- + Y_-(\theta)p_y^+} \tag{4.3}$$

where Y_+ is the number of events from the ^{2}H($\vec{p}$, γ)^{3}He reaction with the beam along $+\hat{y}$ and Y_- for beam along -$\hat{y}$. Because the analyzing power involves the ratio of

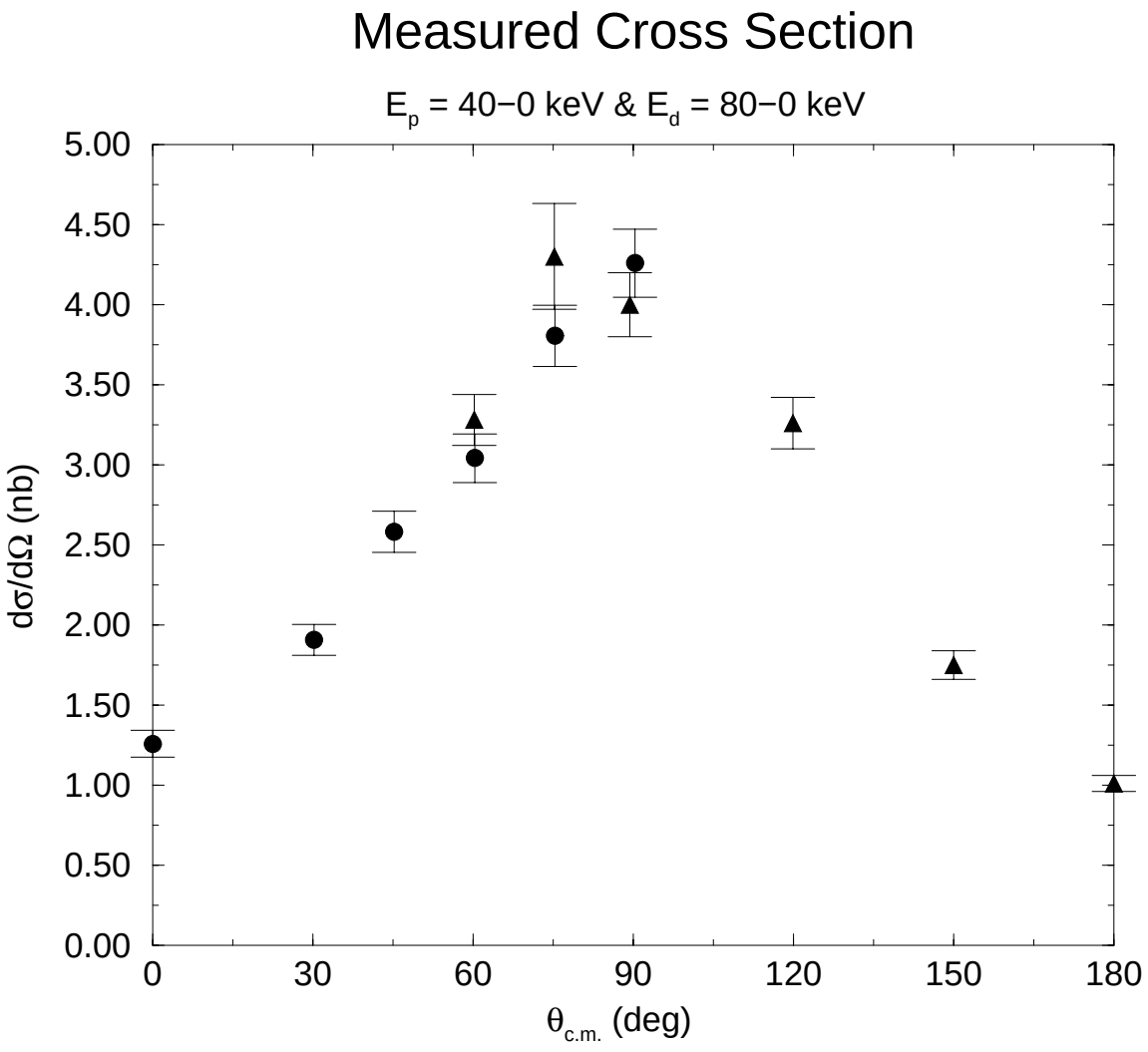

Figure 4.1: The measured cross section for both the ^{1}H(d, γ)^{3}He and ^{2}H(p, γ)^{3}He reactions at E_p = 40-0 keV. The data with circles are taken at E_d = 80-0 keV for the ^{1}H(d, γ)^{3}He reaction. The data with triangles are at E_p = 80-0 keV for the ^{2}H(p, γ)^{3}He reaction deconvoluted to compare with the deuteron data. The error bars are statistical in nature.

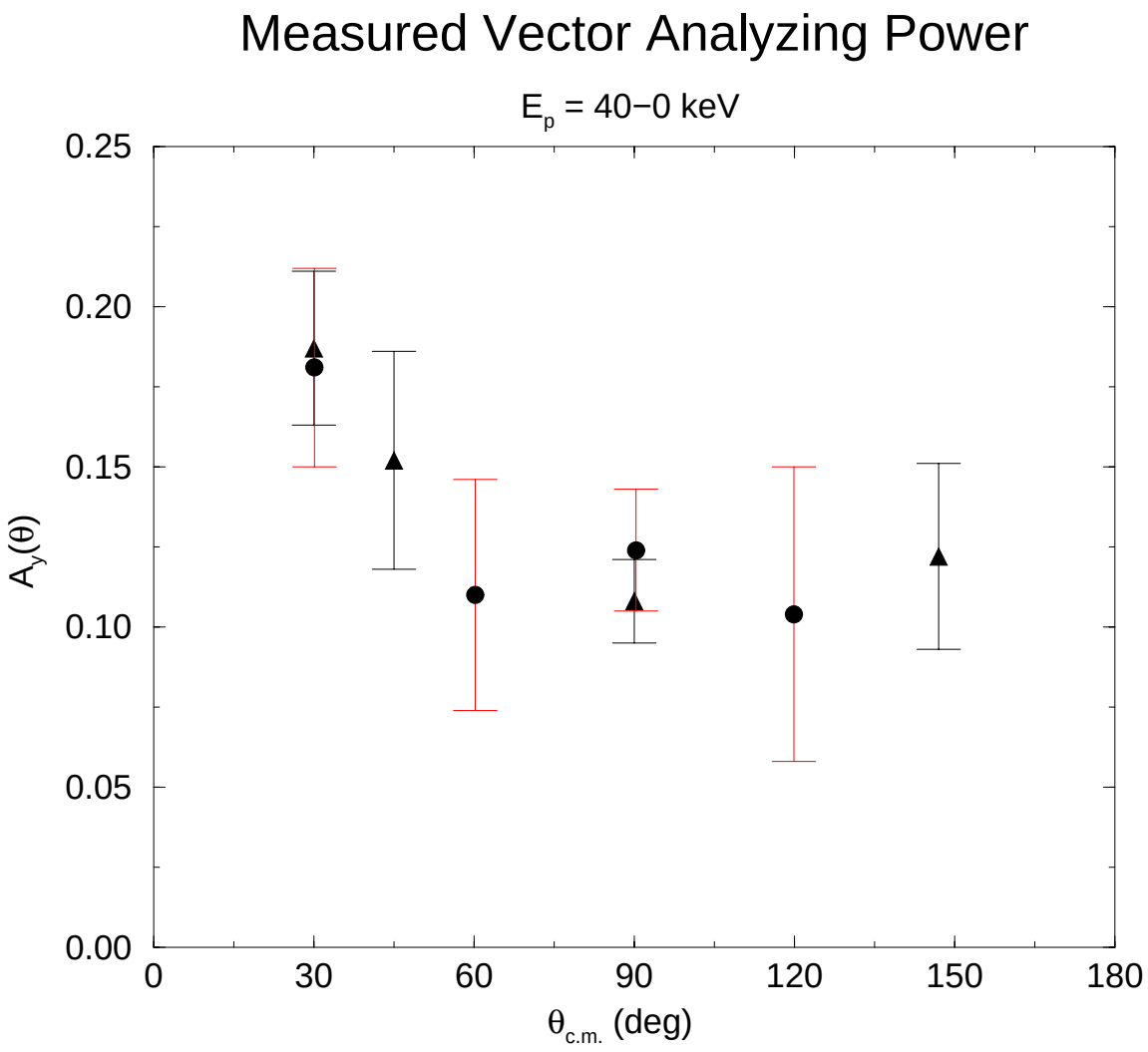

Figure 4.2: The measured vector analyzing power $A_y(\theta)$ for the $^2H(\vec{p},\gamma)^3He$ reaction. The points with circles are measured in [Sch97] and were deconvoluted from E_p = 80-0 keV. The points with triangles were measured for this experiment at E_p = 40-0 keV. The error bars are statistical in nature and also contain the error in the beam polarization measurements.

the yields, there is no dependence on the stopping powers and the other systematic effects are averaged over the two spin states by the fast spin flipping. The same is true for all of the other analyzing powers described in this chapter.

The first four data points at 30°, 60.2°, 90.3°, and 119.8° were measured by Greg Schmid *et al.* and are described in his thesis [Sch95] and his paper [Sch97]. The next four data points were directly measured at E_p = 40-0 keV. The data is presented in Table 4.2 and Figure 4.2.

$\theta_{c.m.}$	$A_y(\theta)$	$\Delta A_y(\theta)$
30.1	0.181	0.031
60.2	0.110	0.036
90.3	0.124	0.019
119.8	0.104	0.046
30	0.187	0.024
45	0.152	0.034
90	0.108	0.013
147	0.122	0.029

Table 4.2: The measured vector analyzing power data for $^2H(\vec{p},\gamma)^3He$ reaction at E_p = 40-0 keV. The first four data points are from deconvolution of data gathered at E_p = 80-0 keV and the last two points are from direct measurement at E_p = 40-0 keV. The error is statistical in nature and also contain the error in the beam polarization measurements.

4.3 Thick Target Analysis

The proton data was collected at E_p = 80-0 keV, but in order to be compared to the deuteron data the proton data from E_p = 40-0 keV had to be extracted. This was accomplished by deconvoluting the spectra from the $^2H(\vec{p},\gamma)^3He$ and $^2H(p,\gamma)^3He$ reactions to get the cross section and vector analyzing power values.

4.3.1 Deconvolution Analysis

The spectra are deconvoluted to remove the HPGe detector response function and the changing deuterium areal density so that the remaining spectra show only the energy dependence of the $^2\mathrm{H}(\vec{\mathrm{p}},\gamma)^3\mathrm{He}$ and $^2\mathrm{H}(\mathrm{p},\gamma)^3\mathrm{He}$ reactions. To remove these two effects, a functional form of the HPGe response function and of the $^2\mathrm{H}(\vec{\mathrm{p}},\gamma)^3\mathrm{He}$ yield are found. Then the two functions are convoluted together and fit to the spectra.

The yield (Y) from the $^2\mathrm{H}(\vec{\mathrm{p}},\gamma)^3\mathrm{He}$ reaction can be written in terms of the deuterium areal density (D), the number of protons incident on the target (P), the efficiency and solid angle of the detector ($\epsilon \mathrm{d}\Omega$), and the cross section $\sigma(\theta_{lab}, \mathrm{E}_{lab})$

$$\mathrm{Y}(\theta_{lab}, \mathrm{E}_{lab}) = \mathrm{D}(\mathrm{E}_{lab})\ \mathrm{P}\ \epsilon \mathrm{d}\Omega\ \sigma(\theta_{lab}, \mathrm{E}_{lab}). \tag{4.4}$$

The cross section can be written in terms of the astrophysical S-factor

$$\sigma(\theta_{lab}, \mathrm{E}_{lab}) = \frac{\mathrm{S}(\theta_{lab}, \mathrm{E}_{lab}) e^{-2\pi\eta}}{\mathrm{E}_{c.m.}} \tag{4.5}$$

where η is the Sommerfield parameter which is related to the center of mass energy in keV

$$2\pi\eta = 31.29\ \mathrm{Z}_1\ \mathrm{Z}_2\ \left(\frac{\mu}{\mathrm{E}_{c.m.}}\right)^{1/2} = \frac{25.639}{\sqrt{\mathrm{E}_{c.m.}}}. \tag{4.6}$$

The S-factor is the result of removing the Coulomb energy dependence from the cross section. The astrophysical S-factor is assumed to be linear with energy far from a resonance and at very low energies where s-wave and p-wave capture dominate so that

$$\mathrm{S}(\theta_{lab}, \mathrm{E}_{lab}) = \mathrm{S}_0(\theta) + \mathrm{E}_{c.m.}\mathrm{S}_1(\theta) \tag{4.7}$$

where S_0 and S_1 are two parameters determined by the fit to the spectra. Combining

Equations 4.4, 4.5 and 4.7 yields

$$Y(\theta_{lab}, \mathrm{E}_{lab}) = \frac{\mathrm{S}_0(\theta_{lab}, \mathrm{E}_{lab}) + \mathrm{E}_{c.m.}\mathrm{S}_1(\theta_{lab}, \mathrm{E}_{lab})}{\mathrm{E}_{c.m.}} e^{\frac{-2\pi\eta}{\mathrm{E}_{c.m.}}} \mathrm{D}(\mathrm{E}_{lab})\mathrm{P}\epsilon \mathrm{d}\Omega. \tag{4.8}$$

The calculation of the response function is more complicated and is described thoroughly in [Sch95]. Essentially, the total response function of the HPGe is a convolution of the the intrinsic response of the HPGe to the incident γ-ray with the kinematic response of the crystal due to its finite geometry.

The intrinsic response was calculated by fitting three functions to the response of the HPGe to the γ-rays of a ^{66}Ga source [Sch96b]. The first function is a gaussian that accounts for the statistical nature of the charge collection. The second is also a Gaussian that is thought to arise from incomplete charge collection. The third function is a step function due to photo-electrons escaping from the crystal and Compton scattering background. These functions were fit to the full energy peaks of the different γ-rays in the ^{66}Ga source.

The kinematic response function was determined by a Monte Carlo simulation of the detector which took into account the multiple scattering of the γ-rays in the crystal. The simulation calculated the effect of the detector accepting γ-rays from different angles other than the one of interest because the front face of the detector has a finite size. The γ-rays from other angles have different energies which widen the response of the detector.

The response function and the yield function were convoluted to give a total response function. This function was fit to each spectrum and the two parameters S_0 and S_1 from Equation 4.8 were determined. This information was used to determine the *S*-factor which gave the cross section as a function of energy. This allowed the observables $\sigma(\theta)$ and $\mathrm{A}_y(\theta)$ for E_p = 40-0 keV to be extracted from the full energy

data.

4.3.2 Comparison of Deconvoluted Data

Two tests of the deconvolution analysis were performed. The first was done by measuring the cross section from the ^{2}H(p,γ)^{3}He and ^{1}H(d,γ)^{3}He reaction. A comparison of the measured cross section at E_d = 80-0 keV (corresponding to E_p = 40-0 keV) to the deconvoluted data obtained from the data taken at E_p = 80-0 keV shows good agreement at the three overlapping angles of 60°, 75°, and 90° in the lab frame of the ^{1}H(d,γ)^{3}He reaction (see Table 4.3 and Figure 4.1). The vector analyzing power $A_y(\theta)$ was measured directly at $E_p = 40 - 0$ keV. The measurements at 30° and 90° agreed within error with the deconvoluted analyzing powers measured previously (see Table 4.4 and Figure 4.2).

$\theta_{c.m.}$	$\sigma(\theta)$ for ^{1}H(d,γ)^{3}He	$\sigma(\theta)$ for ^{2}H(p,γ)^{3}He
60.24	1.00615 ± 0.0502895	1.08519 ± 0.0529363
75.27	1.25883 ± 0.062928	1.42266 ± 0.109181
90.28	1.4089 ± 0.0704384	1.32341 ± 0.0661704

Table 4.3: The cross section measured directly from the ^{1}H(d,γ)^{3}He reaction at E_d = 80-0 keV and the deconvoluted cross section measured by deconvolution from the ^{2}H(p,γ)^{3}He reaction at E_p = 40-0 keV.

$\theta_{c.m.}$	Deconvoluted $A_y(\theta)$	$A_y(\theta)$ (E_p = 40-0 keV)
30	0.187 ± 0.024	0.181 ± 0.031
90	0.108 ± 0.013	0.124 ± 0.019

Table 4.4: The measured analyzing power data at E_p = 40-0 keV compared to the deconvoluted data.

4.4 Tensor Analyzing Powers

Above, we dealt with the observables for $^2\mathrm{H}(\vec{\mathrm{p}},\gamma)^3\mathrm{He}$ reaction which involves a spin 1/2 proton as the polarized beam. With a polarized deuteron beam there are tensor moments due to the deuteron's spin of 1. There is an equation similar to Equation 4.2 that relates the unpolarized cross section σ_0 to the polarized cross section σ_p using the tensor moments of the beam.

$$\sigma_p(\theta) = \sigma_0(\theta)\left\{1 + \sqrt{3}\mathrm{p}_z i\mathrm{T}_{11} + \mathrm{t}_{20}\mathrm{T}_{20}(\theta) + 2Re\left[\mathrm{t}_{21}\mathrm{T}_{21}(\theta)\right] + 2Re\left[\mathrm{t}_{22}\mathrm{T}_{22}(\theta)\right]\right\}. \tag{4.9}$$

The other tensor moments do not affect the cross section since it is only sensitive to moments normal to the scattering plane due to parity conservation. Equation 4.9 can also be written in terms of

$$\mathrm{I}_p(\theta) = \mathrm{I}_0(\theta)\left[1 + \sqrt{3}\mathrm{p}_z i\mathrm{T}_{11}\sin\beta\cos\phi + \frac{1}{2\sqrt{2}}\mathrm{p}_{zz}\mathrm{T}_{20}(\theta)\left(3\cos^2\beta - 1\right)\right.$$
$$\left. -\sqrt{3}\mathrm{p}_{zz}\mathrm{T}_{21}(\theta)\sin\beta\cos\beta\sin\phi - \frac{\sqrt{3}}{2}\mathrm{p}_{zz}\mathrm{T}_{22}(\theta)\sin^2\beta\cos 2\phi\right]. \tag{4.10}$$

where $\mathrm{I}_p(\theta)$ is the intensity of the beam, β is the angle between the z-axis and the quantization axis and ϕ is the angle from the y-axis to the projection of the quantization axis onto the x-y plane. A beam polarized along the y-axis would have $\beta = 90^\circ$ and $\phi = 0^\circ$ and 180° for spin up and spin down respectively.

4.4.1 $i\mathbf{T_{11}}$

The observable $i\mathrm{T}_{11}(\theta)$, also called the vector analyzing power, for $^1\mathrm{H}(\vec{\mathrm{d}},\gamma)^3\mathrm{He}$ is similar to $\mathrm{A}_y(\theta)$ for $^2\mathrm{H}(\vec{\mathrm{p}},\gamma)^3\mathrm{He}$ and is measured in much the same way. To measure $i\mathrm{T}_{11}(\theta)$ the tensor polarization of the beam p_{zz} was set equal to 0 so that the

other tensor moments would not appear in the measurements. Therefore, the states numbered 4 and 5, described in Table 3.1, were used. The only problem with these states is that the theoretical maximum value for p_z is only $\frac{2}{3}$. Unfortunately, there is no other way to eliminate the other tensor moments since no choice of β and ϕ can eliminate all three. The beam polarization axis was set along the $\hat{y}$ axis ($\beta = 90°$) with spin flipping between $\phi = 0°$ and $180°$. $iT_{11}(\theta)$ is defined by

$$iT_{11}(\theta) = \frac{1}{\sqrt{3}} \frac{Y_+(\theta) - Y_-(\theta)}{Y_+(\theta)p_y^- + Y_-(\theta)p_y^+}. \tag{4.11}$$

The analyzing power for the $^1H(\vec{d},\gamma)^3He$ reaction can be defined in terms of $iT_{11}(\theta)$

$$A_y(\theta) = \frac{\sqrt{3}}{2} iT_{11}(\theta). \tag{4.12}$$

In this case though p_y measures p_z for the deuteron beam and Y is the yield for $^1H(\vec{d},\gamma)^3He$. The values of $iT_{11}(\theta)$ are published in [Ric97b] and are presented in Table 4.5 and Figure 4.3.

$\theta_{c.m.}$	$iT_{11}(\theta)$	$\Delta iT_{11}(\theta)$
15.0	-0.0130	0.049
32.0	-0.1040	0.02558
54.0	-0.0768	0.0184
90.0	-0.0727	0.01143
126.0	-0.0972	0.01673
134.0	-0.1130	0.021
148.0	-0.0921	0.02885

Table 4.5: The measured $iT_{11}(\theta)$ data at E_d = 80-0 keV. The errors are statistical in nature and also contain the error in the beam polarization measurements.

4.4.2 T_{20}

The observable $T_{20}(\theta)$ is measured in much the same manner as $iT_{11}(\theta)$. Equation 4.10 shows that a tensor polarized beam aligned along the $\hat{z}$ axis ($\beta = 0°$ and ϕ

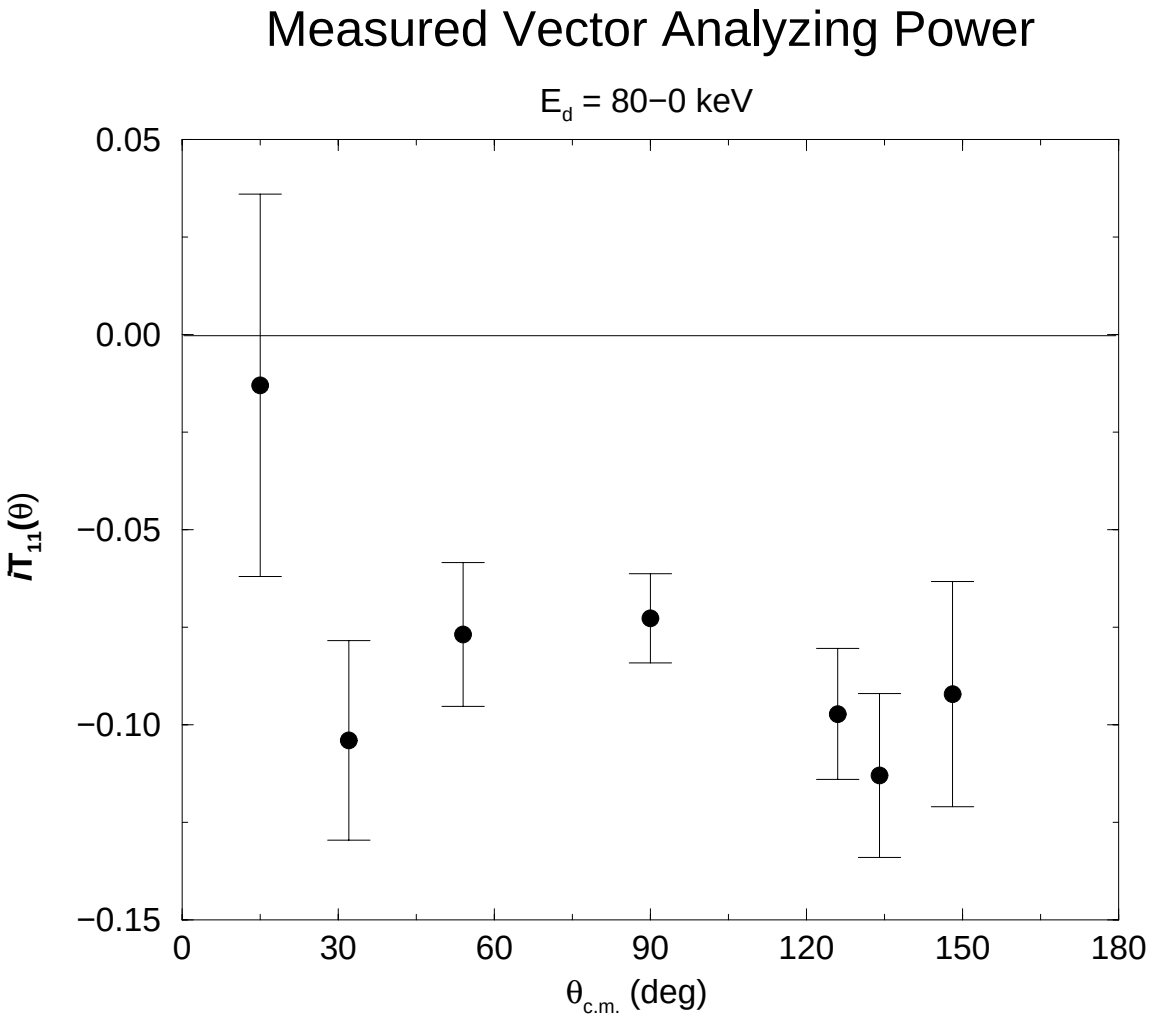

Figure 4.3: The measured vector analyzing power $iT_{11}(\theta)$ for the $^1H(\vec{d},\gamma)^3He$ reaction at E_d = 80-0 keV. The error bars are statistical in nature and also contain the error in the beam polarization measurements.

$\theta_{c.m.}$	$T_{20}(\theta)$	$\Delta T_{20}(\theta)$
0.0	0.318	0.035
20.12	0.170	0.032
90.28	-0.105	0.0092
30.14	0.043	0.038
60.20	-0.120	0.031
120.0	-0.095	0.024
134.9	0.047	0.034
149.9	0.288	0.033
45.20	-0.130	0.032

Table 4.6: The measured $T_{20}(\theta)$ data at E_d = 80-0 keV. The errors are statistical in nature and also contain the error in the beam polarization measurements.

undefined) will only measure intensity changes from $T_{20}(\theta)$. To do this the ABPIS was tuned to states numbered 6 and 7 from Table 3.1 to yield a beam with $p_{zz} = 1$ and -1. The vector polarization of the beam does not matter because the $iT_{11}(\theta)$ contribution is removed by setting $\beta = 0°$. The polarization was spin flipped from $\beta = 0°$ to 180° for the two spin states. The definition of T_{20} is similar to the other observables

$$T_{20}(\theta) = 2\sqrt{2}\frac{Y_+(\theta) - Y_-(\theta)}{Y_+(\theta)p_{zz}^- + Y_-(\theta)p_{zz}^+}. \tag{4.13}$$

This observable was measured by Schmid *et al.* [Sch97] and the values are given in Table 4.6 and Figure 4.4.

4.4.3 T_{21}

The $T_{21}(\theta)$ observable was measured using two different methods. The first method relied on cancelling out the effects of the polarized observables by setting the Wein Filter to $\beta = 54.7°$ and $\phi = 45°$ or 225°. The problem with this method is that the angles have to be set precisely or else the other observables bleed in. In

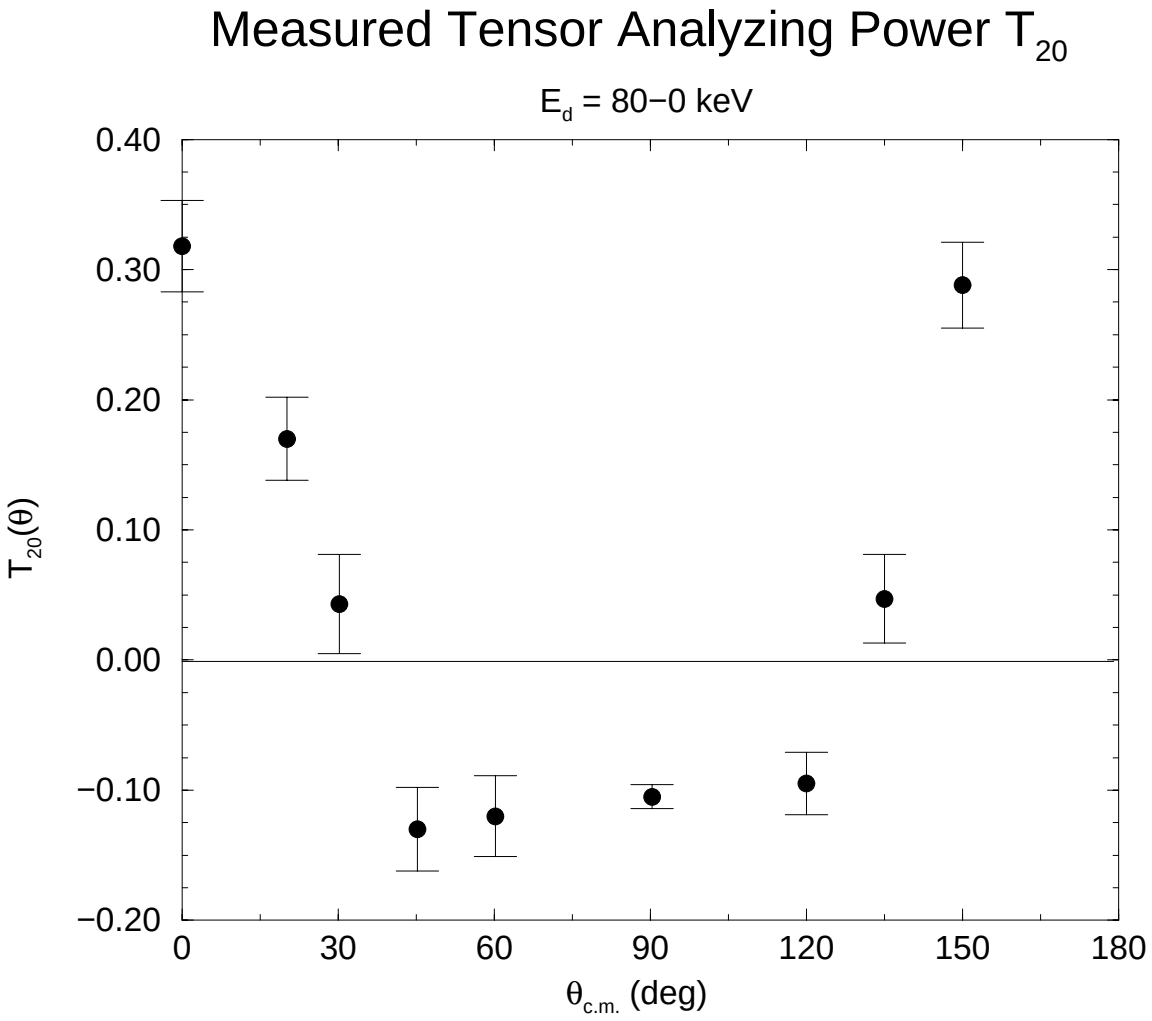

Figure 4.4: The measured $T_{20}(\theta)$ data at $E_d = 80$-0 keV. The error bars are statistical in nature and also contain the error in the beam polarization measurements.

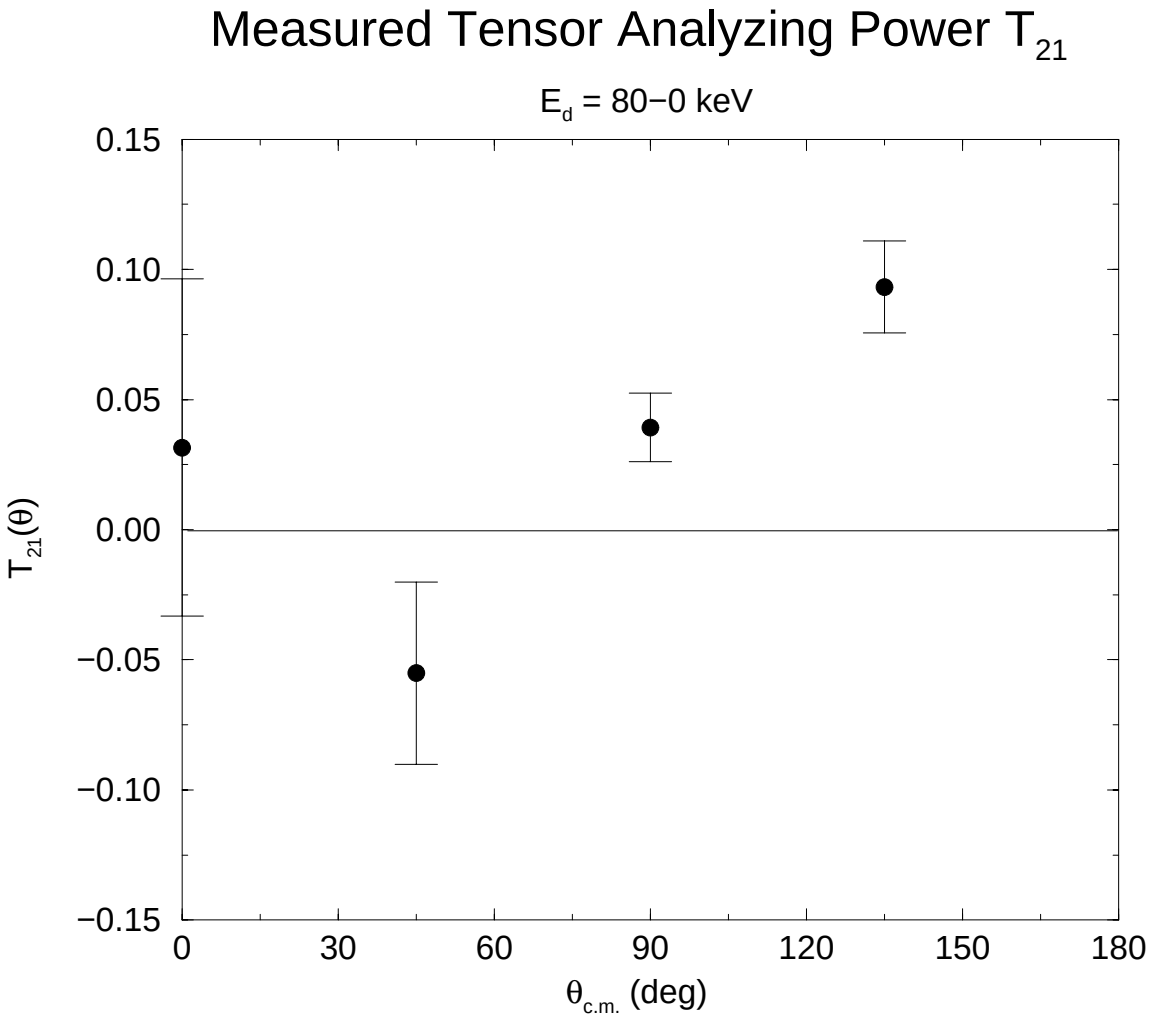

Figure 4.5: The measured $T_{21}(\theta)$ data at E_d = 80-0 keV using the first method. The error bars are statistical in nature and also contain the error in the beam polarization measurements.

this method, the ABPIS was tuned to the states numbered 11 and 12 in Table 3.1. This set $p_z = 0$ so that iT_{11} was eliminated. Setting p_z to be exactly 0 is important because, looking at the numerical factors in front of iT_{11} and T_{21}, one can see that iT_{11} can contaminate T_{21} 27/4 times more strongly than T_{21} can contaminate iT_{11} [Ohl73]. The two spin states had theoretical maxima for p_{zz} of 1 and -2 respectively. Unfortunately, this state only allows $\frac{2}{3}$ of the beam to exit the source because $\frac{1}{3}$ is removed by the second sextupole. The expression used to obtain $T_{21}(\theta)$ using this method is similar to that used to obtain the other observables

$$T_{21}(\theta) = -\frac{1}{\sqrt{3}} \frac{Y_+(\theta) - Y_-(\theta)}{Y_+(\theta)p_{zz}^- + Y_-(\theta)p_{zz}^+}. \tag{4.14}$$

The values measured using this method are given in Table 4.7 and Figure 4.5. The value of $T_{21}(0^\circ)$ is consistent with zero, but not measured to be zero. The value has to be zero at 0° because the expansion of $T_{21}(\theta)$ in terms of Legendre functions (see Appendix A) shows that it must equal zero. The reason it was measured to be non-zero is probably due to misalignment of the spin axis letting other observables bleed into this measurement.

$\theta_{c.m.}$	$T_{21}(\theta)$	$\Delta T_{21}(\theta)$
0	0.0315	0.0648
45	-0.0551	0.0350
90	0.0393	0.0132
135	0.09325	0.0177

Table 4.7: The measured $T_{21}(\theta)$ data at E_d = 80-0 keV using the first method. The errors are statistical in nature and also contain the error in the beam polarization measurements.

The other method used to measure $T_{21}(\theta)$ involved three spin states and is described in detail in Ohlsen *et al.* [Ohl73]. The added bonus of using this method is that the values of $A_{yy}(\theta)$ can be measured at the same time. Unfortunately, $A_{yy}(\theta)$,

unlike $T_{21}(\theta)$, is then very sensitive to misalignments of the spin axis. The three spin states used in this method have $p_{zz} = 0, \pm 1$. From Table 3.1 the states numbered 6 and 7 were chosen for $p_{zz} = \pm 1$ and all transition units off for the unpolarized case $p_{zz} = 0$. β was set to 45° and ϕ was spin flipped between $\pm 90°$. Taking these values and substituting into Equation 4.9 you get

$$L(\theta) = \frac{I(\theta, -90°)}{I_0(\theta)} = 1 + \frac{\sqrt{3}}{2} p_{zz} T_{21}(\theta) + \frac{1}{4\sqrt{2}} p_{zz} T_{20}(\theta) + \frac{\sqrt{3}}{4} p_{zz} T_{22}(\theta) \qquad (4.15)$$

$$R(\theta) = \frac{I(\theta, 90°)}{I_0(\theta)} = 1 - \frac{\sqrt{3}}{2} p_{zz} T_{21}(\theta) + \frac{1}{4\sqrt{2}} p_{zz} T_{20}(\theta) + \frac{\sqrt{3}}{4} p_{zz} T_{22}(\theta) \qquad (4.16)$$

where I_0 is the intensity of the reaction for an unpolarized beam, $p_{zz} = 0$. Therefore,

$$T_{21}(\theta) = \sqrt{3} \frac{L(\theta) - R(\theta)}{p_{zz}} \qquad (4.17)$$

and

$$A_{yy}(\theta) = -\frac{1}{\sqrt{2}} T_{20}(\theta) - \frac{\sqrt{3}}{2} T_{22}(\theta) = -2 \frac{L(\theta) + R(\theta) - 2}{p_{zz}}. \qquad (4.18)$$

Unfortunately, this method of measuring A_{yy} is sensitive to misalignment of the spin axis.

The setup for measurement of this observable was different from all of the others. The first difference was that for each angle measured, two detectors had to be placed at that angle, one at $\phi = 90°$ and the other at $\phi = -90°$, so that you had a left and right detector. This meant that measurement of the two angles, 25° and 135°, required four HPGe. Second, the electronics had to be changed to include a third "polarization state" corresponding to the case of unpolarized beam. Looking at Figure 3.8, the box labeled "Spin Controller" had to be replaced with what is shown in Figure 4.6. Approximately one second was spent in each spin state and the data taking was inhibited by the spin veto when the polarization changed for approximately 12 ms.

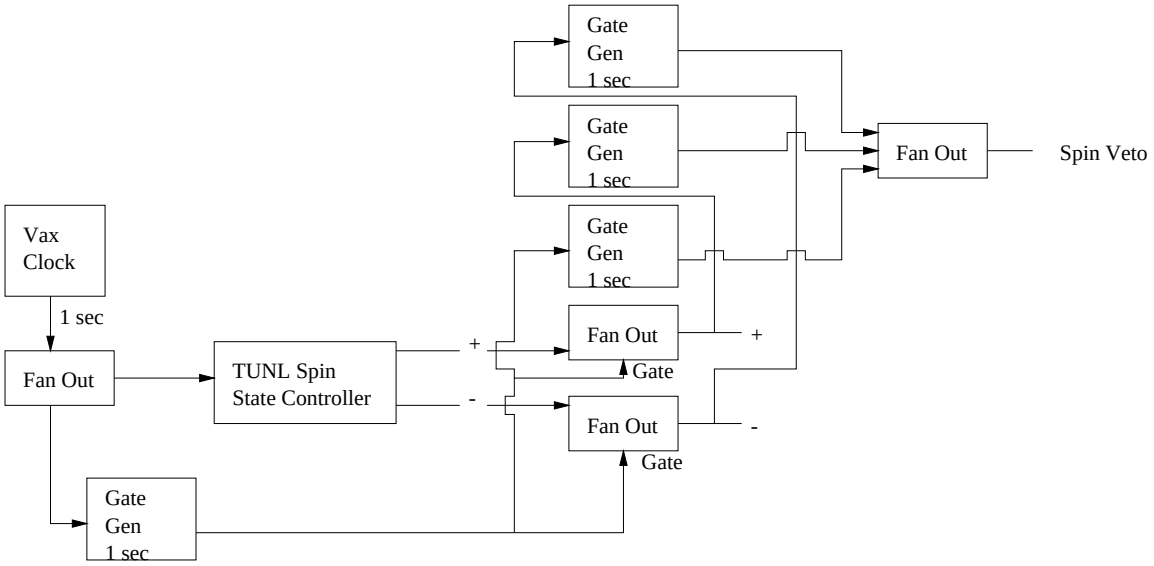

Figure 4.6: The electronics used to control three spin states used to measure T_{21}. The error bars are statistical in nature and also contain the error in the beam polarization measurements.

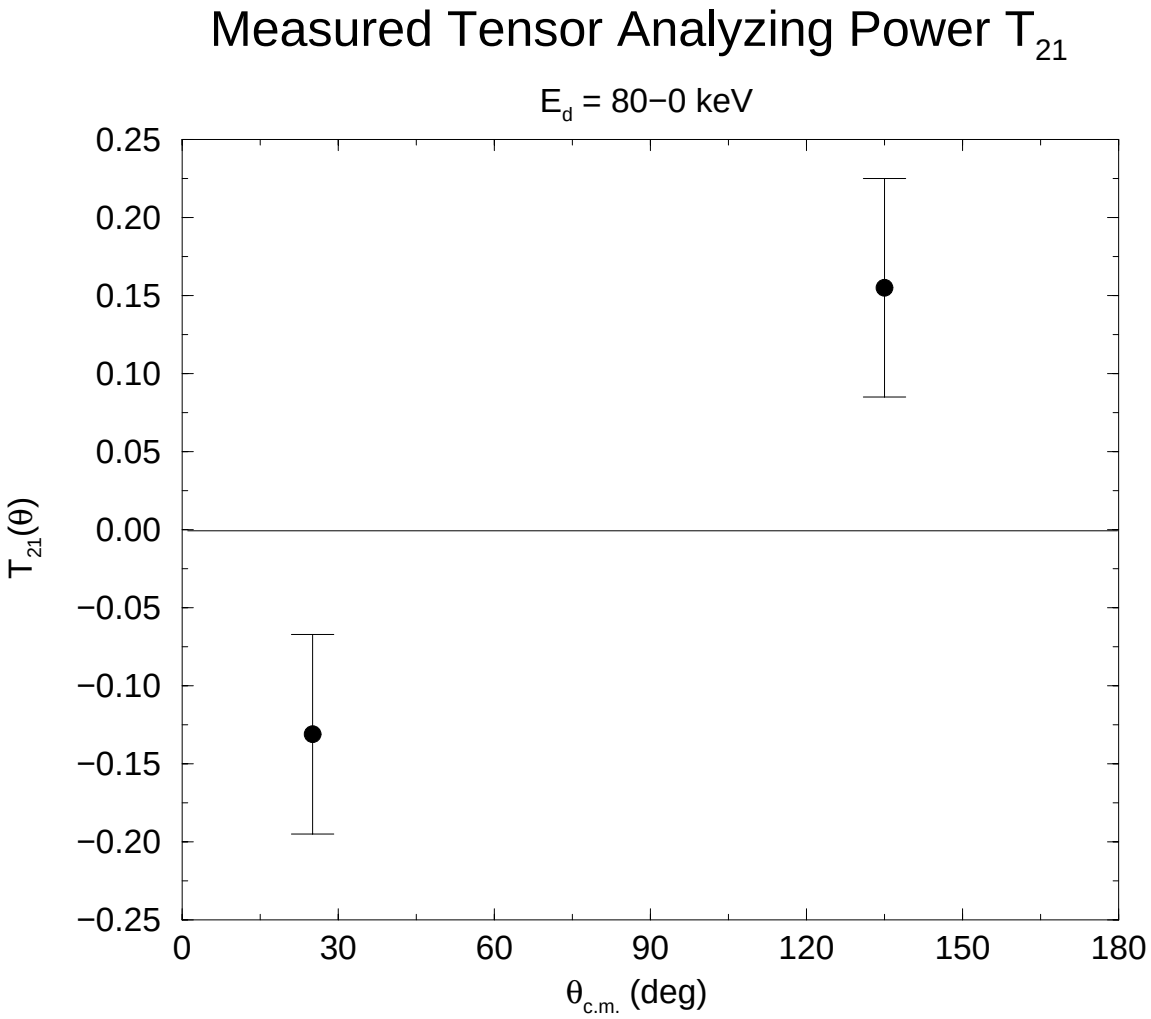

Figure 4.7: The measured $T_{21}(\theta)$ data at E_d = 80-0 keV using the second more accurate method. The error bars are statistical in nature and also contain the error in the beam polarization measurements.

One will notice that the data has measurements of $T_{21}(\theta)$ for both spin states. Therefore, the value of $T_{21}(\theta)$ for both angles is averaged over both spin states. The $T_{21}(\theta)$ data measured using this second method is presented in Table 4.8 and Figure 4.7.

$\theta_{c.m.}$	$T_{21}(\theta)$	$\Delta T_{21}(\theta)$
25.	-0.131	.064
135.	0.155	.070

Table 4.8: The measured $T_{21}(\theta)$ data at E_d = 80-0 keV using the second more accurate method. The errors are statistical in nature and also contain the error in the beam polarization measurements.

The data measured by the second method was deemed more reliable since it is not sensitive to spin axis misalignments. This is further supported by the fact that these results are consistent with the predictions made on the basis of fits to all of the other observables. The difference between the data sets is due to spin axis misalignments in the first method. There is no way to correct the data collected by the first method for spin misalignment and therefore, the data from the second method is the only one used in the data analysis.

The measurement of $A_{yy}(\theta)$ using this method yielded two data points at 25° and 135° which are shown as the first two points in Table 4.9. Combining the three angles where measurements of $T_{20}(\theta)$ and $T_{22}(\theta)$ were obtained using Equation 4.18 yields the next three data points at 45°, 90°, and 135°. The two measurements at 135° agree within errors.

$\theta_{c.m.}$	$A_{yy}(\theta)$	$\Delta A_{yy}(\theta)$
25	-0.272	0.119
135	-0.151	0.129
45	0.041	0.105
90	-0.018	0.118
135	-0.071	0.050

Table 4.9: The measured A_{yy} data at E_d = 80-0 keV. The first two data points were measured directly, but are sensitive to spin misalignments. The next three data points are from combining $T_{20}(\theta)$ and $T_{22}(\theta)$ values. The errors are statistical in nature and also contain the error in the beam polarization measurements.

4.4.4 T_{22}

The observable $T_{22}(\theta)$ is measured in much the same manner as $T_{20}(\theta)$. Equation 4.10 shows that a pure tensor polarized beam with $\beta = 54.7^\circ$ and $\phi = 0^\circ$ or 180° will only measure intensity changes from $T_{22}(\theta)$. To do this the ABPIS was tuned to the states numbered 11 and 12 from Table 3.1 to yield a beam with $p_{zz} = 1$ and -2 and no vector polarization. The problem with this state is that it reduces the intensity of the source by $\frac{1}{3}$ because the second quadrapole removes this portion of the beam. The polarization was spin flipped from $\phi = 0^\circ$ to 180° for the two spin states. The expression used to obtain $T_{22}(\theta)$ is similar to that used to obtain the other observables

$$T_{22}(\theta) = -\frac{2}{\sqrt{3}} \frac{Y_+(\theta) - Y_-(\theta)}{Y_+(\theta)p_{zz}^- + Y_-(\theta)p_{zz}^+}. \tag{4.19}$$

The measured values are given in Table 4.10 and Figure 4.8.

$\theta_{c.m.}$	$T_{22}(\theta)$	$\Delta T_{22}(\theta)$
45.	0.0588	0.0356
90.	0.1062	0.0343
135.	0.0439	0.04

Table 4.10: The measured $T_{22}(\theta)$ data at E_d = 80-0 keV. The errors are statistical in nature and also contain the error in the beam polarization measurements.

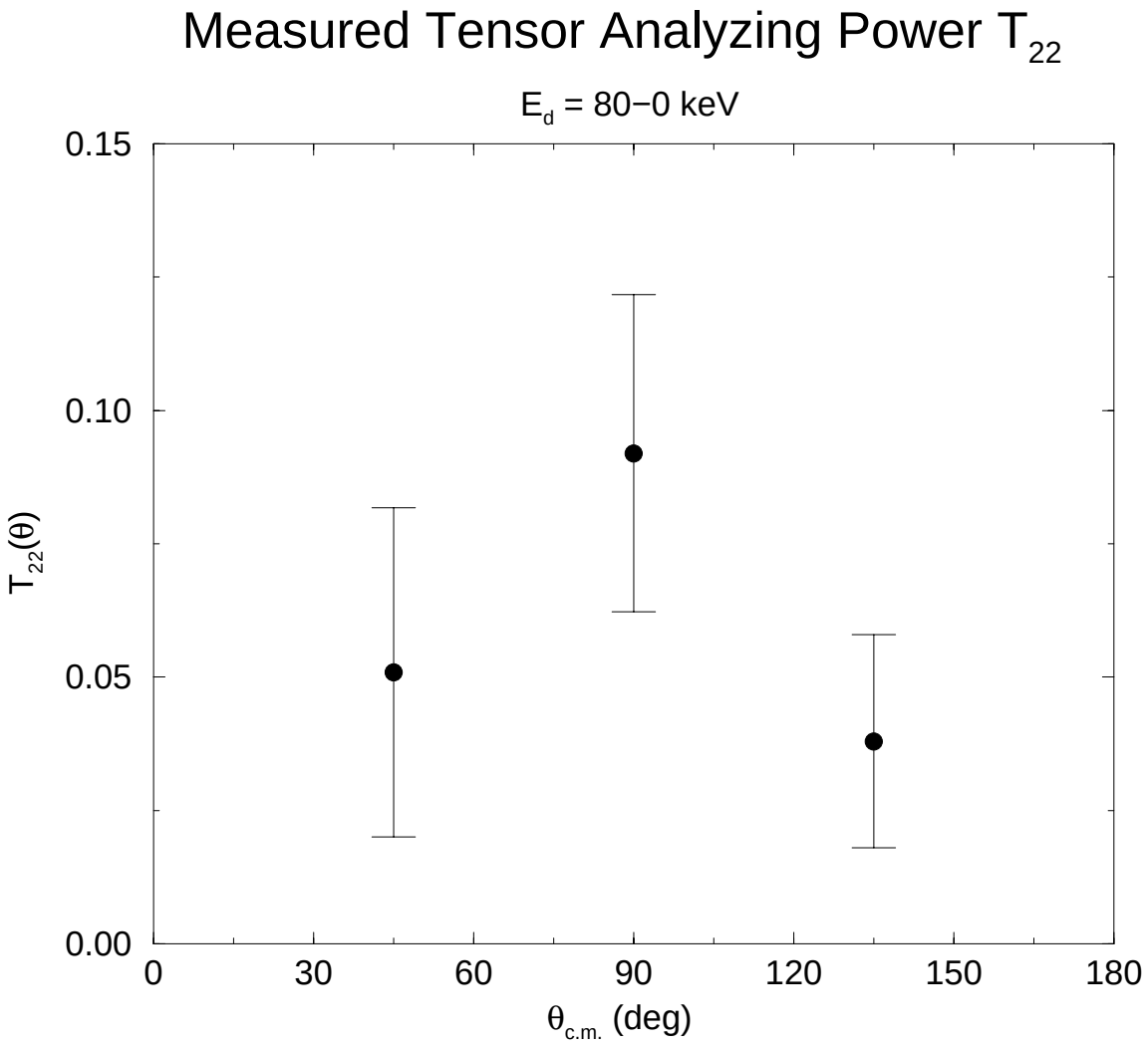

Figure 4.8: The measured $T_{22}(\theta)$ data at E_d = 80-0 keV. The error bars are statistical in nature and also contain the error in the beam polarization measurements.

Chapter 5

γ-ray Polarization

In the previous chapter, measurements of the cross section and polarized observables were discussed. There is one more observable that can be measured for the reaction, but it requires a fundamentally different method of measurement. This observable is the polarization of the γ-ray produced by the ^{2}H(p, γ)^{3}He reaction both for unpolarized and polarized protons.

5.1 Definition of γ-ray Polarization

The linear polarization of γ-rays is discussed in both [Wil74] and in [Sch95]. The definition of the γ-ray polarization P_γ is given as follows

$$P_\gamma(\theta, E_\gamma) = \frac{I_0(\theta, E_\gamma) - I_{90}(\theta, E_\gamma)}{I_0(\theta, E_\gamma) + I_{90}(\theta, E_\gamma)} \tag{5.1}$$

where $I_\phi(\theta, E_\gamma)$ is the intensity of outgoing photons with energy, E_γ, that have their electric field vector at an angle, ϕ, with respect to the reaction plane (see Figure 3.1).

Looking at a simplistic model, one can calculate the expected value of P_γ for electric dipole (E1) and magnetic dipole (M1) radiation. For E1 radiation it is reasonable to assume that the dipole is oriented in the reaction plane along the direction of propagation which means that the electric field vector is perpendicular to the direction of travel, but in the reaction plane. This means that $I_{90} = 0$ and from Equation 5.1 this shows that $P_\gamma(\theta) = 1$ for E1 radiation. For pure M1 radiation, the magnetic field vector is perpendicular to the electric field vector which means that $I_0 = 0$ and $P_\gamma(\theta) = -1$. In fact, for the ^{2}H(p,γ)^{3}He reaction, M1 radiation results from pure s-wave capture, which will be discussed in Section 6.2.1. Therefore, the dipole will have no preferred direction in space and we expect $P_\gamma(\theta) = 0$ for M1 radiation in this reaction.

The $P_\gamma(\theta)$ measured in this experiment is expected to be from a mix of both E1 and M1 radiation, with the E1 radiation dominating. Therefore, we expect to measure $P_\gamma(\theta)$ values close to 1, reflecting the ratio of E1 to M1 strength. Looking at the Transition Matrix Element (TME) expansion in Appendix B one can see that there is more to $P_\gamma(\theta)$ than this simplistic explanation.

5.2 γ-ray Polarization Analyzing Power

Another interesting quantity is the γ-ray polarization as a function of the proton polarization. This quantity is called the γ-ray polarization analyzing power, $A_\gamma(\theta)$, and is defined as follows

$$A_\gamma(\theta) = P_\gamma^+(\theta) - P_\gamma^-(\theta). \tag{5.2}$$

where P_γ^+ is the polarization of the γ-ray for the proton polarized spin up and P_γ^- for spin down. With a perfect polarized source the polarization of the beam would be

1, but in reality the values are smaller than this. Because the observable $A_\gamma(\theta)$ has a dependency on the beam polarization a theoretical comparison must contain the beam polarization from the experiment. This observable then yields more information about the reaction.

The simple expression which one might expect to use to relate the unpolarized γ-ray polarization, P^0_γ, to the average of the polarized $(P^+_\gamma + P^-_\gamma)/2$ is not true. The relationship actually involves the vector analyzing power $A_y(\theta)$ and is given by

$$P^0_\gamma(\theta) = \frac{(1 + f^+ A_y(\theta))\, P^+_\gamma(\theta) + (1 - f^- A_y(\theta))\, P^-_\gamma(\theta)}{2 + (f^+ - f^-)\, A_y(\theta)} \tag{5.3}$$

where f^+ is the polarization of the beam spin up and f^- is for spin down. If either the polarization of the beam or $A_y(\theta)$ is zero, then $P^0_\gamma(\theta)$ reduces to the average of the polarized $P_\gamma(\theta)$.

5.3 Compton Polarimeter

A Compton Polarimeter was employed to measure the polarization of the γ-rays produced by the reaction. This device is sensitive to the orientation of the γ-ray polarization vector and consists of a 128% HPGe detector as a central scatterer surrounded by four 60% HPGe detectors.

The expression for the differential cross section for Compton scattering of a polarized photon is given by the Klein-Nishina formula which can be written as follows [Eva55, Wil74]:

$$d\sigma(\theta_c, \eta) = \frac{r_0^2}{2} \frac{E'^2_\gamma}{E^2_\gamma} \left[\frac{E_\gamma}{E'_\gamma} + \frac{E'_\gamma}{E_\gamma} - 2 \sin^2\theta_c \cos^2\eta \right] d\Omega. \tag{5.4}$$

where Equation 5.4 is summed over all polarization directions of the scattered photon

because the only polarization of interest is that of the incident photon. The symbols from the equation are defined below:

- $r_0 \equiv \frac{e^2}{m_e c^2}$ = the "classical electron radius", where m_e is the mass of the electron.
- $d\Omega$ = the solid angle into which the photon is scattered.
- θ_c = the "Compton Scattering Angle", the angle between the incident photon and the Compton scattered photon.
- η = the angle between the electric field vector of the incident photon and the plane containing the Compton scattered photon.
- E_γ = energy of the incident photon
- E'_γ = energy of the Compton scattered photon related to E_γ by Equation 3.6.

Looking at Equation 5.4, it is clear that the cross section is maximized for $\eta = 90^\circ$ and is minimized for $\eta = 0^\circ$. This means that if a γ-ray from an electric dipole (E1) transition in from the $^2H(p,\gamma)^3He$ reaction has its electric field vector in the reaction (x-z) plane ($\phi = 0^\circ$) then the Compton scattered γ-ray will be more likely to be scattered along the y-axis because $\eta = 90^\circ$. On the other hand, an E1 γ-ray with $\phi = 90^\circ$ is more likely to scatter in the reaction plane of the $^2H(p,\gamma)^3He$ reaction since $\eta = 90^\circ$. The azimuthal angle is determined in [Wul99] Equation 13 and it is shown that $\phi = 0$ for an unpolarized beam or a beam polarized along the $\hat{y}$ axis, which was used in this experiment. Therefore, the Compton polarimeter measures the asymmetry between Compton scattering events in the horizontal (x-z) plane (reaction plane) versus the vertical (x-y) plane as seen in Figure 5.1. The asymmetry

$$A(\theta, E_\gamma) = \frac{N_v(\theta, E_\gamma) - N_h(\theta, E_\gamma)}{N_v(\theta, E_\gamma) + N_h(\theta, E_\gamma)}, \tag{5.5}$$

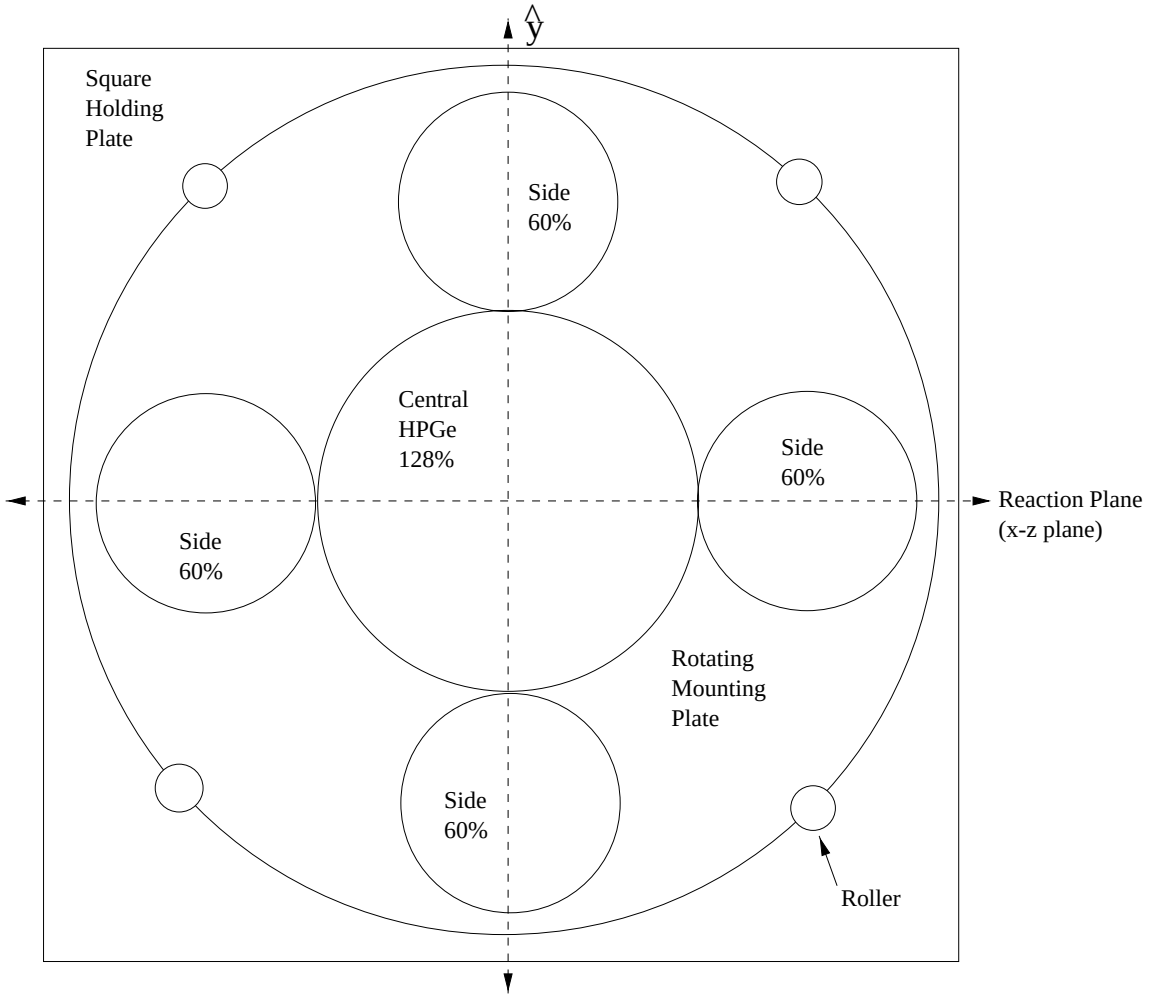

Figure 5.1: A head on view of the Compton polarimeter showing the location of the five detectors as well as the relevant axes.

between the number of Compton scattered γ-rays seen in the detectors horizontally oriented, $\mathrm{N}_h(\theta, \mathrm{E}_\gamma)$, and the those oriented vertically, $\mathrm{N}_v(\theta, \mathrm{E}_\gamma)$. $\mathrm{N}_v(\theta, \mathrm{E}_\gamma)$ and $\mathrm{N}_h(\theta, \mathrm{E}_\gamma)$ can be expressed in terms of $\mathrm{I}_0(\theta, \mathrm{E}_\gamma)$ and $\mathrm{I}_{90}(\theta, \mathrm{E}_\gamma)$ from Equation 5.1,

$$\begin{aligned} \mathrm{N}_v(\theta, \mathrm{E}_\gamma) &= \mathrm{I}_0(\theta, \mathrm{E}_\gamma)\mathrm{d}\sigma(\theta_c, \eta = 90^\circ, \mathrm{E}_\gamma) + \mathrm{I}_{90}(\theta, \mathrm{E}_\gamma)\mathrm{d}\sigma(\theta_c, \eta = 0^\circ, \mathrm{E}_\gamma) \\ \mathrm{N}_h(\theta, \mathrm{E}_\gamma) &= \mathrm{I}_0(\theta, \mathrm{E}_\gamma)\mathrm{d}\sigma(\theta_c, \eta = 0^\circ, \mathrm{E}_\gamma) + \mathrm{I}_{90}(\theta, \mathrm{E}_\gamma)\mathrm{d}\sigma(\theta_c, \eta = 90^\circ, \mathrm{E}_\gamma) \end{aligned} \tag{5.6}$$

where $\mathrm{d}\sigma(\theta, \mathrm{E}_\gamma)$ is given by Equation 5.4. Using Equation 5.6 and Equation 5.5 we

get:

$$\mathrm{A}(\theta, \mathrm{E}_\gamma) = \left(\frac{\mathrm{d}\sigma(\theta_c, \eta = 90^\circ, \mathrm{E}_\gamma) - \mathrm{d}\sigma(\theta_c, \eta = 0^\circ, \mathrm{E}_\gamma)}{\mathrm{d}\sigma(\theta_c, \eta = 90^\circ, \mathrm{E}_\gamma) + \mathrm{d}\sigma(\theta_c, \eta = 0^\circ, \mathrm{E}_\gamma)} \right) \left(\frac{\mathrm{I}_0(\theta, \mathrm{E}_\gamma) - \mathrm{I}_{90}(\theta, \mathrm{E}_\gamma)}{\mathrm{I}_0(\theta, \mathrm{E}_\gamma) + \mathrm{I}_{90}(\theta, \mathrm{E}_\gamma)} \right) \tag{5.7}$$

The second part of Equation 5.7 is just $\mathrm{P}_\gamma(\theta, \mathrm{E}_\gamma)$ defined in Equation 5.1 and the first quantity is a factor that is called the polarization sensitivity, $\mathrm{S}(\mathrm{E}_\gamma)$. This means that Equation 5.7 can be written

$$\mathrm{P}_\gamma(\theta, \mathrm{E}_\gamma) = \frac{\mathrm{A}(\theta, \mathrm{E}_\gamma)}{\mathrm{S}(\mathrm{E}_\gamma)}. \tag{5.8}$$

Now the asymmetry in the Compton polarimeter, $\mathrm{A}(\theta, \mathrm{E}_\gamma)$, can be used to determine the polarization of the γ-rays once the polarization sensitivity is determined. Using the Klein-Nishina equation (Equation 5.4) the sensitivity can be rewritten

$$\mathrm{S}(\mathrm{E}_\gamma) = \frac{\sin^2 \theta_c}{\frac{\mathrm{E}_\gamma}{\mathrm{E'}_\gamma} + \frac{\mathrm{E'}_\gamma}{\mathrm{E}_\gamma} - \sin^2 \theta_c}. \tag{5.9}$$

If one assumes that the detectors are point detectors, Equation 5.9 is only non-zero when $\theta_c = 90^\circ$. Therefore, for point detectors, Equation 5.9 becomes

$$\mathrm{S}(\mathrm{E}_\gamma) = \frac{1}{\frac{\mathrm{E}_\gamma}{\mathrm{m}_e c^2} + \frac{\mathrm{m}_e c^2}{\mathrm{E}_\gamma + \mathrm{m}_e c^2}}. \tag{5.10}$$

This result would allow us to measure the polarization of γ-rays with a polarimeter made of point detectors. Unfortunately, to measure the polarization with real detectors that have finite extent the sensitivity has to be measured experimentally.

5.3.1 Polarization Sensitivity

Solving Equation 5.8 for the polarization sensitivity, $\mathrm{S}(\mathrm{E}_\gamma)$, shows that to experimentally measure this quantity one needs to measure the asymmetries, $A(\theta, \mathrm{E}_\gamma)$, for

γ-rays of known polarization. The production of γ-rays of known polarization is not trivial, but the easiest method available was nuclear reactions. Two nuclear reactions with γ-rays at $E_\gamma = 1.78$ and 4.43 MeV, having previously determined polarizations, were used.

The first reaction was the $^{28}Si(p,p'\gamma)^{28}Si$ reaction which produces a 1.78 MeV γ-ray when protons accelerated to $E_p(lab) = 3.1$ MeV excite the ^{28}Si. The target used for this reaction was a thin ^{12}C foil with a layer of ^{28}Si evaporated on to it. The polarization of the γ-rays produced by this reaction have been measured by [Sch95, Wil74, Bas72, Lit70] at 90°. The measurements are, in order, $P_\gamma(90°) = 1.07 \pm 0.08$, $P_\gamma(90°) = 0.80 \pm 0.03$, $P_\gamma(90°) = 0.74 \pm 0.04$, and $P_\gamma(90°) = 0.82 \pm 0.03$. This comes to a weighted average of $P_\gamma(90°) = 0.81 \pm 0.05$ which is used in the following analysis. This differs from the work of Schmid *et al.* [Sch95, Sch97] where the value of $P_\gamma(90°) = 1.07 \pm 0.08$ was used even though it was significantly different from the other measurements and indicates an unphysical measurement greater than 1. This is of interest because the measurements of P_γ done by Schmid *et al.* are used in the analysis of the TMEs.

The other reaction used was the $^{12}C(p,p'\gamma)^{12}C$ reaction which produces a 4.43 MeV γ-ray when a proton beam of $E_p(lab) = 5.37$ MeV is used. The target used for this reaction was a thin ^{12}C foil. The polarization of this reaction was measured by [Sch95, Wil74, Bas72, Lit70] and their values are, respectively, $P_\gamma(90°) = 0.88 \pm 0.04$, $P_\gamma(90°) = 0.97 \pm 0.02$, $P_\gamma(90°) = 0.80 \pm 0.06$, and $P_\gamma(90°) = 1.10 \pm 0.06$. A weighted average was again used and has a value of $P_\gamma(90°) = 0.95 \pm 0.02$.

The values measured at $E_\gamma = 1.78$ MeV and 4.43 MeV are used to extrapolate a value at $E_\gamma = 5.5$ MeV, the γ-ray energy from the $^2H(p,\gamma)^3He$ reaction. The sensitivity is not expected to change rapidly between 4.43 MeV and 5.5 MeV [Wil74]

so the energy dependent form of the extrapolation should not be too important. The best form would be to average Equation 5.9 over the finite geometry of the detectors. Because of the insensitivity to the energy dependence, this complicated method was not employed and the point geometry Equation 5.10 was used. An overall normalization constant, C, multiplied Equation 5.10 and was varied until the χ^2 for the function was minimized. The equation we are trying to solve is linear with respect to C so the χ^2 minimization reduces to solving

$$\frac{d\chi^2}{dC} = 0 \tag{5.11}$$

for C. The error on this value can be determined by finding the increment in C that causes χ^2 to change by one. From this information the sensitivity at 5.5 MeV can then be determined.

The Compton polarimeter used by Schmid *et al.* was the 128% HPGe surrounded by a NaI annulus. The sensitivity was measured to be S(4.43) = 0.041 ± 0.003 in [Sch95, Sch97] and this value has been adjusted with the weighted value of P_γ to S(4.43) = 0.038 ± 0.004. The previously published value of S(1.78) = 0.100 ± 0.008 [Sch95, Sch97] has been adjusted to S(1.78) = 0.132 ± 0.005. The previously published fit to the data gave C = 0.034 ± 0.0034 [Sch95, Sch97] which yielded S(5.5) = 0.034 ± 0.0034. Using the weighted values of P_γ at 1.78 and 4.4 MeV, a value of C = 0.455 ± 0.016 which yields S(5.5) = 0.042 ± 0.0042 is found. This new value of the sensitivity for the "Schmid" polarimeter was used to correct the $P_\gamma(\theta)$ data gathered by Schmid *et al.* [Sch95, Sch97].

For the polarimeter used in the current experiment, the sensitivity was found to be S(1.78) = 0.17 ± .01 and S(4.43) = 0.08 ± .004. This yields C = 0.646 ± 0.017 and S(5.5) = 0.060 ± 0.006. You can see in Figure 5.2 that the fit describes the data points well.

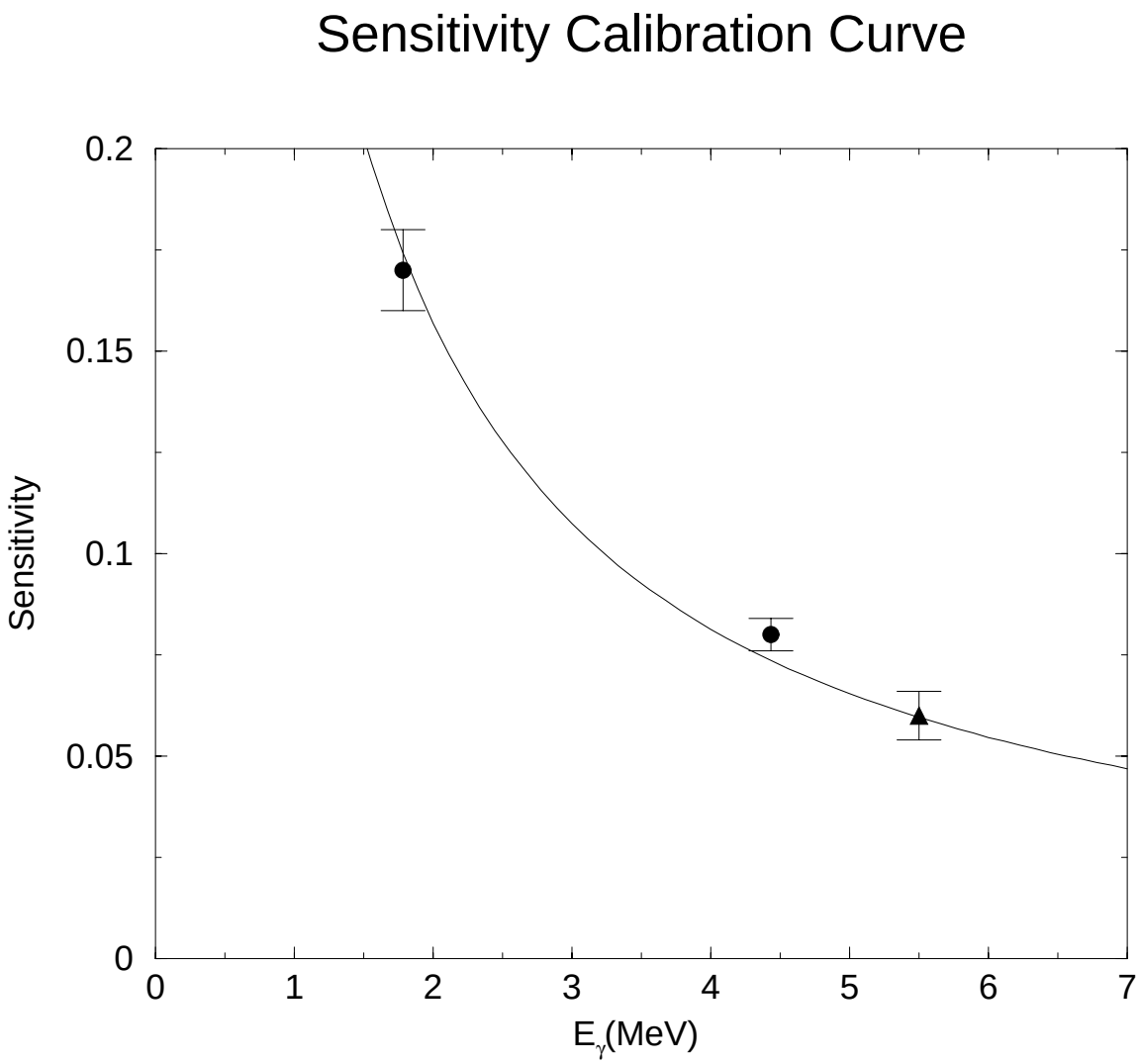

Figure 5.2: The fit of the measured sensitivities (circles) and the extracted point at 5.5 MeV (triangle). The error bars include the error on the polarization of the γ-ray and the statistical error in the measurement.

5.4 Measuring γ-ray Polarization

With the sensitivity of the polarimeter known at 5.5 MeV, measuring the polarization of the γ-rays from the $^2\mathrm{H}(\vec{\mathrm{p}},\gamma)^3\mathrm{He}$ reaction requires that only the asymmetry $\mathrm{A}(\theta)$ be measured as a function of the outgoing γ-ray angle θ. Measuring the difference in Compton scattering between the horizontal and vertical plane is simple, but ridding the measurement of contaminants is more difficult.

The Compton polarimeter is placed at the angle of interest as close to the target chamber as possible. To help cancel out instrumental asymmetries in the polarimeter, such as efficiency differences and misalignments, the detectors were rotated periodically so that the horizontal detectors become the vertical detectors. Looking at Figure 5.1, one can see that the side detectors can be rotated around the central detector. During a run, the detectors had to be filled with liquid Nitrogen (LN_2) every 12 hours and this was deemed a good time to rotate the detectors by 90°. The numbers measured in the vertical and horizontal plane were averaged over the two different orientations.

The count rate of the polarimeter is fairly low because only γ-rays that Compton scatter and deposit energy in the center detector and one side detector are counted. To increase the count rate, events that Compton scatter in a side crystal and deposit energy in the center crystal are allowed as well. This increases the count rate substantially while increasing the angular spread of the detected capture γ-rays which the polarimeter is averaging over.

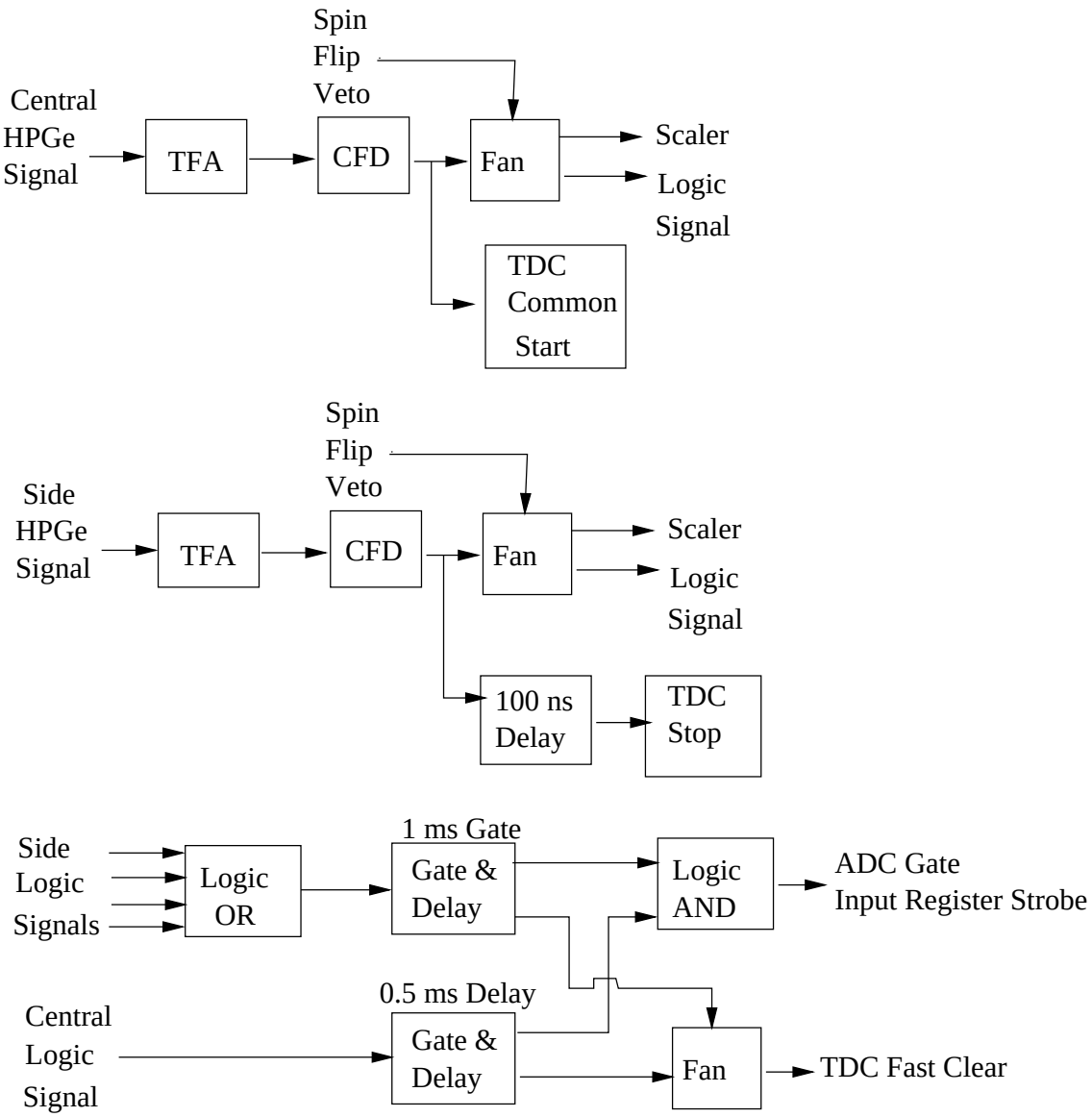

Figure 5.3: The essential electronics for the Compton polarimeter.

5.4.1 Electronics

The electronics for the Compton polarimeter are significantly more complicated than those shown for individual HPGe in Figure 3.8. One of the outputs from each of the five HPGe is fed into a spectroscopy amplifier and the unipolar output is sent directly to an ADC. The other copy of the HPGe output is connected to a TFA whose output is connected to a CFD (see Figure 5.3). Each CFD has 100 ns of delay attached. The settings of their thresholds as well as the TFA gains are described below. One copy of the CFD logic signal for the side detectors is then delayed 400 ns and sent directly to the TDC's stop inputs. The other copy of the CFD logic pulse along with the central detector's CFD output are fanned out. If the run is done with a polarized beam, the spin flip veto signal is connected to this fan out module which inhibits all output logic signals for 7 ms. One output of the fan for each detector is connected to a scaler. For the side detectors another fan output is sent into a logical OR which means that the output fires whenever there is a logic signal from any of the four side detectors. The output of this OR is sent to a gate and delay generator that creates a 1 ms long gate. This gate is logic ANDed with the central detector signal that has been delayed by 500 ns. The output of this AND is used to trigger the ADC and is the main electronics gate. A negated version of the AND is used as a Fast Clear for the TDC.

To eliminate low energy events, the lower energy cut off was set by the CFD and TFA. The TFA amplification and CFD levels were set so that the lowest energy pulse allowed to trigger the data acquisition system was 150 keV (see Figure 5.4). This limit is set based on the fact that the lowest energy γ-ray emitted from Compton scattering at 5.5 MeV is equal to 244 keV at 180°(Equation 3.6). This hardware cut reduces the number of events that the computer system has to record. More severe

cuts can be added offline.

There must be a coincidence between a side detector and the central detector for the event to be of interest since a γ-ray has to Compton scatter in the central crystal and then the scattered γ-ray has to leave some energy in a side crystal (or the other way around). The coincidence is accomplished in two ways. First, the main electronics gate, described above, cuts out many events before the computer digitizes them. Second, a time spectrum is also acquired using a Time to Digital Converter (TDC). This module starts counting when it receives a signal from the central detector. Each side detector has a logic signal delayed by 400 ns and this signal is fed into 4 of the TDC's stop inputs. The TDC is set to 800 ns full scale. Therefore, a coincidence within 800 ns between the central detector and a side detector should show up as a peak in the center of the spectrum. The TDC is started with every logic pulse from the central detector, but data is only acquired every time there is a coincidence between the center and a side detector. Therefore, the TDC has to be reset every time there is a event in the center crystal without an event in the side crystal so that the null event in the TDC is not stored. This is accomplished by the Fast Clear signal described above.

5.4.2 Online Data Analysis

The online data analysis has more substantial cuts to reduce the number of events that are not created by Compton scattering. The first cut checks for a coincidence registered by the TDC spectrum (see Figure 5.5) for each side detector (see Figure 5.6). The next cut makes sure that the energy deposited in the central HPGe is between 200 keV and 5350 keV and is not between 505 keV and 517 keV. The first cut eliminates, by energy, events that could not have occurred by Compton scattering.

The second cut removes events that were caused by first and second escape events (i.e. 511 keV escapes from the scattering crystal). After the cut on the center detector, each side crystal is checked for the same energy cuts.

The next cuts are based on reconstructing the Compton scattering angle (see Figure 5.7). Events scattered from the central detector into the side detectors or from a side detector into the central detector are allowed. The energy of the incident γ-ray are known to within a few keV and the energy deposited in each of the detectors is known. From this information we can calculate the Compton scattering angle, θ_c, both if the γ-ray scattered in the central crystal or the side crystal. Then any events that do not have real angles are removed (see Figure 5.8).

Finally, if more than one side crystal and center crystal pair have events that satisfy all the cuts, then the event is removed since it is not possible to have a valid event in more than one detector pair (see Figure 5.9). Finally, the energy deposited in the central crystal and the energy deposited in the side crystal were summed together to produce the final reconstructed spectrum (see Figure 5.10). The energy resolution is still very good and we can now see how many events fall into the photopeak. From this information the horizontal-vertical asymmetry and the polarization of the γ-rays can be calculated.

5.5 Measured Values

The unpolarized $P_\gamma(\theta)$ measurements presented in Figure 5.11 were performed by Schmid *et al.* [Sch95, Sch97] except for one measurement at 90° performed with the new polarimeter. The measurements in [Sch97] have been corrected with the weighted sensitivity as described in Section 5.3.1, and are given in Table 5.1 and Figure 5.11.

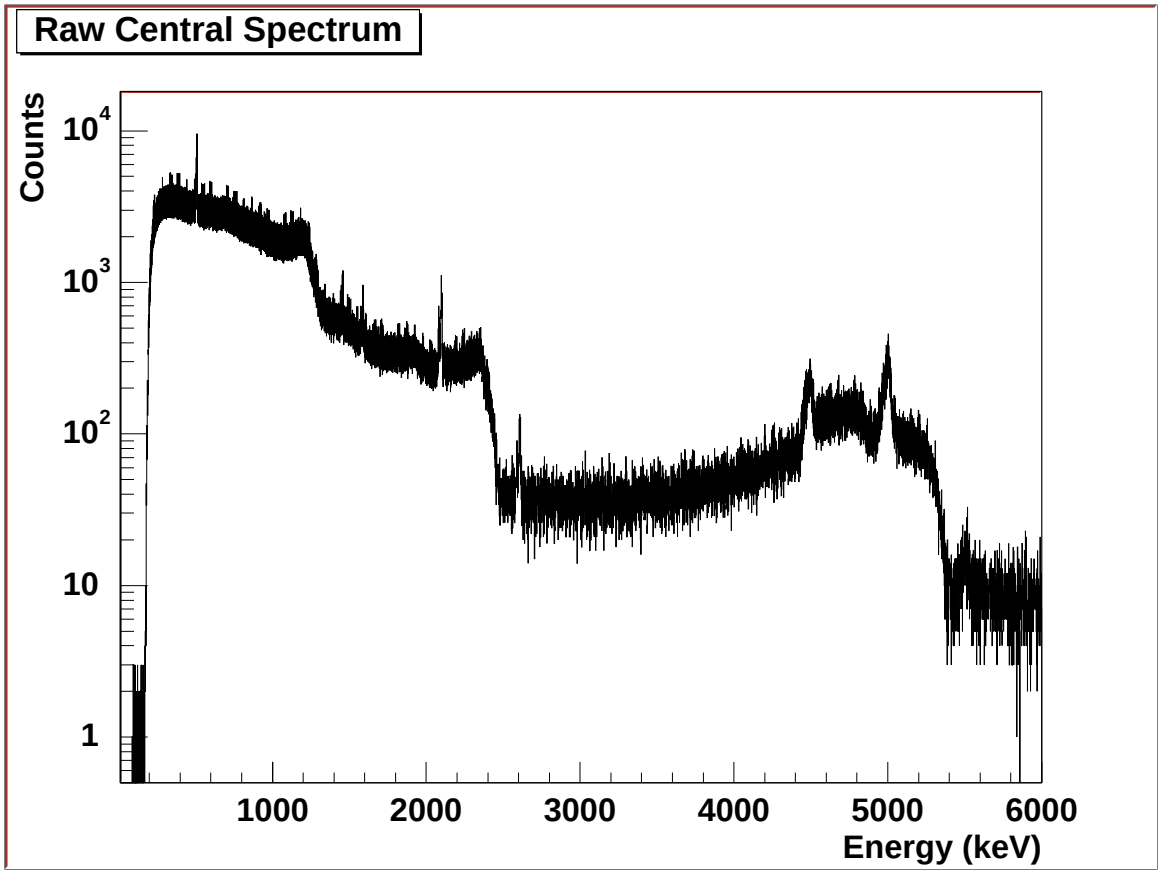

Figure 5.4: The raw spectrum from the central detector in the Compton polarimeter. The photopeak is small while the Compton edge and first and second escape peak are emphasized. The 511 keV line is quite large.

The polarized measurement of the γ-ray polarization analyzing power, $A_\gamma(\theta)$, was only performed at 90° due to time constraints. The one data point took three weeks to measure and yielded a value of $A_\gamma(90°) = 0.134 \pm 0.095$ from Equation 5.2. The average polarization of the proton beam during these runs was 0.55 ± 0.05 and -0.70 $\pm$ 0.05 for f^+ and f^-, respectively.

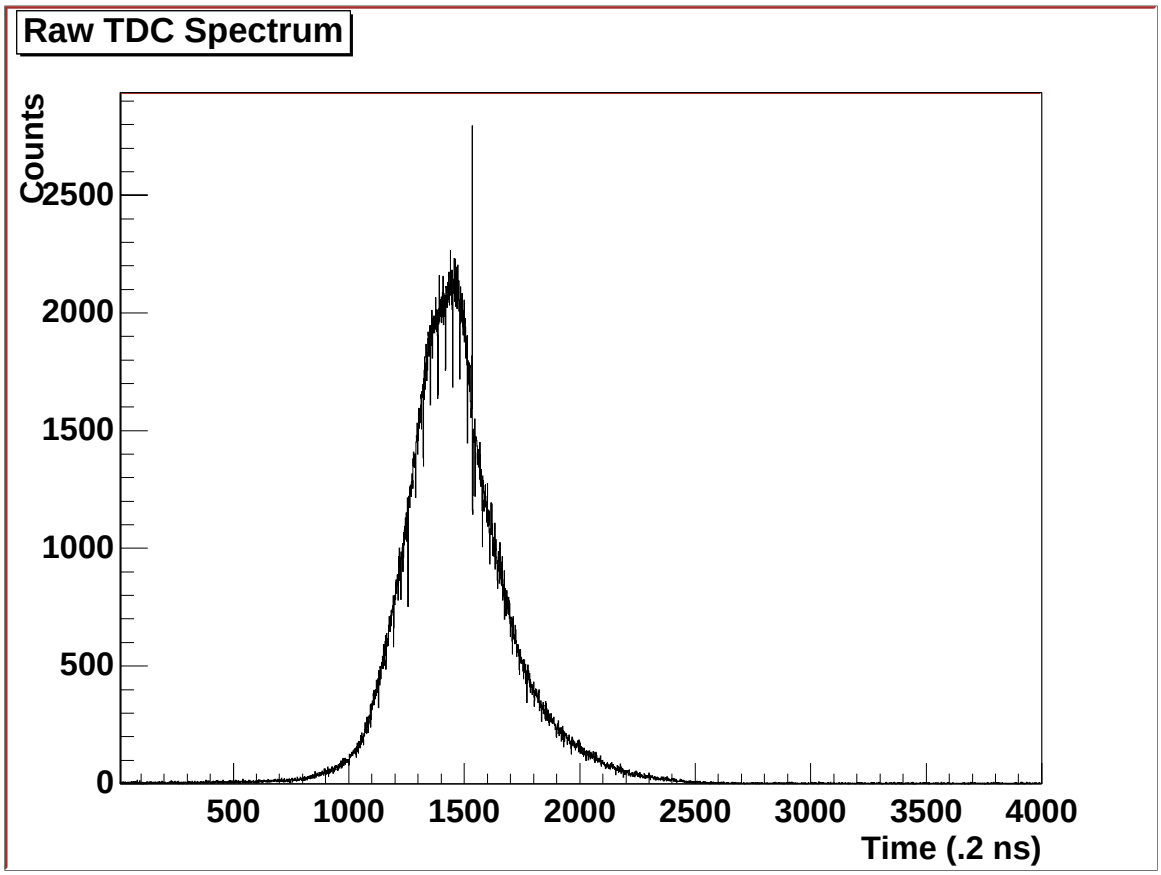

Figure 5.5: The TDC spectrum for one side detector in the Compton polarimeter.

$\theta_{c.m.}$	$P_\gamma(\theta)$	$\Delta P_\gamma(\theta)$
30.8	0.45	0.21
60.4	0.64	0.27
91.0	0.86	0.23
120.2	0.64	0.30
90	0.652	0.10

Table 5.1: The first four values of P_γ as measured in [Sch97] and the last value measured with the 5 HPGe polarimeter. The values at 90° agree within error. The errors are statistical in nature and also contain the error in the beam polarization measurements.

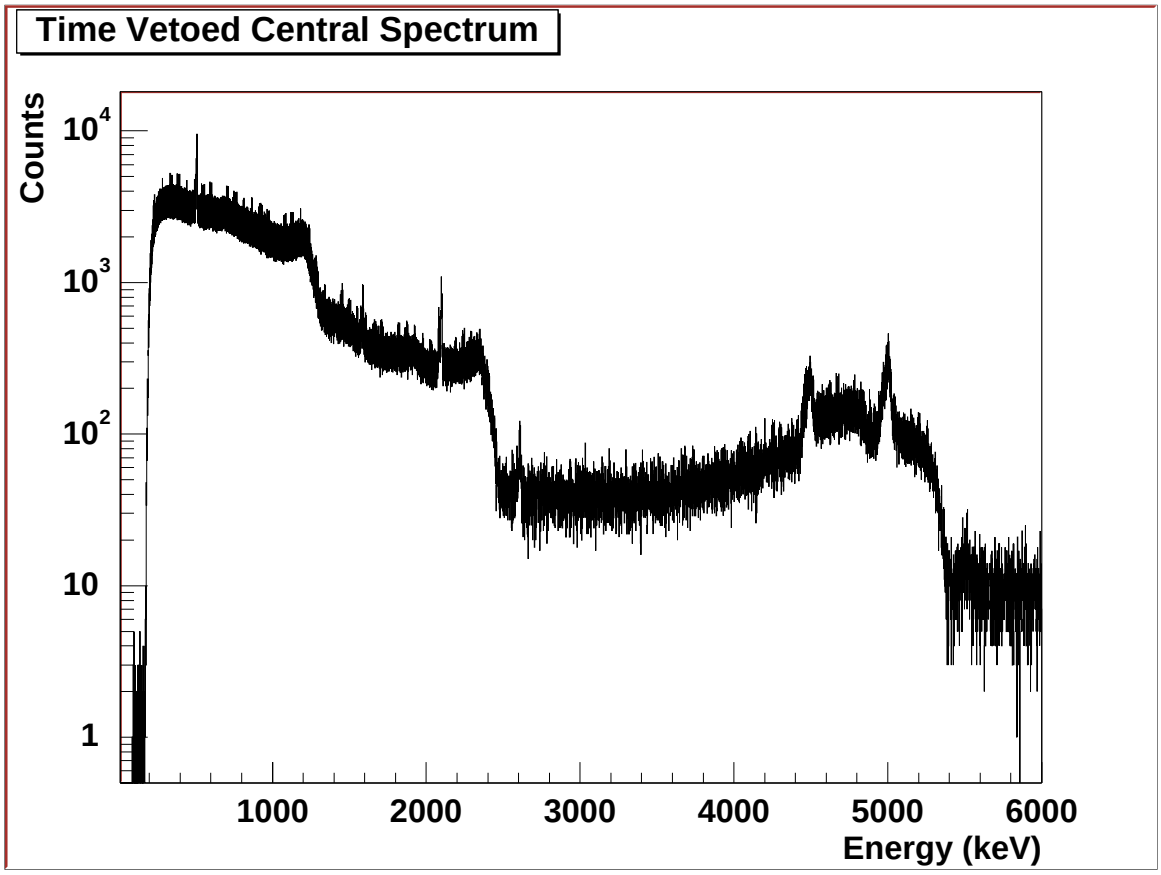

Figure 5.6: The spectrum from the central detector after the cut on the TDC. There is little difference between this spectrum and Figure 5.4. This is due to the hardware gate that eliminates most events that are not in coincidence.

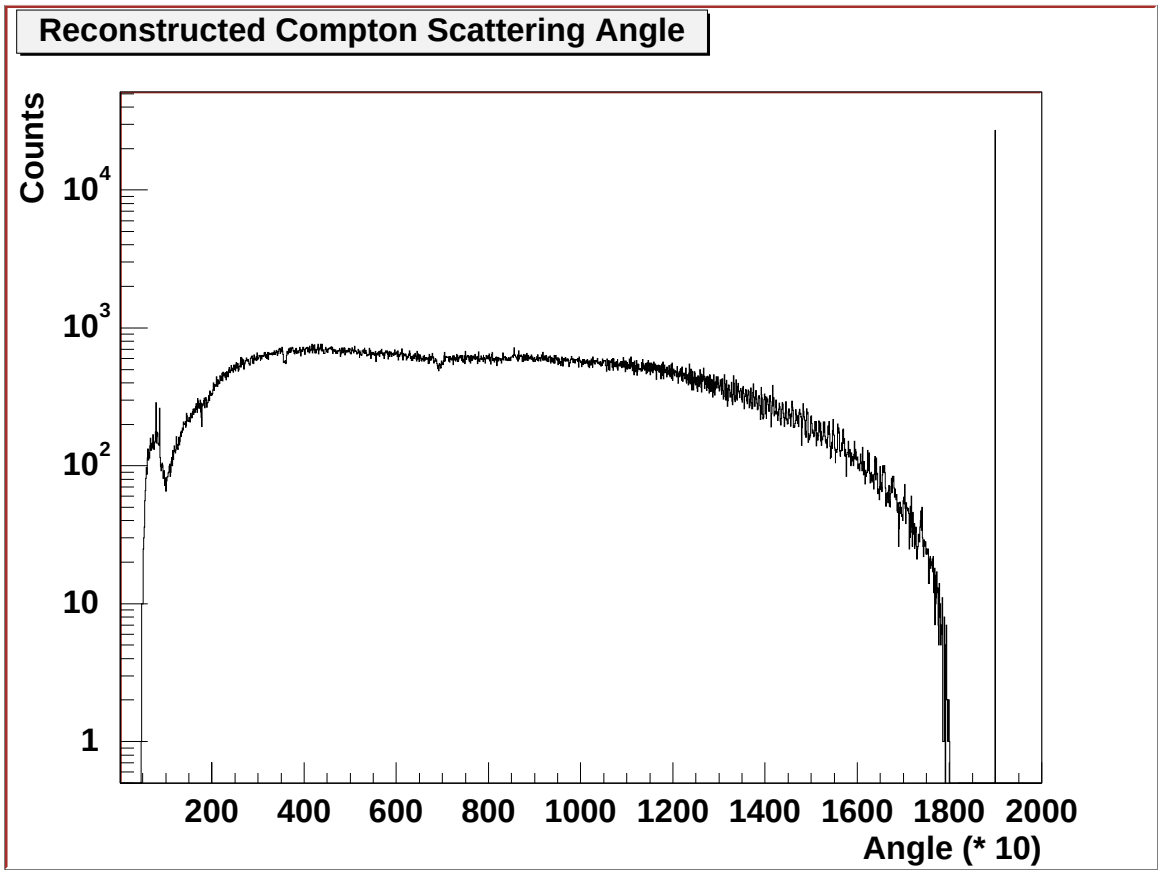

Figure 5.7: The reconstructed Compton angle multiplied by 10. The peak at 1900 is where the software places events that do not reconstruct to real angles.

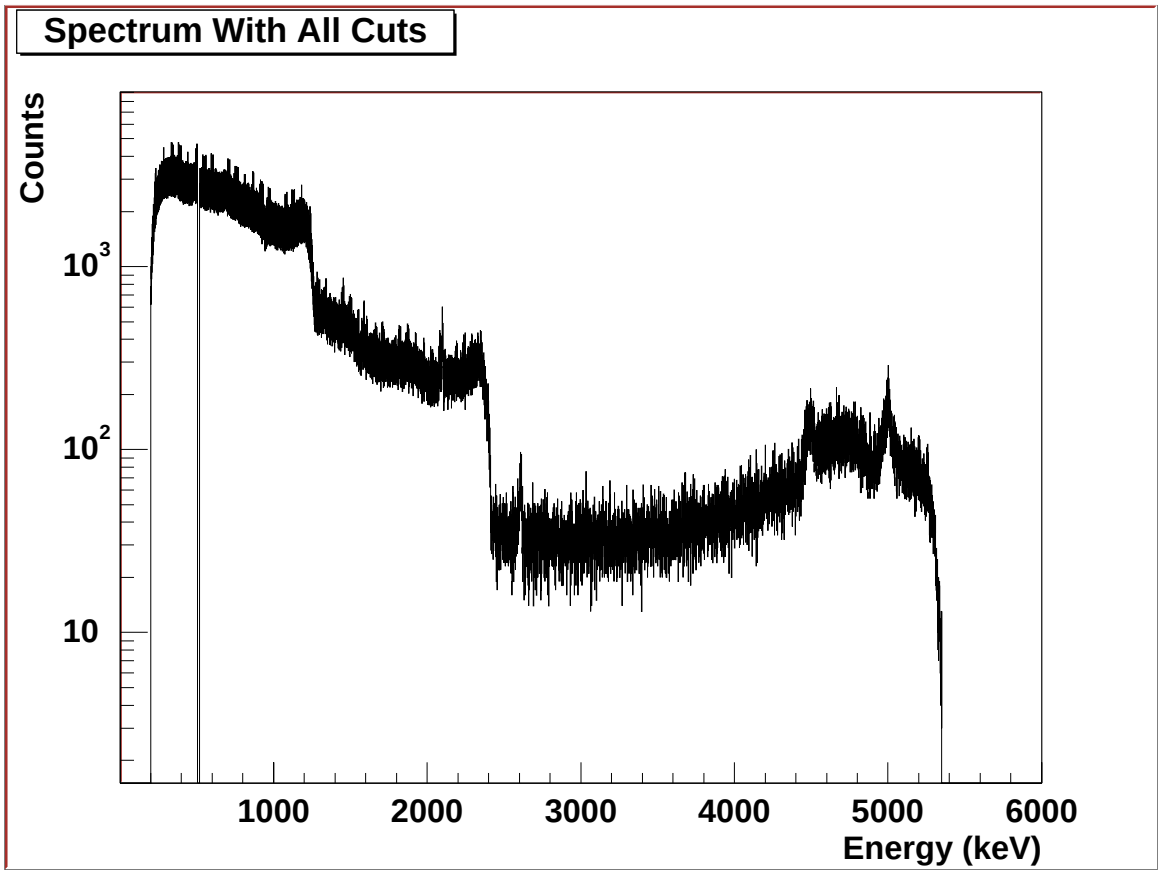

Figure 5.8: The spectrum after all cuts except for the multiplicity check. The 511 keV peak is gone and there are no events over 5350 keV.

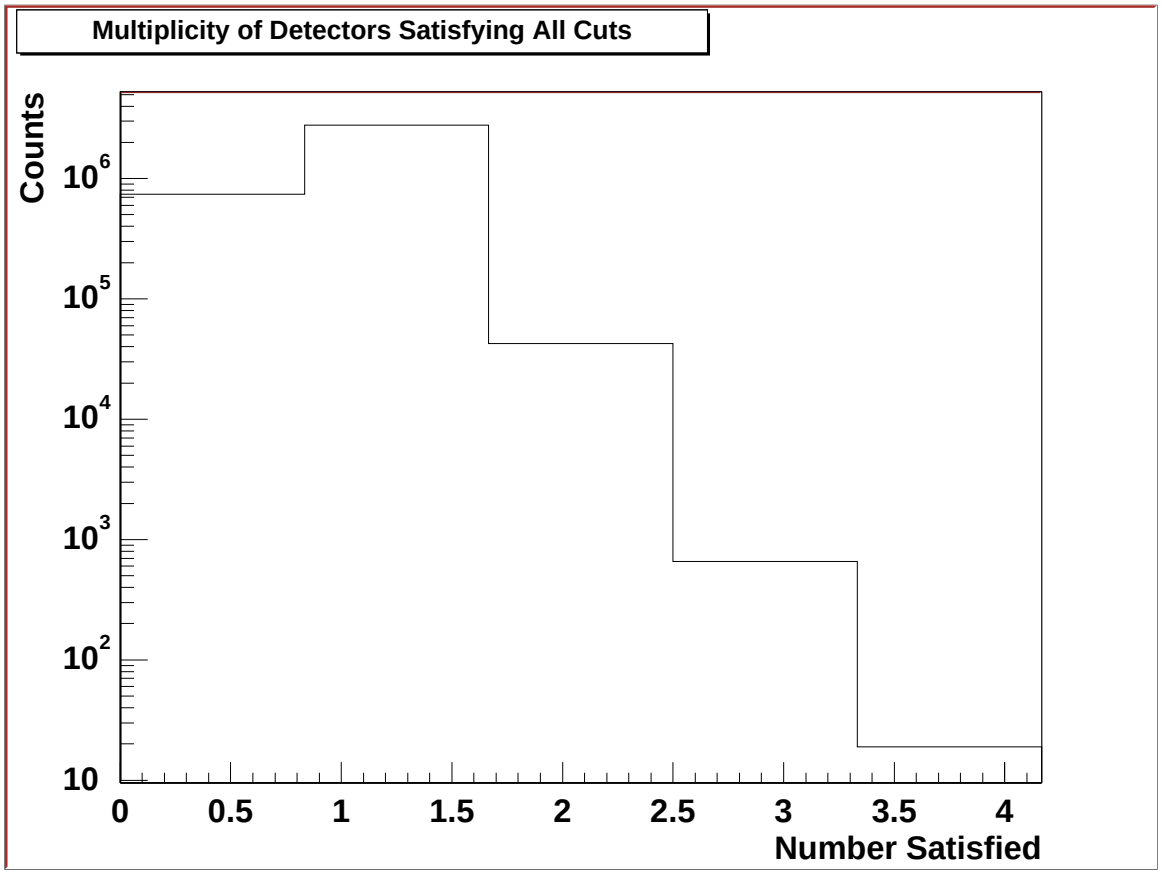

Figure 5.9: The number of detector pairs that satisfy all cuts. Only events with a multiplicity of 1 are used. There are nearly as many events in which no detector satisfies all cuts.

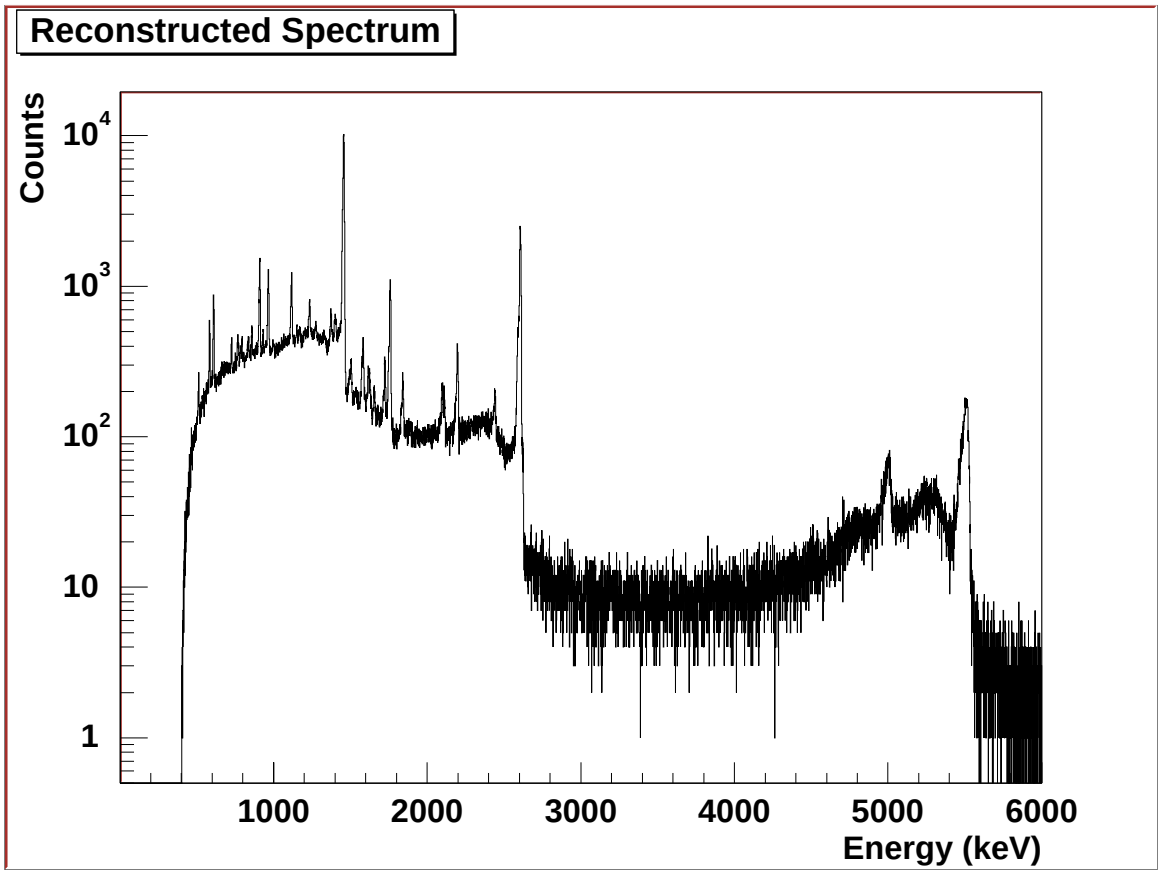

Figure 5.10: The final reconstructed spectrum. The second escape peak is completely eliminated and the energy resolution of the spectrum is still excellent.

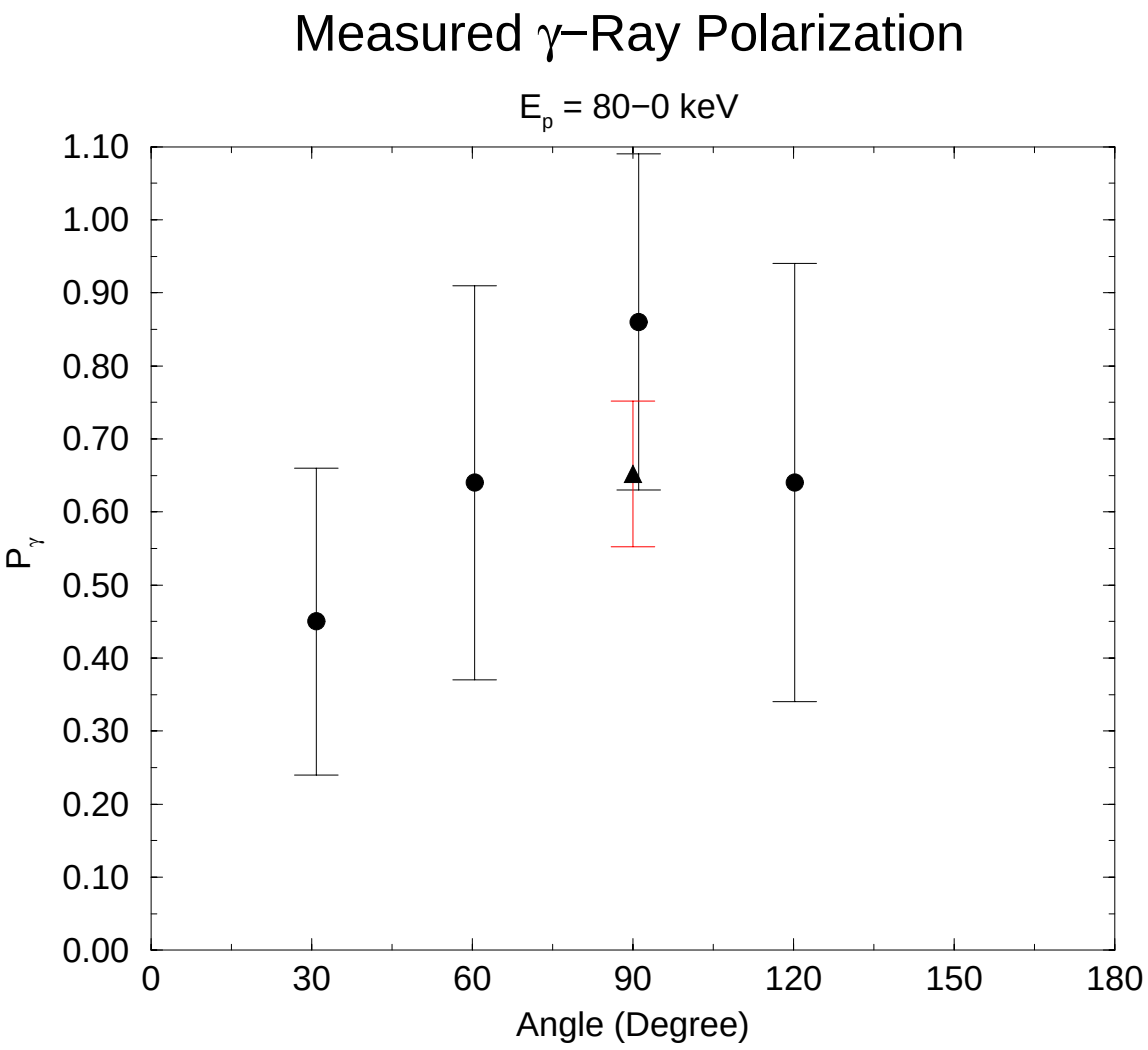

Figure 5.11: The circle data points of P_γ as measured in [Sch97] and the triangular point measured with the 5 HPGe polarimeter. The error bars are statistical in nature and also contain the error in the beam polarization measurements.

Chapter 6

Analysis Results

The observables presented in the previous two chapters compromise the most complete data set ever obtained for the $^2\mathrm{H}(\vec{\mathrm{p}},\gamma)^3\mathrm{He}$ and $^1\mathrm{H}(\vec{\mathrm{d}},\gamma)^3\mathrm{He}$ reactions. The measured data can be compared directly to the observables predicted by theoretical calculations. Although this comparison can reveal differences between theory and experiment, it is desirable to obtain further insight into the origins of these differences. All of the observables can be written in terms of complex Transition Matrix Elements (TMEs) and then the TMEs can be fit to the measured data. Comparing the TMEs calculated from theory with the TMEs obtained by fitting the data yields critical information about the reaction and the three-body system.

6.1 Legendre Polynomial Expansion

Using the angular correlation formalism in [Sey79], the observables can be expanded in terms of the TMEs. The unpolarized cross section, σ_0, can be written in

terms of Legendre polynomials

$$\sigma_0(\theta) = \left(\frac{\lambda\!\!\!^{-2}}{4(2x+1)(2a+1)}\right) \sum_k \mathrm{Q}_k \mathrm{a}_k \mathrm{P}_k(\cos\theta) \tag{6.1}$$

where $\mathrm{Q}_0 \equiv \mathrm{P}_0 = 1$ and

$$\mathrm{A}_0 = \left(\frac{\lambda\!\!\!^{-2}}{4(2x+1)(2a+1)}\right) \mathrm{a}_0. \tag{6.2}$$

These equations are written for the capture reaction a(x,L)c where a is the spin of the target, x is the spin of the projectile, c is the spin of the residual nucleus, and L is the multipolarity of the γ-ray. The value $\lambda\!\!\!^{-}$ is the reduced wave length of the incident beam. The a_k are the normalized Legendre Polynomial coefficients, the $\mathrm{P}_k(\cos\theta)$ are the Legendre polynomials, and the Q_k are the finite geometry attenuation factors. The A_0 coefficient is the absolute cross section normalization constant and contains the correct cross section units. If Equation 6.1 is integrated over all angles the total cross section, σ_T is given by

$$\sigma_T = \int_0^{2\pi} \int_0^{\pi} \sigma(\theta)\ \sin\theta\ \mathrm{d}\theta\ \mathrm{d}\phi = 4\pi \mathrm{A}_0. \tag{6.3}$$

The polarized cross section σ_p can be written in terms of Legendre polynomials with coefficients in front of each polynomial [Sey79]

$$\sigma_p(\theta) = \mathrm{A}_0 \sum_k \Big(\mathrm{a}_k \mathrm{P}_k(\cos\theta) + \mathrm{b}_k \mathrm{P}_k^1(\cos\theta)\mathrm{p}_y + \mathrm{c}_k \mathrm{P}_k(\cos\theta)\mathrm{t}_{20} + \mathrm{d}_k \mathrm{P}_k^1(\cos\theta) Re\left\{\mathrm{t}_{21}\right\} + \mathrm{e}_k \mathrm{P}_k^2(\cos\theta) Re\left\{\mathrm{t}_{22}\right\}\Big). \tag{6.4}$$

The associated Legendre polynomial coefficients a_k, b_k, c_k, d_k and e_k can be related to observables by Equation 4.9. The associated Legendre polynomial coefficients are defined similarly to a_k above. This yields

$$\mathrm{A}_y(\theta)\ \sigma_0(\theta) = \sum_k \mathrm{Q}_k \mathrm{z}_k \mathrm{P}_k^1(\cos\theta) \tag{6.5}$$

$$iT_{11}(\theta)\ \sigma_0(\theta) = \frac{1}{\sqrt{3}} \sum_k Q_k b_k P_k^1(\cos\theta) \tag{6.6}$$

$$T_{20}(\theta)\ \sigma_0(\theta) = \sum_k Q_k c_k P_k(\cos\theta) \tag{6.7}$$

$$T_{21}(\theta)\ \sigma_0(\theta) = \frac{1}{2} \sum_k Q_k d_k P_k^1(\cos\theta) \tag{6.8}$$

$$T_{22}(\theta)\ \sigma_0(\theta) = \frac{1}{2} \sum_k Q_k e_k P_k^2(\cos\theta). \tag{6.9}$$

6.1.1 The Q_k Coefficients

The papers [Ros53, Fer65] contain derivations and discussions of these coefficients. The coefficients are defined by

$$Q_k = \frac{J_k}{J_0}, \tag{6.10}$$

where

$$J_k = \int_0^\pi \epsilon(\beta)\ P_k(\cos\beta)\ d(\cos\beta), \tag{6.11}$$

and where β is the angle of the incident γ-ray beam with respect to the HPGe symmetry axis and $\epsilon(\beta)$ is the probability of γ-ray detection at that angle.

The simplest method for calculating the Q_k coefficients is the method of [Ros53], where $\epsilon(\beta)$ is calculated using the γ-ray linear attenuation coefficients, τ (units = cm^{-1}). From the path length through the HPGe detector at an angle β, $x(\beta)$, one can express $\epsilon(\beta)$ as,

$$\epsilon(\beta) = 1 - e^{-\tau\ x(\beta)}. \tag{6.12}$$

Equation 6.12 gives the total probability that the γ-ray will be detected. This includes the HPGe response function, spreading of the γ-ray energy due to changes in charge collection, as well as loss of events from the full energy peak due to Compton scattering or escape peaks (see Section 3.3). Typically, the interesting quantity is the probability of detecting a full energy event. This is not only dependent on the path length, but also on where the initial interaction takes place in the crystal. This raises the question of how closely Equation 6.12 approximates the full energy detection probability. A Monte Carlo simulation was carried out in [Sch95] and the difference between the result of the simulation and the values calculated from Equation 6.12 was found to be less than 1%. The agreement is due to the fact that the Q_k are calculated as values close to 1 and the differences between Equation 6.12 and more accurate methods is not apparent. Therefore, for purposes of calculating the Q_k for this experiment, Equation 6.12 will be used. The Q_k calculated for this experiment are: $Q_0 = 1.0$, $Q_1 = 0.98$, and $Q_2 = 0.97$.

6.2 Transition Matrix Element Expansion

The Legendre polynomial coefficients presented in the previous section can be expanded in terms of the TMEs of the reaction. The expansion is done according to [Sey79] where the TMEs are written in terms of $R = |R|e^{i\phi}$ where $|R|$ is the TME amplitude and ϕ is the phase. Each matrix element is identified by its continuum quantum numbers in the channel spin coupling scheme. This scheme couples the particle spins in a continuum state vectorially to give the channel spin, s. The channel spin is then combined vectorially with the relative angular momentum, ℓ, to give the total angular momentum for the state, j. Each TME is identified by the j, ℓ, s, and

the mode and multipolarity of the transition, i.e. E1, M1. The expansion of each of the coefficients in terms of the TMEs is given in Appendix A and B.

6.2.1 TMEs for ^{2}H(p,γ)^{3}He and ^{1}H(d,γ)^{3}He

The TMEs present in the ^{2}H(p,γ)^{3}He and ^{1}H(d,γ)^{3}He reactions are restricted by the rules of angular momentum coupling. The proton has $J^\pi = 1/2^+$ and the deuteron has $J^\pi = 1^+$ which can couple to form a variety of continuum states. These states then decay to the ground state of ^{3}He, $J^\pi = 1/2^+$, by emitting a γ-ray.

Given the low incident beam energy in the experiment, E_p = 40-0 keV, one would expect s-wave capture (ℓ=0) to dominate. However, the p-wave terms (ℓ=1) have to be considered because there are no s-wave E1 transitions, and to allow E1 transitions we must allow p-wave capture. The higher angular momentum states, $\ell \geq 2$, are not included because they are expected to be negligible at these energies. In fact, Coulomb penetrability calculations show that from $\ell = 0$ to $\ell = 1$ the barrier penetrability drops by two orders of magnitude and from $\ell = 1$ to $\ell = 2$ it drops three orders of magnitude. This confirms the elimination of terms with $\ell \geq 2$. E1, M1, and E2 radiation are the first terms in the multipole expansion of the electromagnetic field and are the strongest contributors. E2 radiation is suppressed in this case since it requires capture to the D-state, as will be discussed below. The assignment of γ-ray mode (Electric or Magnetic) and multipolarity (L) is done by angular momentum and parity conservation for the reaction. The change in parity from an electric multipole is $(-1)^L$ and for a magnetic multipole it is $(-1)^{L+1}$. The parity of the continuum state, P, is given by $P = \pi_p \pi_d (-1)^\ell$, where π_p and π_d are the intrinsic parities of the proton and deuteron which are both 1 and the $(-1)^\ell$ is the parity from the the orbital angular momentum of the two particles. The continuum quantum numbers for the

^{2}H(p,γ)^{3}He and ^{1}H(d,γ)^{3}He reactions including only s-wave and p-wave transitions are shown in Table 6.1.

s	ℓ	j	Mode and Multipolarity
1/2	1	1/2	E1
1/2	1	3/2	E1,M2
3/2	1	1/2	E1
3/2	1	3/2	E1,M2
1/2	0	1/2	M1
3/2	0	3/2	M1,E2

Table 6.1: The continuum quantum numbers of only s- and p-wave capture TMEs allowed in the ^{1}H(d,γ)^{3}He and ^{2}H(p,γ)^{3}He reactions.

6.2.2 Constraining the Fit

The nine possible TMEs shown in Table 6.1 mean that there are 17 free parameters to fit, nine amplitudes and eight relative phases. Even with the relatively large amount of data collected, it would be difficult to find a unique fit for these parameters. Fortunately, there are some reasonable assumptions that reduce the number of TMEs.

First, we assume that the the ^{3}He ground state is described by a p+d cluster model. In this model, the proton and deuteron move around each other in a relative S- or D-state, the P-state is prohibited by parity conservation. The S-state is lower in energy and is therefore expected to dominate. Typical values of the probability of the D-state in ^{3}He are around 12% [Vet85, Wel88]. The electric multipole operators are expected to be spin independent so we need only consider electric transitions which have $\Delta s = 0$, where Δs is the change in channel spin between the continuum and final states. The S-state of ^{3}He must have channel spin 1/2 to satisfy angular momentum coupling, therefore, we only consider electric matrix elements which have s=1/2 when

considering transitions to the S-state of ^{3}He. The s=3/2 E1 transition to the D-state of ^{3}He is expected to be small due to the small probability of the D-state. The E2 transition is even smaller because it is weaker than the E1 transition so it can be neglected. As further support, full theoretical calculations of this E2 TME show it to be an order of magnitude smaller than the s=3/2 E1 TME, the smallest term of the E1 and M1 terms.

Second, we neglect M2 transitions. Single particle shell model calculations for γ-ray decay transition rates in heavy nuclei, the Weisskopf estimates [Eis85], predict that M2 transitions should be the fourth strongest term in the electromagnetic field expansion after E1, M1, and E2 transitions. Also, for this reaction, M2 transitions only arise in p-wave capture which further reduces their strength. For these reasons it is reasonable to ignore the M2 transitions. Again, the full theoretical calculations show this TME to be two orders of magnitude smaller than the s=3/2 E1 TME.

With the elimination of the M2 and E2 transitions from the above assumptions, we are left with six TMEs which are listed in Table 6.2. This leaves 11 independent parameters to fit to the data.

TME	Multipolarity	s	ℓ	j
$^2p_2$	E1	1/2	1	1/2
$^2p_4$	E1	1/2	1	3/2
$^4p_2$	E1	3/2	1	1/2
$^4p_4$	E1	3/2	1	3/2
$^2s_2$	M1	1/2	0	1/2
$^4s_4$	M1	3/2	0	3/2

Table 6.2: The TMEs used in the analysis of the reaction.

6.2.3 Preforming the TME Fit

A C++ code based on a fitting code described in [Jam71] is used to do a χ^2 minimization of the TMEs to the measured data. The code uses the ROOT data analysis system which is a new version of the CERN library written in C++. To control the minimization, the code uses the MINUIT fitting routines from the CERN library. The analysis program varies the amplitudes and phases for the TMEs and does a χ^2 minimization of the measured data. The χ^2 function is given by

$$\chi^2 = \sum_{o,\theta} \left(\frac{\mathrm{V}_o(\theta) - \mathrm{C}_o(\theta)}{\mathrm{E}_o(\theta)} \right)^2 \tag{6.13}$$

where the sum is over the observables and the values of θ where the observable was measured. The quantity $\mathrm{V}_o(\theta)$ is the observable measured at that θ, $\mathrm{C}_o(\theta)$ is the value of the observable at θ calculated from the TMEs, and $\mathrm{E}_o(\theta)$ is the error on the observable measured at θ.

6.3 Three-Body Theory Results

The Pisa group [Viv96] did three-body calculations of the $^2\mathrm{H}(\vec{\mathrm{p}},\gamma)^3\mathrm{He}$ reaction at E_p = 10, 25, 35, 45, 60, and 80 keV. To compare the theory to the data that we collected at E_p = 40 - 0 keV the theory data had to be energy averaged from 10 to 45 keV. This was done by weighting the calculated values by the stopping power. The formula used was

$$\mathrm{R}_{avg} = \frac{\sum_{E=0}^{n} (\mathrm{R}_E + \mathrm{R}_{E+1})(\Delta E)(\mathrm{STP}_{E+1} - \mathrm{STP}_E)}{(\mathrm{E}_n - \mathrm{E}_0)(\mathrm{STP}_{E_n} - \mathrm{STP}_{E_0})} \tag{6.14}$$

where R is the value to be energy averaged, ΔE is the energy difference between the two values, and STP_E is the stopping power at that energy. The changes in stopping

power are given in Table 6.3

ΔE_p(keV)	Δ STP
10 – 25	1.83
25 – 35	0.975
35 – 45	0.889
45 – 60	1.251
60 – 80	1.608

Table 6.3: The stopping power differences used to weight the theory calculations.

The calculations were done in a different formalism from the one used in [Sey79]. The calculated amplitudes include a factor of $\sqrt{2j+1}$ and the calculated phase of the $^2p_2$ and $^2p_4$ is rotated by 180°. The calculated phase of the $^2s_2$ is rotated by 90° and the $^4s_4$ by $-90°$. All of the calculated results will be transformed to the formalism of [Sey79] so that the equations in Appendix A and B are valid.

6.3.1 Full Calculation

The full calculation done by the Pisa group [Viv96] uses both the AV18 NN Potential and the Urbana IX three body interactions as described in Section 2.3. They also calculated the one E2 and and two M2 TMEs listed in Table 6.1. The calculated theoretical observables plotted in Figure 6.1 contain these E2 and M2 terms. For comparison the theoretically calculated values without these terms are shown in Figure 6.1. There are slight differences in σ, iT_{11}, T_{22}, and P_γ. The differences in T_{22} are most noticeable because allowing E2 and M2 radiation allows for e_3 and e_4 coefficients as well as the e_2 coefficient. With these coefficients non-zero, the observable is no longer symmetric around 90°. One will note that the calculated A_y is lower than the measured values and that the calculated iT_{11} is larger than the

measured values. This is called the "A_y Puzzle" and is discussed in Section 1.5.2. The total χ^2 is quite large, as seen in Table 6.4, with over half of the χ^2 coming from T_{22}. Table 6.5 contains the calculated TMEs and cross section fractions. Finally, the

Observable	χ^2
σ	29.684093
A_y	44.762837
iT_{11}	17.684732
T_{20}	157.116936
T_{21}	3.759770
T_{22}	0.989690
P_γ	0.922068
A_γ	0.076859
Total	254.996985

Table 6.4: The χ^2 for each observable for the calculated observables.

TME	Amplitude	Fraction	Phase
$^2p_2$	0.3142	0.189674	25.274
$^2p_4$	0.3417	0.448658	25.302
$^4p_2$	0.05655	0.006144	205.32
$^4p_4$	0.03022	0.003509	25.514
$^2s_2$	0.3524	0.238599	163.18
$^4s_4$	0.1718	0.113415	163.22

Table 6.5: The TMEs calculated from the full theory.

values of the Legendre coefficients are given in Table 6.6.

6.3.2 Impulse Approximation Calculation

The Pisa group [Viv96] calculated the TMEs for $^2H(\vec{p},\gamma)^3He$ reaction using the AV18 NN potential without any two-body currents, the Impulse approximation. The

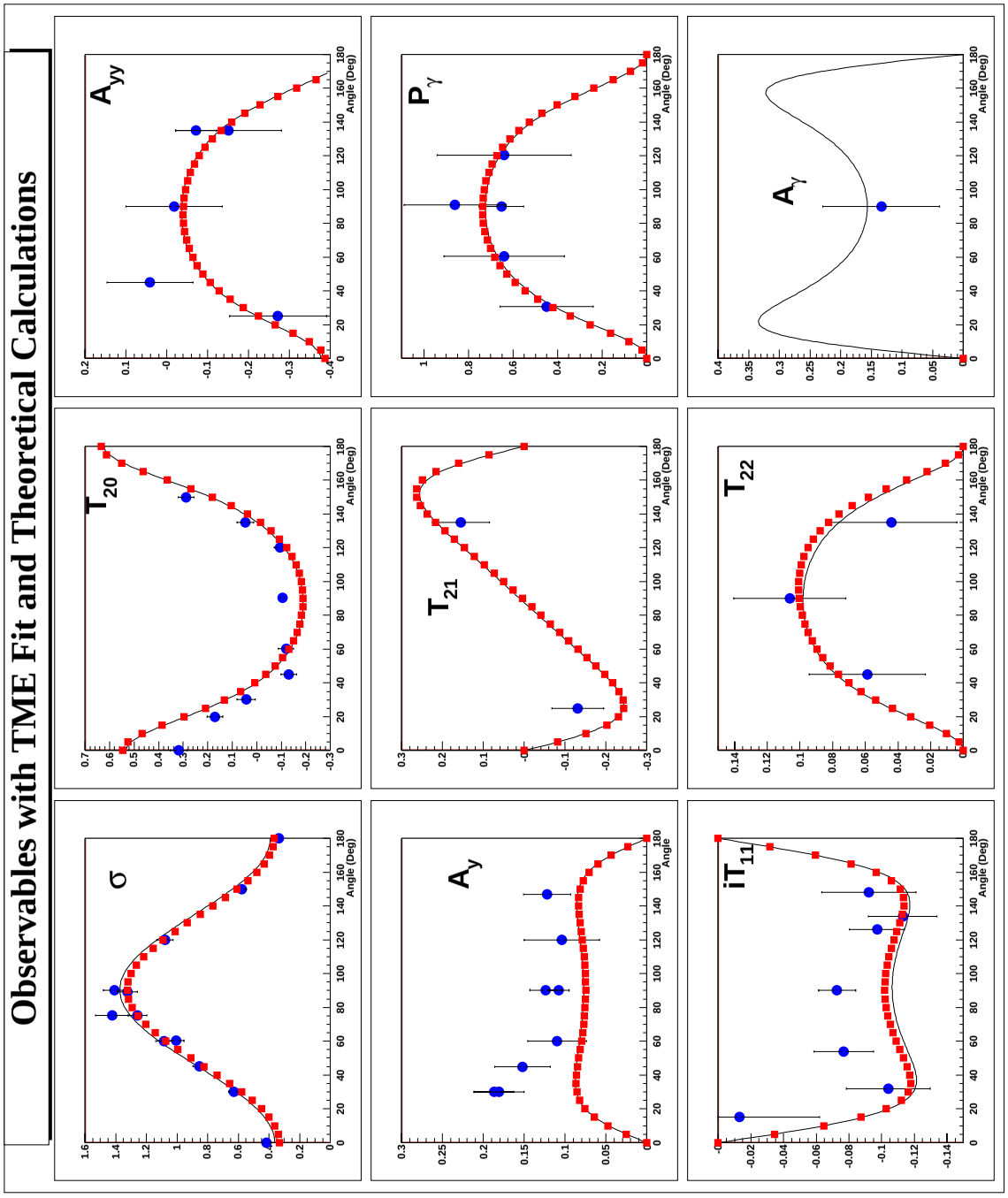

Figure 6.1: The full theoretically calculated observables. The squares are the theoretical predictions for each observable with E2 and M2 terms included. The solid line is the theoretical observable without the E2 and M2 terms. The circles with error bars are the measured data and the error bars are statistical in nature.

Observable	Coefficient	Value
σ	A_0	1.0410
	a_1	-0.014066
	a_2	-0.63755
iT_{11}	b_1	-0.24313
	b_2	-0.00018066
T_{20}	c_0	-0.095731
	c_1	-0.024172
	c_2	0.30562
T_{21}	d_1	0.029613
	d_2	-0.23027
T_{22}	e_2	0.086266
A_y	z_1	0.10199
	z_2	-0.00013670
P_γ	f_2	-0.061738
	g_1	0.21858
	g_2	-3.4072e-05
	h_1	-0.49610
	h_2	8.7907e-05

Table 6.6: The resulting Legendre polynomial coefficients from the full theoretical calculations.

calculated values had to be both energy and stopping power averaged to compare to our data. The values calculated this way are not a good approximation of the reaction as shown by Figure 6.2. None of the observables are well represented using this calculation and the χ^2 is 140 times greater than for the full calculation (see Table 6.7). This is almost completely due to the cross section which the Impulse Approximation underpredicts. The biggest change in the calculated TMEs is that $^4p_2$ phase has changed by 180° and $^4p_4$ has a large reduction in amplitude and a change in phase. The amplitudes of all the TMEs have changed (see Table 6.8). The E1 s=3/2 cross section fractions have dropped substantially. The ratio of the cross section fractions for the M1 terms has changed from 0.48 to 1.92. This will be discussed in further detail in Section 6.6. This leads to large changes in all of the

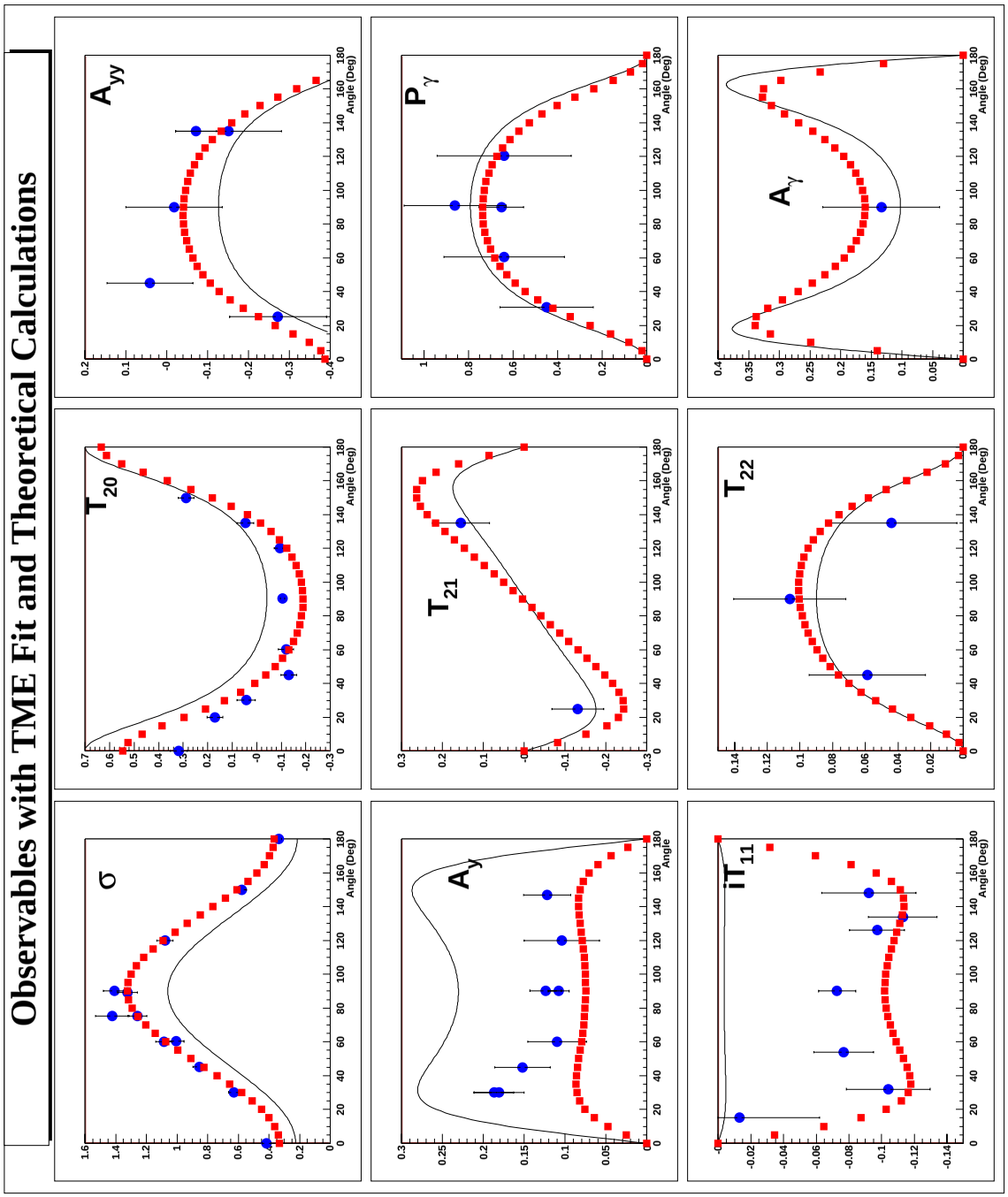

Figure 6.2: The theoretically calculated observables using the Impulse Approximation. The squares are the full theoretical predictions for each observable with E2 and M2 terms included. The solid line is the theoretical Impulse approximation calculations without the E2 and M2 terms. The circles with error bars are the measured data where the error bars are statistical in nature.

Legendre coefficients (see Table 6.9).

Observable	χ^2
σ	300.335696
A_y	214.233500
iT_{11}	134.620247
T_{20}	340.358032
T_{21}	0.605755
T_{22}	1.005061
P_γ	2.337896
A_γ	0.109855
Total	993.606042

Table 6.7: The χ^2 for each observable from the Impulse Approximation calculation.

TME	Amplitude	Fraction	Phase
$^2p_2$	0.3027	0.234761	25.262
$^2p_4$	0.3068	0.482328	25.292
$^4p_2$	0.01897	0.000922	25.611
$^4p_4$	0.0001308	0.0	59.546
$^2s_2$	0.1934	0.095833	163.32
$^4s_4$	0.1906	0.186156	163.22

Table 6.8: The TMEs calculated from the Impulse Approximation.

6.4 TME Analysis Results

The six TMEs from Table 6.2 were fit to the full data set. The $^2p_2$ phase was held to the same value as the theoretical predication because one phase is arbitrary. The fit was started at the theoretical values for each of the TMEs' amplitudes and phases with the final values shown in Table 6.11. The total χ^2/ν (chi-square per degree of freedom) for the fit was found to be 1.03. There were 47 data points and 11 free

Observable	Coefficient	Value
σ	A_0	0.78060
	a_1	0.0068264
	a_2	-0.71704
iT_{11}	b_1	-0.0084658
	b_2	-0.00021775
T_{20}	c_0	0.028665
	c_1	0.0050855
	c_2	0.16963
T_{21}	d_1	-0.0062298
	d_2	-0.14459
T_{22}	e_2	0.081393
A_y	z_1	0.31322
	z_2	-0.00016692
P_γ	f_2	-0.069434
	g_1	0.23952
	g_2	-3.9431e-05
	h_1	-0.61203
	h_2	0.00010180

Table 6.9: The resulting Legendre polynomial coefficients from the Impulse Approximation calculation.

parameters resulting in 36 degrees of freedom. The χ^2 for each observable is listed in Table 6.10. One will notice that half of the χ^2 results from $T_{20}(\theta)$ which one can see in Figure 6.3 where two data points do not intersect the fit at all. The TMEs from the fit are in Table 6.11 and the cross section fractions for each TME are also listed. And the Legendre polynomial coefficients calculated from the fitted TMEs are given in Table 6.12. A graph of each observable and the TME fit to the data is shown in Figure 6.3.

In Figure 6.3 the theoretical calculations are also shown to allow comparison between theory and the TME fit to the data. One can see that there are substantial differences in $A_y(\theta)$ and $iT_{11}(\theta)$ which shows that the $A_y(\theta)$ puzzle exists for this capture reaction. The other major difference is between the $T_{22}(\theta)$ fit and the theo-

retical calculations which shows little asymmetry around 90°. Looking at Table 6.11 and Table 6.5 the main changes are to the E1 s=1/2 amplitudes and the E1 s=3/2 phases. The main changes in the cross section fraction from the fit in to the theory are to $^2p_2$ and $^2p_4$.

Observable	χ^2
σ	8.387644
A_y	3.815820
iT_{11}	2.866483
T_{20}	18.332832
T_{21}	0.302989
T_{22}	0.789464
P_γ	0.986593
A_γ	1.609170
Total	37.090995

Table 6.10: The χ^2 for each observable in the full fit to the data.

TME	Amplitude	Fraction	Phase
$^2p_2$	0.3545 ± 0.02687	0.250423 ± 0.037960	25.274 ± 0
$^2p_4$	0.3159 ± 0.01282	0.397578 ± 0.032265	27.019 ± 3.9713
$^4p_2$	0.06815 ± 0.02609	0.009252 ± 0.007084	164.56 ± 41.303
$^4p_4$	0.04722 ± 0.01839	0.008883 ± 0.006920	251.36 ± 36.444
$^2s_2$	0.3485 ± 0.0245	0.241951 ± 0.034016	163.88 ± 9.3792
$^4s_4$	0.1519 ± 0.01475	0.091914 ± 0.017853	158.02 ± 20.943

Table 6.11: The TMEs resulting from a fit to the full data set. The fraction of the cross section strength for each TME is also given.

6.5 Watson's Theorem and the $A_y(\theta)$ Puzzle

Watson's Theorem, as described in Section 1.5.1, was applied to the data analysis in an effort to improve the fit to the data and reduce the errors on the TMEs. This

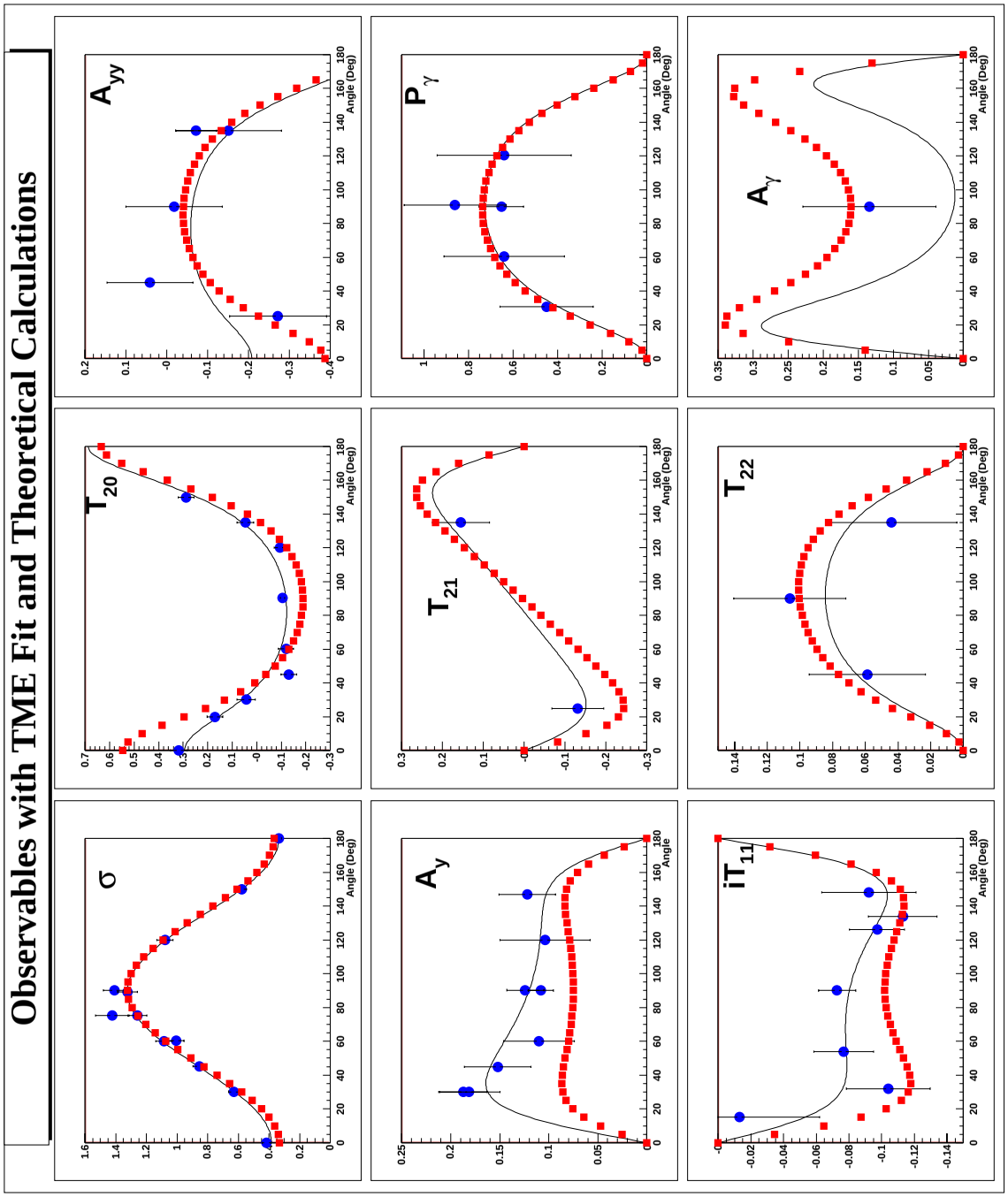

Figure 6.3: The full TME fit to the data. The squares are the theoretical predictions for each observable. The circles with error bars are the measured data where the error bars are statistical in nature. The solid line is the TME fit for each observable.

Observable	Coefficient	Value
σ	A_0	1.0039 ± 0.063935
	a_1	0.024001 ± 0.10073
	a_2	-0.64104 ± 0.058601
iT_{11}	b_1	-0.18351 ± 0.10813
	b_2	0.0086570 ± 0.022259
T_{20}	c_0	-0.047598 ± 0.057473
	c_1	-0.058652 ± 0.075316
	c_2	0.21900 ± 0.056392
T_{21}	d_1	0.071837 ± 0.092248
	d_2	-0.17127 ± 0.037734
T_{22}	e_2	0.074329 ± 0.020927
A_y	z_1	0.15873 ± 0.098516
	z_2	0.016314 ± 0.021964
P_γ	f_2	-0.062070 ± 0.0056729
	g_1	0.18750 ± 0.041330
	g_2	0.010536 ± 0.010428
	h_1	-0.64145 ± 0.12682
	h_2	-0.027176 ± 0.026923

Table 6.12: The resulting Legendre polynomial coefficients from the full fit to the data.

theorem relates the phases determined by a phase shift analysis of scattering data to the phases for radiative capture. Because there is no scattering data at these energies the theoretically calculated phases were used to constrain the capture phases. As one can see from Table 6.13, the theoretical nuclear phase shifts are extremely small at the energies of our experiment. Even if the phase shifts are off by large amounts our experiment would not be sensitive to them since we have errors on the order of a few degrees.

Constraining the TMEs, fit to the data, to have their E1 and M1 phases be within 1° of the theoretically calculated phases results in a χ^2/ν of 1.659. The main problem with this fit is that it is nearly symmetric around 90° for $A_y(\theta)$ and $iT_{11}(\theta)$ which is not true of the data set. It also changes the doublet to quartet M1 cross section ratio

TME	Nuclear Phase (deg)
$^2p_2$	-0.004
$^2p_4$	-0.004
$^4p_2$	0.009
$^4p_4$	0.010
$^2s_2$	-0.008
$^4s_4$	-0.52

Table 6.13: The calculated theoretical nuclear phase shifts for the $^2H(p,\gamma)^3He$ and $^1H(d,\gamma)^3He$ reactions.

to 0.666 which is quite distant from the theoretical values. Allowing the E1 s=3/2 phases to vary while keeping all other phases within 1° of the theory values gives a χ^2/ν of 1.035 and the M1 ratio is 0.428. Unfortunately, the phases of the E1 s=3/2 terms are now 130° from the other E1 phases and are 95° from each other.

An investigate of the behavior of the E1 s=3/2 phases was undertaken because the paper discussed in Section 1.5.2 [Hüb98] blames the s=3/2, ℓ=1 phases for the $A_y(\theta)$ puzzle in elastic scattering. Therefore, we examined the s=3/2 TMEs in the capture reaction for the same effects. In a fit to the data, the only parameters allowed to vary from the theoretical values were the E1 s=3/2 phases. This yielded a χ^2/ν = 2.600 and brings the experimental $A_y(\theta)$ and $iT_{11}(\theta)$ data at 90° into agreement with the data. The asymmetry of the data around 90° was not reproduced, but the overall difference between theory and experiment was much reduced. The s=3/2, j=1/2 E1 phase rotated by -47° and the s=3/2, j=3/2 E1 phase rotated by -99°. The main problem with this fit to the data is that $T_{20}(\theta)$ asymmetry around 90° is not reproduced. It seems that in the case of the capture reaction $^2H(\vec{p},\gamma)^3He$ and $^1H(\vec{d},\gamma)^3He$, the $A_y(\theta)$ puzzle is caused by the E1 s=3/2 phases. These values do not seem to be calculated properly by the current theory. Hopefully work will be underway to fix these values.

More TMEs were allowed to vary in an attempt to get a good description of the $T_{20}(\theta)$ data. Allowing the s=3/2 E1 TME amplitudes and phases to vary only changes $\chi^2/\nu = 2.513$ and $T_{20}(\theta)$ is still not well reproduced. Allowing all E1 amplitudes to vary and the E1 s=3/2 phases to vary yields $\chi^2/\nu = 1.246$ and now all observables are reproduced nearly as well as with the free fit. The effect of the M1 amplitudes on the fit was examined by allowing all amplitudes to vary. All the phases were held within 1° of theory, except the E1 s=3/2 which could vary anywhere. The fit of the data with these constraints yielded $\chi^2/\nu = 1.035$. The fit is almost as good as the free fit with the bonus that the errors on the TMEs are reduced from those on the free fit.

Finally, allowing all amplitudes and the E1 s=3/2 phases to vary while holding the other four phases fixed to theoretical values yields $\chi^2/\nu = 0.968$ and reproduces the data very well. The assumption that the phases of the E1 s=1/2 and M1 TMEs are well determined by theory is upheld by the small reduction in χ^2 for the current fit of 37.759 to the unconstrained fit of 37.091 (this is given as χ^2 because the degrees of freedom change for the two fits). The phases for the capture TMEs were calculated from the theoretical scattering phases. These phases, except for the s=3/2 E1 phases, seem to be well described and are in good agreement with scattering experiments at higher energies. In light of this, this fit will be used for calculating the quantities of interest. The tables containing the calculated values for this fit are given in Table 6.14, Table 6.15, and Table 6.16.

Observable	χ^2
σ	8.683287
A_y	3.856369
iT_{11}	3.167061
T_{20}	17.960440
T_{21}	0.398044
T_{22}	0.830874
P_γ	1.002430
A_γ	1.860617
Total	37.759122

Table 6.14: The χ^2 for each observable for the phase constrained final fit to the data.

TME	Amplitude	Fraction	Phase	Theory
$^2p_2$	0.375 ± 0.0147	0.279829 ± 0.021947	25.274 ± 0	25.274
$^2p_4$	0.3075 ± 0.009486	0.376424 ± 0.023222	25.302 ± 0	25.302
$^4p_2$	0.07847 ± 0.009174	0.012254 ± 0.002865	154.34 ± 8.5649	205.32
$^4p_4$	0.05068 ± 0.007268	0.010225 ± 0.002933	246.88 ± 11.543	25.514
$^2s_2$	0.3291 ± 0.0107	0.215504 ± 0.014017	163.18 ± 0	163.18
$^4s_4$	0.163 ± 0.006568	0.105763 ± 0.008523	163.22 ± 0	163.22

Table 6.15: The TMEs determined by the phase constrained final fit to the data.

6.6 Doublet to Quartet Strength (MEC)

The inclusion of Meson Exchange Currents (MEC) changes the theoretical value of the ratio of the Doublet to Quartet M1 cross section strength substantially (see Section 1.5.3). The treatment of the MEC in the theoretical calculations are important. Friar's [Fri91] calculations at zero energy using AV14 gave a ratio of 0.58. The AV18/IX "full" calculation in [Viv96] gives a ratio of 0.512 at zero energy. The AV14/VIII calculation, which has a stronger tensor force than AV18, gives a ratio of 0.456. Neither result from [Viv96] agrees with [Fri91] because of the use of different NN potentials and three-body currents.

Observable	Coefficient	Value
σ	A_0	1.0049 $\pm$ 0.036328
	a_1	0.022002 $\pm$ 0.027622
	a_2	-0.64333 $\pm$ 0.034762
iT_{11}	b_1	-0.18435 $\pm$ 0.023972
	b_2	0.012989 $\pm$ 0.0053473
T_{20}	c_0	-0.047331 $\pm$ 0.017986
	c_1	-0.060286 $\pm$ 0.018431
	c_2	0.22004 $\pm$ 0.018510
T_{21}	d_1	0.073838 $\pm$ 0.022574
	d_2	-0.17481 $\pm$ 0.013134
T_{22}	e_2	0.080146 $\pm$ 0.0080407
A_y	z_1	0.15933 $\pm$ 0.018575
	z_2	0.014933 $\pm$ 0.0071193
P_γ	f_2	-0.062289 $\pm$ 0.0033653
	g_1	0.17826 $\pm$ 0.0094737
	g_2	0.0079213 $\pm$ 0.0033800
	h_1	-0.62255 $\pm$ 0.031285
	h_2	-0.020420 $\pm$ 0.0087253

Table 6.16: The resulting Legendre polynomial coefficients from the constrained and final fit to the data.

The full theoretical calculation, at the energies of the current experiment, includes MEC and uses AV18/IX which gives a ratio of 0.478 while the Impulse Approximation calculation, which excludes two-body currents including MEC, shows a ratio of 1.94. The newest value determined from experiment using the constrained fit as described in the section before is 0.49 $\pm$ 0.05. Our ratio yields a value of 15.8 $\pm$ 1.0 nb for the s=1/2 M1 capture cross section and 7.75 $\pm$ 0.62 nb for the s=3/2 M1 capture. This is in comparison to the full three body calculation of 15.8 nb and 7.5 nb, respectively. The remarkable agreement observed here is tribute to the quality of the state-of-the-art three-body theory.

6.7 Asymptotic D- to S-State Ratio

As was shown in Section 1.5.4, the asymptotic D- to S-state ratio, η, is sensitive to T_{20} and to the tensor force. In order to determine the value of η experimentally one needs to measure $T_{20}(90^\circ)$.

The value measured was $T_{20}(90^\circ) = -0.1051 \pm 0.0108$ [Ric97a]. The value of η was determined by varying η until it predicted the correct value of T_{20}. The radiative capture program DIRAC generates the TMEs which are used to calculate the value of T_{20} using the TME expansion in Section A.3. The electric transitions can be calculated using Siegert's theorem, but calculations of the magnetic transitions require explicit MEC (two-body currents) effects. Therefore, DIRAC only calculates the electric transitions. The M1 TMEs account for about 30% of the cross section strength at these energies [Sch97]. Therefore, the value of $T_{20}(90^\circ)$ was calculated with the M1 contribution removed. This was done by obtaining the TMEs from a fit to the observables. In the case of [Ric97a] the fit to the cross section, $A_y(\theta)$, $P_\gamma(\theta)$, and $T_{20}(\theta)$ yielded TMEs that gave a value of $T_{20}(90^\circ)$ that was too negative. In order to correct for that, the M1 removed value of $T_{20}(90^\circ)$ was found by the following method. $T_{20}(90^\circ)$ was calculated from the TME fit to the data. Then the ratio of this number and the number calculated with the M1 terms set to zero was taken. This ratio was then multiplied by the experimentally measured value of $T_{20}(90^\circ)$. The M1 removed value from this method was found to be $T_{20}(90^\circ) = -0.0742 \pm 0.0176$ [Ric97a]. In the current experiment, the TME fit predicted the value of $T_{20}(90^\circ)$ accurately. So the M1 removed value was calculated simply by setting the M1 TME's amplitudes to zero and calculating $T_{20}(90^\circ)$. This yielded a M1 removed value of $T_{20}(90^\circ) = -0.0654 \pm 0.0165$.

The TME for E1 radiation takes the form of $\langle u|\theta|\psi\rangle$. To determine the TMEs one needs to determine the bound state wave function, u, the operator, θ, which is just er for E1 radiation, and the scattering wavefunction, ψ. The bound state wave function, u, used was the purely asymptotic Whittaker function. The value of C_S^C was set to match experimental values from [Wel88] so that $(C_S^C)^2 = 3.24$. Then C_D^C was set according to the value of η. The Whittaker function diverges at p-d separation distance of zero. So a cutoff of r_{cut} was set at a few fermis. At high energies [Vet85] this cutoff was found to change the value of η, but at low energies [Ric97a] the cutoff had an order of magnitude smaller effect on the value of η. The final state wavefunction, ψ, consisted of the Whittaker function beyond 3 fm and an optical model potential for the wave function from [Gib84] for the innermost 3 fm. The values for the optical model potential were taken from Guss [Kin83] except that the imaginary surface terms were neglected. The value of η was then varied until the M1 removed value of $T_{20}(90^\circ)$ was obtained. This yielded for Rice *et al.* [Ric97a] a value of $\eta = -0.0399 \pm 0.0091$. For the current experiment the value was $\eta = -0.0340 \pm .0102$ which is the same within error. The error in the new number is mostly due to the large error in the E1 s=3/2 phases.

To check the model dependence of the determination of η the Whittaker function and the realistic wavefunction were matched differently. Two extra calculations were done with the realistic wavefunction multiplied by 2/3 and 3/2 (see Figure 6.4. For the data of Rice *et al.* [Ric97a], this yielded values of $\eta = -0.0387 \pm 0.0087$ for the 3/2 case and $\eta = -0.0418 \pm 0.0096$ for the 2/3 case. Thus, the model dependence was found to be small and the final value was $\eta = -0.0399 \pm 0.0091^{+0.0012}_{-0.0019}$. Using the same method for the current experiment gives $\eta = -0.0340 \pm .0102^{+0.010}_{-0.015}$. This compares well with the distorted-wave Born approximation extraction of $\eta = -0.0386 \pm 0.0046 \pm 0.0012$

from [Aye95]. Friar *et al.* [Fri88] also calculated $\eta = -0.0430 \pm 0.001$ using a full three-body Faddeev calculation.

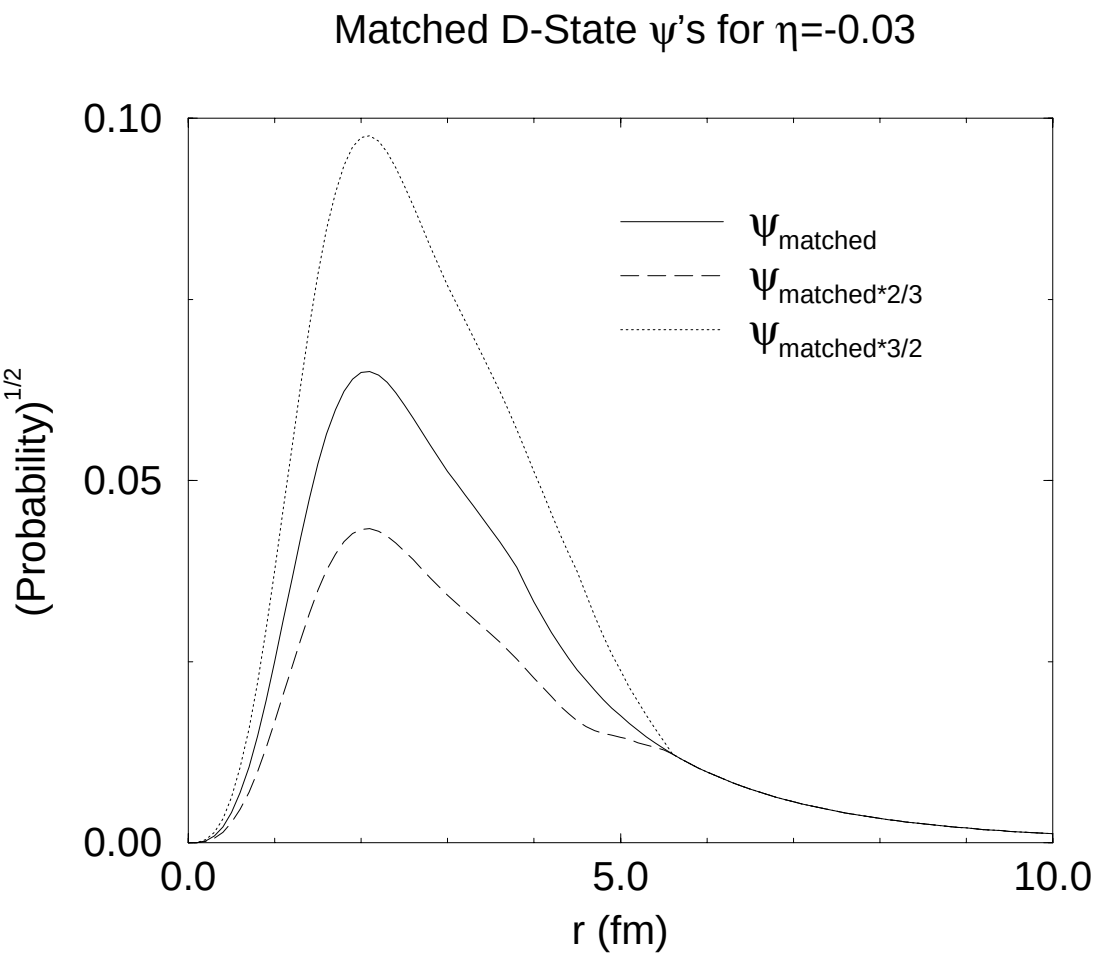

Figure 6.4: The matched realistic and Whittaker function wavefunctions for the D-state with the realistic section multiplied by factors of 2/3, 1, and 3/2.

6.8 Gerasimov-Drell-Hearn Sum Rule

From the TME fit to the gathered data, part of the Gerasimov-Drell-Hearn (GDH) Sum Rule (see Section 1.5.5) can be calculated for the $^3\vec{\mathrm{H}}\mathrm{e}(\vec{\gamma},\mathrm{d})\mathrm{H}$ reaction.

The integral for the GDH sum rule is repeated here

$$\mathrm{I}_{GDH} = \int_{\mathrm{E}_{th}}^{\infty} \frac{\sigma_{\rightrightarrows}(k) - \sigma_{\rightleftarrows}(k)}{k} \mathrm{d}k = 4\pi\alpha S \left(\frac{\kappa\hbar c}{Mc^2}\right)^2, \tag{6.15}$$

where the different quantities are explained in Section 1.5.5. From the article [Wel94] the difference between the photodisintegration cross sections for a polarized γ-ray beam and ^{3}He target can be written in terms of the TMEs for the reaction. The difference in cross sections is given by

$$\sigma_{\rightrightarrows}(k) - \sigma_{\rightleftarrows}(k) = \lambda\!\!\!^{-2}_{\gamma} f_c f \left[-\left|{}^2\mathrm{p}_2\right|^2 + \left|{}^2\mathrm{p}_4\right|^2 - \left|{}^4\mathrm{p}_2\right|^2 + \left|{}^4\mathrm{p}_4\right|^2 - \left|{}^2\mathrm{s}_2\right|^2 + \left|{}^4\mathrm{s}_4\right|^2 \right] \tag{6.16}$$

where $\lambda\!\!\!^{-}_{\gamma}$ is the wavelength of the incident γ-ray beam, and f and f_c are the fractional polarization of the target and γ-ray beam respectively. For the calculations, the polarizations are set to 1 in order to make it easier to compare to theory.

The first step is take the S-factor data and M1 fraction data from [Sch97]. This allows us to calculate the S-factor separately for the E1 and M1 terms (see Figure 6.5) which allows us to calculate σ_{E1} and σ_{M1} as a function of energy using Equation 4.5. A linear fit to the M1 and E1 S-factors yields

$$\mathrm{S}_{E1}(\mathrm{E}_{lab}) = 0.0859 + 0.00445\ \mathrm{E}_{lab} \tag{6.17}$$

$$\mathrm{S}_{M1}(\mathrm{E}_{lab}) = 0.107 - 0.000405\ \mathrm{E}_{lab} \tag{6.18}$$

where E_{lab} is in keV and the S-factors are in eV·b. The astrophysical S-factor at zero energy calculated by [Viv96] for s- and p-waves is $\mathrm{S}_S = 0.105$ eV·b and $\mathrm{S}_P = 0.0865$ eV·b. This is in excellent agreement with our extrapolation.

Next, we make an assumption about the cross section fractions. We have determined the cross section fractions from E_p(lab) = 40-0 keV. The cross section drops rapidly so that most of the contribution to this calculation is from 30-40 keV. Therefore, we assume that the cross section fractions for the E1 terms, with respect to

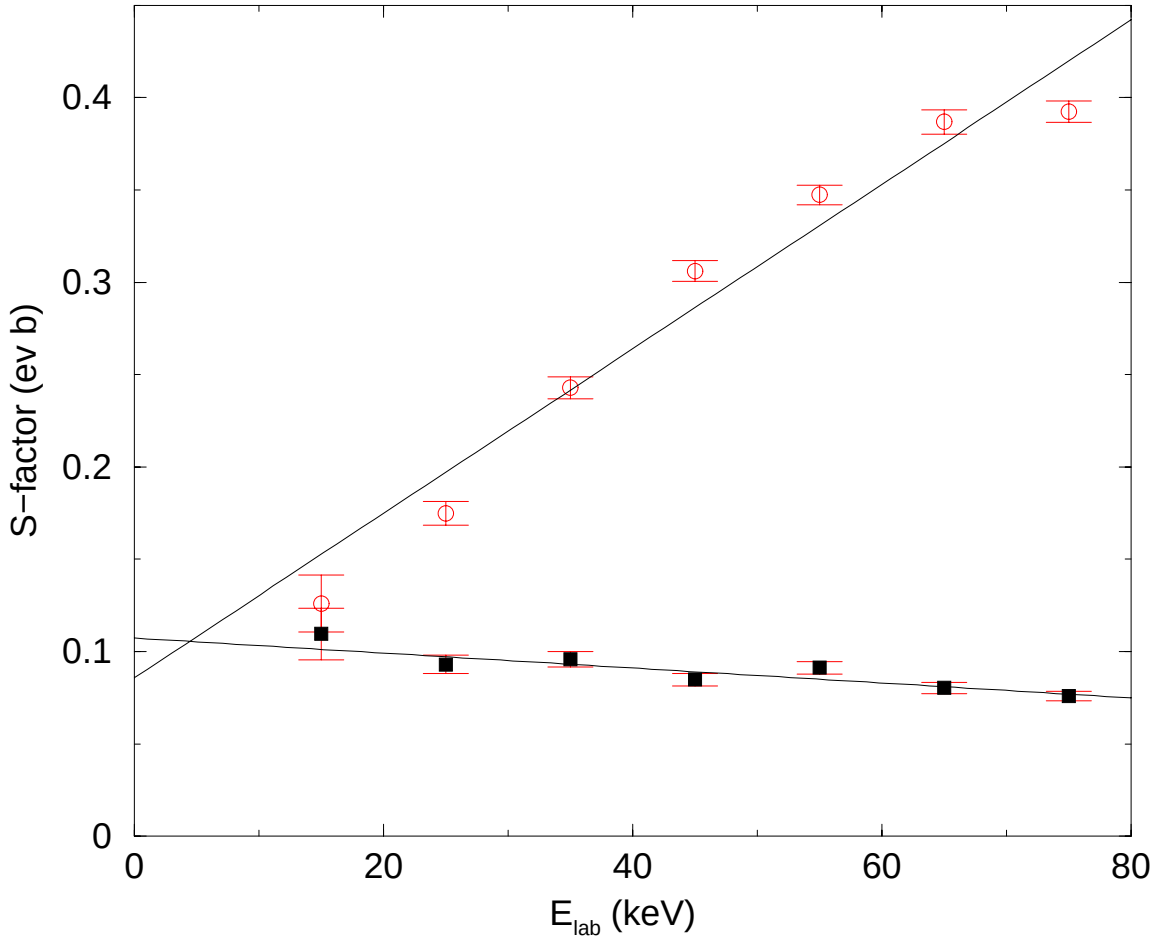

Figure 6.5: The astrophysical S-factors for the ^{2}H(p,γ)^{3}He reaction. The open circles are the E1 S-factors and the closed squares are the M1 S-factors. A χ^2 linear fit is shown for each set of S-factors.

each other, and the M1 terms, with respect to each other, stay constant. This means that the ratio of the two M1 terms, $\frac{\sigma_{M1}(s=3/2)}{\sigma_{M1}(s=1/2)}$, stays at about 0.5, but the total M1 cross section will vary with energy according to σ_{M1} determined above. This has been shown to be true for the M1 terms in [Viv96]. The same general idea is carried out with the E1 terms except now the ratio that is kept constant is given by

$$\mathrm{R}_{E1} = \frac{\sigma^i_{E1}}{\sum_j \sigma^j_{E1}} \tag{6.19}$$

and the total E1 cross section is determined as a function of energy by σ_{E1}.

We need the amplitudes of the TMEs for the $^3\vec{\mathrm{H}}\mathrm{e}(\vec{\gamma},\mathrm{d})\mathrm{H}$ reaction, but we have determined the TMEs of the $^1\mathrm{H}(\mathrm{d},\gamma)^3\mathrm{He}$ or $^2\mathrm{H}(\mathrm{p},\gamma)^3\mathrm{He}$ reaction. The TME amplitudes for the different reactions can be related by the principle of detailed balance as described in [Hay70]. The cross section for photodisintegration can be related to the capture reaction B(X,γ)A by

$$\sigma(\gamma,p)\ \lambda\!\!\!^{-2}_{\gamma}\ 2(2\mathrm{S}_A+1) = \lambda\!\!\!^{-2}_{p}\ (2\mathrm{S}_X+1)\ (2\mathrm{S}_B+1)\ \sigma(p,\gamma) \tag{6.20}$$

where S_A is the spin of A, S_X is the spin of X, S_B is the spin of B. The value of $\lambda\!\!\!^{-}_{\gamma}$ is given by

$$\lambda\!\!\!^{-}_{\gamma} = \frac{\hbar c}{\mathrm{E}_{c.m.}+Q} \tag{6.21}$$

where Q is the photodisintegration threshold energy. The value of $\lambda\!\!\!^{-}_{p}$ is given by

$$\lambda\!\!\!^{-}_{p} = \frac{\hbar c}{\mu\sqrt{2\mathrm{M}_B\mathrm{E}_p}} \tag{6.22}$$

where μ is the reduced mass $\frac{\mathrm{M}_X}{\mathrm{M}_A}$. This yields

$$\sigma(\gamma,p) = \frac{(2\mathrm{S}_X+1)(2\mathrm{S}_B+1)}{2(2\mathrm{S}_A+1)}\mu\left(2\mathrm{M}_B c^2\right)\frac{\mu\mathrm{E}_{lab}}{\left(\mu\mathrm{E}_{lab}+Q\right)^2}\sigma(p,\gamma) \tag{6.23}$$

which for the $^3\vec{\mathrm{H}}\mathrm{e}(\vec{\gamma},\mathrm{d})\mathrm{H}$ reaction reduces to

$$\sigma(\gamma,p) = 1879.74\times10^3\frac{0.6678\mathrm{E}_{lab}}{\left(0.6678\mathrm{E}_{lab}+5494\right)^2}\sigma(p,\gamma) \tag{6.24}$$

for E_{lab} in keV.

We can now calculate the integral as a function of energy numerically and obtain the GDH sum rule. The results are summarized in Table 6.17. One can see that the impulse approximation shows that the GDH sum rule at these energies should be almost 0. This is not so surprising since this approximation assumes no internal structure. The full calculation using AV18/IX agrees within errors with the fit to the

Component	Fit	AV18/IX	IA
E1 s=1/2	-0.0345 ± 0.0095	0.0095	0.0016
E1 s=3/2	-0.0027 ± 0.0008	-0.0012	-0.00023
M1	-0.0533 ± 0.0077	-0.0585	-0.00066
Total	-0.0906 ± 0.0123	-0.050	0.00073
Total(0-80)	-1.105 ± 0.219	-0.459	0.0155

Table 6.17: The GDH sum rule calculated from our fit to the data as well as for the full calculation using AV18/IX and the impulse approximation (IA). All the numbers are integrated from $E_p = 0$ to 40 keV and are in nb. The calculations are split up for each of the different E1 terms with different s and for the M1 terms. The same calculation was also done for $E_p = 0$ to 80 keV.

data for the E1 s=3/2 and M1 terms. The E1 s=1/2 terms for the full calculation and the fit differ substantially and this difference accounts for the difference in the total calculated sum rule. The theorists [Viv96] are calculating the GDH sum rule exactly and this will be included when it becomes available.

The fit to the data is for an energy average of about 35 keV. The assumption that the cross section fractions for the E1 terms and the M1 terms are constant with respect to each other over our energy region can be checked at the lower energies. Changing the E1 s=1/2 terms' cross section fractions by 20% and the M1 terms' cross section fractions by 20% and integrating from 0 to 20 keV yields a difference of only 0.002 nb which is only a 6.2% difference.

Chapter 7

Conclusions

This experiment succeeded in obtaining the most complete data set to date for the ^{2}H($\vec{\mathrm{p}},\gamma$)^{3}He and ^{1}H($\vec{\mathrm{d}},\gamma$)^{3}He reactions at E$_p$(lab) = 40-0 keV. The observables measured were the differential cross section $\sigma(\theta)$, the vector analyzing power A$_y(\theta)$ and the related factor iT$_{11}(\theta)$, the tensor analyzing powers T$_{20}(\theta)$, T$_{21}(\theta)$ and T$_{22}(\theta)$, as well as the γ-ray polarization P$_\gamma(\theta)$, and the γ-ray polarization analyzing power A$_\gamma(\theta)$. For the case of P$_\gamma(\theta)$ and A$_\gamma(\theta)$ the data was acquired at E$_p$(lab) = 80-0 keV and no effort was made to extract the energy dependence due to the limited statistics. Six complex transition matrix elements, listed in Table 6.2, were fit to the observables and these TMEs were compared with *ab initio* three-body model calculations.

7.1 Discussion of Results

The experimental results of the measurements of ^{2}H($\vec{\mathrm{p}},\gamma$)^{3}He and ^{1}H($\vec{\mathrm{d}},\gamma$)^{3}He are contained in Chapter 6. The complete data set allowed us to determine the

TME of the reaction to a high degree of accuracy. The unconstrained fit of the six TMEs listed in Table 6.2 to the data set yields a χ^2/ν of 1.03. The quality of the fit allows accurate comparison with the theoretically determined TMEs. Most of the difference between the theory and experiment lies in the E1 s=3/2 terms which double in strength between theory and the fit to the data and have strikingly different phases. The phases of the other terms stay relatively close to theory, but the cross section fractions change substantially (see Table 6.11 and Table 6.5). This fit agrees well with all of the observables, with most of the error coming from the T_{20} data which has two data points that do not fall on the fitted curve. The fit has a ratio of the quartet to doublet M1 strength of 0.380 which does not agree well with theory.

After careful analysis, the values of the phases of the E1 s=3/2 TMEs have been determined to be the cause of the $A_y(\theta)$ puzzle for the $^2H(\vec{p},\gamma)^3He$ and $^1H(\vec{d},\gamma)^3He$ reactions. The changes in the phases of these relatively small TMEs, in terms of amplitudes, have large effects on the vector analyzing powers. In the case of three-body scattering the same effect has been seen for NN scattering in the s=1 p-wave terms. Further theoretical studies [Tor98b] are under way to try and determine the E1 s=3/2 terms' amplitudes and phases that are consistent with all of the observables including the vector analyzing powers. The other changes that occur in the E1 amplitudes are necessary to reproduce T_{20} accurately. It seems that the theory currently miscalculates the E1 terms in general and has the most trouble with the E1 s=3/2 terms. Several ideas have been put forth about the origin of this problem [Hüb98] including charge-independence breaking (CIB), charge-symmetry breaking (CSB), and the three-body force. In the paper [Hüb98], the CIB and CSB explanations are shown to be impossible and that all current three-body forces either have no effect or make the problem worse. The current three-body force models only contain the terms that are

considered to be the most important and easiest to calculate. The conclusion is that what is needed is a new three-body force with modified or new potentials, especially spin-orbit terms [Hüb98]. This needs to be verified with new calculations.

In an effort to achieve a TME fit to the data with a lower error, Watson's theorem was used to constrain the phases to be equal to those calculated by theory, except for the E1 s=3/2 terms, which do not seem to be well resolved by theory. This yields a χ^2/ν of 0.968 and a significant reduction in the error on the TMEs. This is the fit that is used to calculate all other quantities. This fit yields a quartet to doublet ratio of 0.49 ± 0.05 which is in excellent agreement with the AV18/IX calculation of 0.475. It also reproduces all of the data nearly as well as the completely unconstrained fit. The χ^2 is up from the free fit by about 1% except for T_{20} whose χ^2 drops by 2% compared to the unconstrained fit.

Using our fit to the data we were able to calculate the asymptotic D- to S-State ratio, η, from our $T_{20}(\theta)$ data. This parameter is related to the strength of the D-state in ^{3}He and provides information on the tensor force. η was determined previously for $^2\mathrm{H}(\vec{\mathrm{p}},\gamma)^3\mathrm{He}$ in [Ric97a] and was found to be $\eta = -0.0399 \pm 0.0091^{+0.0012}_{-0.0019}$. Another extraction of η using the distorted-wave Born approximation yielded $\eta = -0.0386 \pm 0.0046 \pm 0.0012$ [Aye95] while a full three-body calculation yielded $\eta = -0.0430 \pm 0.001$ [Fri88]. The value from our more detailed determination of the TMEs gave $\eta = -0.0340 \pm .0102^{+0.010}_{-0.015}$ agrees well with the other measurement and the theoretical calculation. This value's error is due to the large error on the s=3/2 TMEs phases.

Finally, our determination of the TMEs from the experimental data allowed us to calculate the Gerasimov-Drell-Hearn sum rule right above threshold for the $^3\vec{\mathrm{He}}(\vec{\gamma},\mathrm{d})\mathrm{H}$ reaction. This quantity relates the anomalous magnetic moment squared

to the integral of the difference in the cross section for the spin of the target and the γ-ray beam aligned and anti-aligned divided by the energy (see Equation 1.6). The derivation is based solely on the dispersion relation for forward Compton scattering, the optical theorem, and the low energy theorem. The anomalous magnetic moment, κ, is not only non-zero, but it is quite large in comparison to those of the nucleons and deuteron. The value of κ implies that the total integral will be equal to 496 μb and the integral below pion threshold is expected to be approximately 237 μb.

To calculate this value we assume that the *S*-factor is linear as a function of energy for both the E1 and the M1 components. This assumption is born out by the data from [Sch95, Sch97] as seen in Figure 6.5. The next assumption is that the M1 quartet to doublet ratio stays the same over our energy range, an assumption bolstered by the calculations of Viviani *et al.* [Viv96]. The E1 cross section ratios are assumed to stay constant with respect to the other E1 terms as a function of energy as well. These assumptions do not significantly affect the outcome of the calculation. When the cross section fractions for E1 s=1/2 and M1 terms were changed for the lower half of the integral from their fitted values by 20%, a 2.0% effect was seen in the calculated GDH sum rule.

These assumptions give us the cross section as a function of energy for each of the six TMEs. Using the principle of detailed balance we converted these TMEs to the TMEs of the $^3\vec{\mathrm{H}}\mathrm{e}(\vec{\gamma},\mathrm{d})\mathrm{H}$ reaction. This allowed us to calculate the GDH sum rule for the energies of our reaction, 40-0 keV. This means that the integral was performed from E_γ = 5.495 - 5.522 MeV. This yielded a value for the integral of -0.0906 $\pm$ 0.0123 nb. The full calculation yields a value of -0.050 nb which is about half the value of the fit to the data. Breaking up the integral to see the effect of the different TMEs, we see that the integral from the M1 and E1 s=3/2 terms are about the same for the

fit and theory. The integral calculated from the E1 s=1/2 terms is a factor of 3.6 greater for the fit to data than for the theory. Again it appears that the E1 terms are responsible for the difference between experiment and theory. The other important point is that both the fit to the data and the theory give a negative value for the integral while the total integral value of the sum-rule is supposed to be positive. That means the integral must become positive and larger at higher energies to make up for this negative contribution.

The final important piece of the GDH sum rule is given by the Impulse Approximation (IA) calculations, no two-body currents. The IA predicts a small value for the integral of 0.00073 nb. This is not too surprising because the IA does not describe any internal structure for the ground state. This result indicates that our experimentally determined value for the sum-rule integral from E_γ = 5.495 - 5.522 MeV is about 70 times larger than the value predicted in a nucleons-only theoretical model of ^{3}He. This is the most dramatic measurement of the effects of meson-exchange currents ever reported in nuclear physics.

7.2 Astrophysical Relevance

This new measurement of the ^{2}H(p, γ)^{3}He reaction reveals that the astrophysical *S*-factor at zero energy is reduced from the value obtained by [Gri63]. The old value has been used in calculations of protostellar evolution and the 34% reduction of this value from 0.25 $\pm$ 0.04 eV·b [Gri63] to 0.166 $\pm$ 0.005 eV·b [Sch97] has an effect on these calculations. The change in the *S*-factor has no effect on energy production in the solar proton-proton chain because the production of deuterium in the sun is bottlenecked by a weak reaction. On the other hand, in protostellar evolution it is

the first nuclear reaction to turn on and so it has a large influence on the development of a protostar.

Calculations of the evolution of a protostar are dependent on the interstellar deuterium to hydrogen (D/H) ratio. We make the reasonable assumption that the interstellar D/H ratio will scale with changes in the ^{2}H(p,γ)^{3}He reaction's S-factor [Sch97]. Taking the previously calculated interstellar D/H ratio of 2.5×10^{-5} [Sta88] and reducing it by 34% yields 1.7×10^{-5}. The calculations of protostellar evolution by [Sta88] were done for different D/H ratios. For a D/H ratio of 2.5×10^{-5}, there is a "thermostat effect" that keeps the temperature of the protostar constant and the radius of the protostar will grow with accreted mass. The calculation was also done for a D/H ratio of 1.3×10^{-5}, which is approximately 25% smaller than what our experiment implies. Nevertheless, it shows that between D/H ratio values of 2.5×10^{-5} and 1.3×10^{-5} a change in protostellar evolution takes place. For a D/H ratio of 1.3×10^{-5}, the star starts to contract with increasing mass after reaching a mass of about 0.7 solar masses. This destroys the "thermostat effect" and changes the calculated luminosity and temperature for protostars. Calculations using the new value of the interstellar D/H ratio from the our determination of the S-factor need to be completed to check if the "thermostat effect" exists in protostars.

7.3 In Closing

The measurement of ^{2}H($\vec{\text{p}}$,γ)^{3}He and ^{1}H($\vec{\text{d}}$,γ)^{3}He at E$_p$(lab) = 40-0 keV has revealed important and interesting physics. The data set collected in this experiment represents the most complete measurement of a three-body reaction at very low energy. The TMEs for this experiment have been determined accurately and provide a

test bed for theoretical three-body calculations. Interesting quantities and questions about the ^{3}He system have been determined and answered: the quartet to doublet M1 cross section ratio, the determination of the TMEs causing of the $A_y(\theta)$ puzzle in this system, the asymptotic D- to S-state ratio, and the GDH sum rule.

The knowledge culled from this experiment has been not only substantial, but surprising. It has helped to initiate further study of low energy capture reactions and three body systems. Hopefully, all of the experimental features will one day be well represented by nuclear theory.

Appendix A

Observable Equations

The analysis used the six Transition Matrix Elements that are listed in Table 6.2. The coefficients were calculated using the code "LS.FOR" which is available on the Sun and Vax clusters at TUNL. This code calculates the coefficients in the manner set forth in [Sey79]. A Clebsch-Gordon coefficient in the calculations restricts the value of k, the order of the Legendre Polynomial $P_k^q(\cos\theta)$, to $|L' - L| \leq k \leq |L' + L|$. Therefore, k can only take on values of 0, 1, or 2 for the TMEs given in Table 6.2.

A.1 Cross Section

Using Equation 6.1 and these six TMEs the formula for the cross section becomes

$$\sigma(\theta) = A_0 \left(a_0 + Q_1 a_1 P_1(\cos\theta) + Q_2 a_2 P_2(\cos\theta)\right). \tag{A.1}$$

The full expansion for the coefficients in the cross section are given by

$$a_0 = 2\left|{}^2p_2\right|^2 + 4\left|{}^2p_4\right|^2 + 2\left|{}^4p_2\right|^2 + 4\left|{}^4p_4\right|^2 + 2\left|{}^2s_2\right|^2 + 4\left|{}^4s_4\right|^2, \tag{A.2}$$

$$\begin{aligned} a_1 = &-4\left|{}^2s_2\right|\left|{}^2p_2\right|\cos(\phi_{{}^2s_2}-\phi_{{}^2p_2}) + 4\left|{}^2s_2\right|\left|{}^2p_4\right|\cos(\phi_{{}^2s_2}-\phi_{{}^2p_4}) \\ &- 2\sqrt{2}\left|{}^4s_4\right|\left|{}^4p_2\right|\cos(\phi_{{}^4s_4}-\phi_{{}^4p_2}) - 4\sqrt{5}\left|{}^4s_4\right|\left|{}^4p_4\right|\cos(\phi_{{}^4s_4}-\phi_{{}^4p_4}) \end{aligned} \quad (A.3)$$

and

$$\begin{aligned} a_2 = &-4\left|{}^2p_2\right|\left|{}^2p_4\right|\cos(\phi_{{}^2p_2}-\phi_{{}^2p_4}) + 2\sqrt{\frac{2}{5}}\left|{}^4p_2\right|\left|{}^4p_4\right|\cos(\phi_{{}^4p_2}-\phi_{{}^4p_4}) \\ &- 2\left|{}^2p_4\right|^2 + \frac{8}{5}\left|{}^4p_4\right|^2. \end{aligned} \quad (A.4)$$

A.2 iT_{11}

From Equation 6.6, the expansion of iT_{11} is

$$\frac{iT_{11}(\theta)\ \sigma(\theta)}{A_0} = Q_1 P_1^1(\cos\theta) b_1 + Q_2 P_2^1(\cos\theta) b_2. \quad (A.5)$$

The coefficients are given as follows

$$\begin{aligned} b_1 = &-4\left|{}^2s_2\right|\left|{}^2p_2\right|\sin(\phi_{{}^2s_2}-\phi_{{}^2p_2}) + \sqrt{2}\left|{}^2s_2\right|\left|{}^4p_2\right|\sin(\phi_{{}^2s_2}-\phi_{{}^4p_2}) \\ &- 2\left|{}^2s_2\right|\left|{}^2p_4\right|\sin(\phi_{{}^2s_2}-\phi_{{}^2p_4}) - \sqrt{5}\left|{}^2s_2\right|\left|{}^4p_4\right|\sin(\phi_{{}^2s_2}-\phi_{{}^4p_4}) \\ &+ \left|{}^4s_4\right|\left|{}^2p_2\right|\sin(\phi_{{}^4s_4}-\phi_{{}^2p_2}) - \frac{5}{2}\sqrt{2}\left|{}^4s_4\right|\left|{}^4p_2\right|\sin(\phi_{{}^4s_4}-\phi_{{}^4p_2}) \\ &+ 5\left|{}^4s_4\right|\left|{}^2p_4\right|\sin(\phi_{{}^4s_4}-\phi_{{}^2p_4}) - 2\sqrt{5}\left|{}^4s_4\right|\left|{}^4p_4\right|\sin(\phi_{{}^4s_4}-\phi_{{}^4p_4}) \end{aligned} \quad (A.6)$$

and

$$\begin{aligned} b_2 = &\ 2\left|{}^2p_2\right|\left|{}^2p_4\right|\sin(\phi_{{}^2p_2}-\phi_{{}^2p_4}) + \frac{2}{\sqrt{5}}\left|{}^2p_2\right|\left|{}^4p_4\right|\sin(\phi_{{}^2p_2}-\phi_{{}^4p_4}) \\ &- \frac{1}{\sqrt{2}}\left|{}^4p_2\right|\left|{}^2p_4\right|\sin(\phi_{{}^4p_2}-\phi_{{}^2p_4}) - \frac{1}{\sqrt{10}}\left|{}^4p_2\right|\left|{}^4p_4\right|\sin(\phi_{{}^4p_2}-\phi_{{}^4p_4}) \\ &+ \frac{3}{\sqrt{5}}\left|{}^2p_4\right|\left|{}^4p_4\right|\sin(\phi_{{}^2p_4}-\phi_{{}^4p_4}). \end{aligned} \quad (A.7)$$

A.3 T_{20}

Equation 6.7 gives

$$\frac{T_{20}(\theta)\ \sigma(\theta)}{A_0} = c_0 + Q_1 P_1(\cos\theta) c_1 + Q_2 P_2(\cos\theta) c_2. \tag{A.8}$$

The coefficients are given as follows

$$\begin{aligned} c_0 = {} & 4\left|{}^2p_2\right|\left|{}^4p_2\right|\cos(\phi_{{}^2p_2} - \phi_{{}^4p_2}) - \sqrt{2}\left|{}^4p_2\right|^2 \\ & - 4\sqrt{\frac{2}{5}}\left|{}^2p_4\right|\left|{}^4p_4\right|\cos(\phi_{{}^2p_4} - \phi_{{}^4p_4}) + \frac{8}{5}\sqrt{2}\left|{}^4p_4\right|^2, \end{aligned} \tag{A.9}$$

$$\begin{aligned} c_1 = {} & -4\left|{}^2s_2\right|\left|{}^4p_2\right|\cos(\phi_{{}^2s_2} - \phi_{{}^4p_2}) - 2\sqrt{\frac{2}{5}}\left|{}^2s_2\right|\left|{}^4p_4\right|\cos(\phi_{{}^2s_2} - \phi_{{}^4p_4}) \\ & - 2\sqrt{2}\left|{}^4s_4\right|\left|{}^2p_2\right|\cos(\phi_{{}^4s_4} - \phi_{{}^2p_2}) + 2\left|{}^4s_4\right|\left|{}^4p_2\right|\cos(\phi_{{}^4s_4} - \phi_{{}^4p_2}) \\ & + 2\sqrt{2}\left|{}^4s_4\right|\left|{}^2p_4\right|\cos(\phi_{{}^4s_4} - \phi_{{}^2p_4}) - 8\sqrt{\frac{2}{5}}\left|{}^4s_4\right|\left|{}^4p_4\right|\cos(\phi_{{}^4s_4} - \phi_{{}^4p_4}), \end{aligned} \tag{A.10}$$

and

$$\begin{aligned} c_2 = {} & 2\sqrt{2}\left|{}^2s_2\right|\left|{}^4s_4\right|\cos(\phi_{{}^2s_2} - \phi_{{}^4s_4}) + \sqrt{2}\left|{}^4s_4\right|^2 \\ & + 2\sqrt{\frac{2}{5}}\left|{}^2p_2\right|\left|{}^4p_4\right|\cos(\phi_{{}^2p_2} - \phi_{{}^4p_4}) - 4\left|{}^4p_2\right|\left|{}^2p_4\right|\cos(\phi_{{}^4p_2} - \phi_{{}^2p_4}) \\ & - \frac{2}{\sqrt{5}}\left|{}^4p_2\right|\left|{}^4p_4\right|\cos(\phi_{{}^4p_2} - \phi_{{}^4p_4}) + 2\sqrt{\frac{2}{5}}\left|{}^2p_4\right|\left|{}^4p_4\right|\cos(\phi_{{}^2p_4} - \phi_{{}^4p_4}) + \sqrt{2}\left|{}^4p_4\right|^2. \end{aligned} \tag{A.11}$$

A.4 T_{21}

In the same way, Equation 6.8 yields

$$\frac{T_{21}(\theta)\ \sigma(\theta)}{A_0} = Q_1 P_1^1(\cos\theta) d_1 + Q_2 P_2^1(\cos\theta) d_2. \tag{A.12}$$

The expansion of the coefficients are given by

$$\begin{aligned} \mathrm{d}_1 = {} & 2\sqrt{6}\left|{}^2\mathrm{s}_2\right|\left|{}^4\mathrm{p}_2\right|\cos(\phi_{{}^2\mathrm{s}_2}-\phi_{{}^4\mathrm{p}_2}) + 2\sqrt{\frac{3}{5}}\left|{}^2\mathrm{s}_2\right|\left|{}^4\mathrm{p}_4\right|\cos(\phi_{{}^2\mathrm{s}_2}-\phi_{{}^4\mathrm{p}_4}) \\ & + 2\sqrt{3}\left|{}^4\mathrm{s}_4\right|\left|{}^2\mathrm{p}_2\right|\cos(\phi_{{}^4\mathrm{s}_4}-\phi_{{}^2\mathrm{p}_2}) - \sqrt{6}\left|{}^4\mathrm{s}_4\right|\left|{}^4\mathrm{p}_2\right|\cos(\phi_{{}^4\mathrm{s}_4}-\phi_{{}^4\mathrm{p}_2}) \\ & - 2\sqrt{3}\left|{}^4\mathrm{s}_4\right|\left|{}^2\mathrm{p}_4\right|\cos(\phi_{{}^4\mathrm{s}_4}-\phi_{{}^2\mathrm{p}_4}) + 4\sqrt{\frac{12}{5}}\left|{}^4\mathrm{s}_4\right|\left|{}^4\mathrm{p}_4\right|\cos(\phi_{{}^4\mathrm{s}_4}-\phi_{{}^4\mathrm{p}_4}) \end{aligned} \quad \text{(A.13)}$$

and

$$\begin{aligned} \mathrm{d}_2 = {} & -\frac{4}{\sqrt{3}}\left|{}^2\mathrm{s}_2\right|\left|{}^4\mathrm{s}_4\right|\cos(\phi_{{}^2\mathrm{s}_2}-\phi_{{}^4\mathrm{s}_4}) - \frac{2}{\sqrt{3}}\left|{}^4\mathrm{s}_4\right|^2 \\ & + \sqrt{6}\left|{}^4\mathrm{p}_2\right|\left|{}^2\mathrm{p}_4\right|\cos(\phi_{{}^4\mathrm{p}_2}-\phi_{{}^2\mathrm{p}_4}) + \sqrt{\frac{6}{5}}\left|{}^4\mathrm{p}_2\right|\left|{}^4\mathrm{p}_4\right|\cos(\phi_{{}^4\mathrm{p}_2}-\phi_{{}^4\mathrm{p}_4}) \\ & - 2\sqrt{\frac{3}{5}}\left|{}^2\mathrm{p}_4\right|\left|{}^4\mathrm{p}_4\right|\cos(\phi_{{}^2\mathrm{p}_4}-\phi_{{}^4\mathrm{p}_4}) - \frac{2\sqrt{3}}{5}\left|{}^4\mathrm{p}_4\right|^2. \end{aligned} \quad \text{(A.14)}$$

A.5 $\mathbf{T_{22}}$

As in the previous section, Equation 6.9 gives

$$\frac{\mathrm{T}_{22}(\theta)\ \sigma(\theta)}{\mathrm{A}_0} = \mathrm{Q}_2\mathrm{P}_2^2(\cos\theta)\mathrm{e}_2 \quad \text{(A.15)}$$

and the coefficient is as follows

$$\begin{aligned} \mathrm{e}_2 = {} & \frac{2}{\sqrt{3}}\left|{}^2\mathrm{s}_2\right|\left|{}^4\mathrm{s}_4\right|\cos(\phi_{{}^2\mathrm{s}_2}-\phi_{{}^4\mathrm{s}_4}) + \frac{2}{\sqrt{12}}\left|{}^4\mathrm{s}_4\right|^2 \\ & - 2\sqrt{\frac{3}{5}}\left|{}^2\mathrm{p}_2\right|\left|{}^4\mathrm{p}_4\right|\cos(\phi_{{}^2\mathrm{p}_2}-\phi_{{}^4\mathrm{p}_4}) - 2\sqrt{\frac{3}{10}}\left|{}^4\mathrm{p}_2\right|\left|{}^4\mathrm{p}_4\right|\cos(\phi_{{}^4\mathrm{p}_2}-\phi_{{}^4\mathrm{p}_4}) \\ & - \frac{\sqrt{3}}{5}\left|{}^4\mathrm{p}_4\right|^2. \end{aligned} \quad \text{(A.16)}$$

A.6 $\mathbf{A}_y$

Finally, Equation 6.5 and these TMEs gives

$$\frac{\mathrm{A}_y(\theta)\ \sigma(\theta)}{\mathrm{A}_0} = \mathrm{Q}_1\mathrm{P}_1^1(\cos\theta)\mathrm{z}_1 + \mathrm{Q}_2\mathrm{P}_2^1(\cos\theta)\mathrm{z}_2 \tag{A.17}$$

and the coefficients are calculated to be

$$\begin{aligned}
\mathrm{z}_1 = &-\frac{4}{3}\left|{}^2\mathrm{s}_2\right|\left|{}^2\mathrm{p}_2\right|\sin(\phi_{{}^2\mathrm{s}_2} - \phi_{{}^2\mathrm{p}_2}) + 4\frac{\sqrt{2}}{3}\left|{}^2\mathrm{s}_2\right|\left|{}^4\mathrm{p}_2\right|\sin(\phi_{{}^2\mathrm{s}_2} - \phi_{{}^4\mathrm{p}_2}) \\
&- \frac{2}{3}\left|{}^2\mathrm{s}_2\right|\left|{}^2\mathrm{p}_4\right|\sin(\phi_{{}^2\mathrm{s}_2} - \phi_{{}^2\mathrm{p}_4}) - \frac{4\sqrt{5}}{3}\left|{}^2\mathrm{s}_2\right|\left|{}^4\mathrm{p}_4\right|\sin(\phi_{{}^2\mathrm{s}_2} - \phi_{{}^4\mathrm{p}_4}) \\
&+ \frac{4}{3}\left|{}^4\mathrm{s}_4\right|\left|{}^2\mathrm{p}_2\right|\sin(\phi_{{}^4\mathrm{s}_4} - \phi_{{}^2\mathrm{p}_2}) + \frac{5\sqrt{2}}{3}\left|{}^4\mathrm{s}_4\right|\left|{}^4\mathrm{p}_2\right|\sin(\phi_{{}^4\mathrm{s}_4} - \phi_{{}^4\mathrm{p}_2}) \\
&+ \frac{20}{3}\left|{}^4\mathrm{s}_4\right|\left|{}^2\mathrm{p}_4\right|\sin(\phi_{{}^4\mathrm{s}_4} - \phi_{{}^2\mathrm{p}_4}) + \frac{4\sqrt{5}}{3}\left|{}^4\mathrm{s}_4\right|\left|{}^4\mathrm{p}_4\right|\sin(\phi_{{}^4\mathrm{s}_4} - \phi_{{}^4\mathrm{p}_4})
\end{aligned} \tag{A.18}$$

and

$$\begin{aligned}
\mathrm{z}_2 = &\frac{2}{3}\left|{}^2\mathrm{p}_2\right|\left|{}^2\mathrm{p}_4\right|\sin(\phi_{{}^2\mathrm{p}_2} - \phi_{{}^2\mathrm{p}_4}) + \frac{8}{3\sqrt{5}}\left|{}^2\mathrm{p}_2\right|\left|{}^4\mathrm{p}_4\right|\sin(\phi_{{}^2\mathrm{p}_2} - \phi_{{}^4\mathrm{p}_4}) \\
&- \frac{2\sqrt{2}}{3}\left|{}^4\mathrm{p}_2\right|\left|{}^2\mathrm{p}_4\right|\sin(\phi_{{}^4\mathrm{p}_2} - \phi_{{}^2\mathrm{p}_4}) + \frac{2}{3\sqrt{10}}\left|{}^4\mathrm{p}_2\right|\left|{}^4\mathrm{p}_4\right|\sin(\phi_{{}^4\mathrm{p}_2} - \phi_{{}^4\mathrm{p}_4}) \\
&+ \frac{4}{\sqrt{5}}\left|{}^2\mathrm{p}_4\right|\left|{}^4\mathrm{p}_4\right|\sin(\phi_{{}^2\mathrm{p}_4} - \phi_{{}^4\mathrm{p}_4}).
\end{aligned} \tag{A.19}$$

Appendix B

γ-Ray Observable Equations

The γ-ray polarization as a function of proton polarization is more difficult to define and we have written a paper [Wul99] that deals with this topic. From this paper the polarization of the γ-ray in terms of the six TMEs given in Table 6.2 are calculated and given by:

$$\mathrm{P}_\gamma(\theta) = -2\sqrt{\frac{5}{3}} \left(\frac{\mathrm{f}_2 \mathrm{P}_2^2(\cos\theta) + \frac{f}{\sqrt{6}} \left[\mathrm{P}_1^1(\cos\theta)\mathrm{g}_1 + \mathrm{P}_2^1(\cos\theta)\mathrm{g}_2 \right]}{\frac{1}{2} \left(\mathrm{a}_0 + \mathrm{P}_1(\cos\theta)\mathrm{a}_1 + \mathrm{P}_2(\cos\theta)\mathrm{a}_2 \right) + \frac{f}{\sqrt{6}} \left[\mathrm{P}_1^1(\cos\theta)\mathrm{h}_1 + \mathrm{P}_2^1(\cos\theta)\mathrm{h}_2 \right]} \right) \tag{B.1}$$

where f is the polarization of the proton beam, the a_k coefficients are from Equation A.1 for the cross section and the coefficients f_2, g_k, and h_k are given below. Equation B.1 can be used to calculate the γ-ray polarization for an unpolarized beam, $\mathrm{P}_\gamma^0(\theta)$, by setting $f = 0$. To calculate $\mathrm{A}_\gamma(\theta)$ one takes the difference between two versions of Equation B.1, one with $f = 1$ and the other with $f = -1$.

The coefficient f_2 is given by

$$\mathrm{f}_2 = \frac{1}{5}\sqrt{\frac{3}{8}}\left[-\sqrt{10}\left|{}^2\mathrm{p}_2\right|\left|{}^2\mathrm{p}_4\right|\cos(\phi_{{}^2\mathrm{p}_2}-\phi_{{}^2\mathrm{p}_4}) - \sqrt{\frac{5}{2}}\left|{}^2\mathrm{p}_4\right|^2 + \left|{}^4\mathrm{p}_2\right|\left|{}^4\mathrm{p}_4\right|\cos(\phi_{{}^4\mathrm{p}_2}-\phi_{{}^4\mathrm{p}_4}) + 2\sqrt{\frac{2}{5}}\left|{}^4\mathrm{p}_4\right|^2\right]. \quad \text{(B.2)}$$

The coefficients g_k are given by

$$\begin{aligned}\mathrm{g}_1 = 3\Bigg[&-\frac{2}{\sqrt{10}}\left|{}^2\mathrm{p}_2\right|\left|{}^4\mathrm{s}_4\right|\sin(\phi_{{}^2\mathrm{p}_2}-\phi_{{}^4\mathrm{s}_4}) \\ &-\frac{1}{\sqrt{10}}\left|{}^2\mathrm{p}_4\right|\left|{}^2\mathrm{s}_2\right|\sin(\phi_{{}^2\mathrm{p}_4}-\phi_{{}^2\mathrm{s}_2}) - \frac{2}{\sqrt{10}}\left|{}^2\mathrm{p}_4\right|\left|{}^4\mathrm{s}_4\right|\sin(\phi_{{}^2\mathrm{p}_4}-\phi_{{}^4\mathrm{s}_4}) \\ &-\frac{1}{2\sqrt{5}}\left|{}^4\mathrm{p}_2\right|\left|{}^4\mathrm{s}_4\right|\sin(\phi_{{}^4\mathrm{p}_2}-\phi_{{}^4\mathrm{s}_4}) - \frac{\sqrt{2}}{5}\left|{}^4\mathrm{p}_4\right|\left|{}^2\mathrm{s}_2\right|\sin(\phi_{{}^4\mathrm{p}_4}-\phi_{{}^2\mathrm{s}_2}) \\ &-\frac{2\sqrt{2}}{5}\left|{}^4\mathrm{p}_4\right|\left|{}^4\mathrm{s}_4\right|\sin(\phi_{{}^4\mathrm{p}_4}-\phi_{{}^4\mathrm{s}_4})\Bigg] \quad \text{(B.3)}\end{aligned}$$

and

$$\begin{aligned}\mathrm{g}_2 = &-\frac{1}{\sqrt{10}}\left|{}^2\mathrm{p}_2\right|\left|{}^2\mathrm{p}_4\right|\sin(\phi_{{}^2\mathrm{p}_2}-\phi_{{}^2\mathrm{p}_4}) \\ &+\frac{2\sqrt{2}}{5}\left|{}^2\mathrm{p}_2\right|\left|{}^4\mathrm{p}_4\right|\sin(\phi_{{}^2\mathrm{p}_2}-\phi_{{}^4\mathrm{p}_4}) + \frac{1}{\sqrt{5}}\left|{}^2\mathrm{p}_4\right|\left|{}^4\mathrm{p}_2\right|\sin(\phi_{{}^2\mathrm{p}_4}-\phi_{{}^4\mathrm{p}_2}) \\ &+\frac{3\sqrt{2}}{5}\left|{}^2\mathrm{p}_4\right|\left|{}^4\mathrm{p}_4\right|\sin(\phi_{{}^2\mathrm{p}_4}-\phi_{{}^4\mathrm{p}_4}) - \frac{1}{10}\left|{}^4\mathrm{p}_2\right|\left|{}^4\mathrm{p}_4\right|\sin(\phi_{{}^4\mathrm{p}_2}-\phi_{{}^4\mathrm{p}_4}). \quad \text{(B.4)}\end{aligned}$$

The coefficients h_k are given by

$$\begin{aligned}\mathrm{h}_1 = \frac{1}{\sqrt{6}}\Bigg[&4\left|{}^2\mathrm{p}_2\right|\left|{}^2\mathrm{s}_2\right|\sin(\phi_{{}^2\mathrm{p}_2}-\phi_{{}^2\mathrm{s}_2}) \\ &+4\left|{}^2\mathrm{p}_2\right|\left|{}^4\mathrm{s}_4\right|\sin(\phi_{{}^2\mathrm{p}_2}-\phi_{{}^4\mathrm{s}_4}) + 2\left|{}^2\mathrm{p}_4\right|\left|{}^2\mathrm{s}_2\right|\sin(\phi_{{}^2\mathrm{p}_4}-\phi_{{}^2\mathrm{s}_2}) \\ &+20\left|{}^2\mathrm{p}_4\right|\left|{}^4\mathrm{s}_4\right|\sin(\phi_{{}^2\mathrm{p}_4}-\phi_{{}^4\mathrm{s}_4}) + 4\sqrt{2}\left|{}^4\mathrm{p}_2\right|\left|{}^2\mathrm{s}_2\right|\sin(\phi_{{}^4\mathrm{p}_2}-\phi_{{}^2\mathrm{s}_2}) \\ &-\frac{10}{\sqrt{2}}\left|{}^4\mathrm{p}_2\right|\left|{}^4\mathrm{s}_4\right|\sin(\phi_{{}^4\mathrm{p}_2}-\phi_{{}^4\mathrm{s}_4}) - 4\sqrt{5}\left|{}^4\mathrm{p}_4\right|\left|{}^2\mathrm{s}_2\right|\sin(\phi_{{}^4\mathrm{p}_4}-\phi_{{}^2\mathrm{s}_2}) \\ &-4\sqrt{5}\left|{}^4\mathrm{p}_4\right|\left|{}^4\mathrm{s}_4\right|\sin(\phi_{{}^4\mathrm{p}_4}-\phi_{{}^4\mathrm{s}_4})\Bigg] \quad \text{(B.5)}\end{aligned}$$

and

$$\begin{aligned} \mathrm{h}_2 = \frac{1}{\sqrt{6}} \Bigg[& 2 \left|{}^2\mathrm{p}_2\right| \left|{}^2\mathrm{p}_4\right| \sin(\phi_{{}^2\mathrm{p}_2} - \phi_{{}^2\mathrm{p}_4}) \\ & - \frac{8}{\sqrt{5}} \left|{}^2\mathrm{p}_2\right| \left|{}^4\mathrm{p}_4\right| \sin(\phi_{{}^2\mathrm{p}_2} - \phi_{{}^4\mathrm{p}_4}) - \frac{4}{\sqrt{2}} \left|{}^2\mathrm{p}_4\right| \left|{}^4\mathrm{p}_2\right| \sin(\phi_{{}^2\mathrm{p}_4} - \phi_{{}^4\mathrm{p}_2}) \\ & - \frac{12}{\sqrt{5}} \left|{}^2\mathrm{p}_4\right| \left|{}^4\mathrm{p}_4\right| \sin(\phi_{{}^2\mathrm{p}_4} - \phi_{{}^4\mathrm{p}_4}) \\ & + \frac{2}{\sqrt{10}} \left|{}^4\mathrm{p}_2\right| \left|{}^4\mathrm{p}_4\right| \sin(\phi_{{}^4\mathrm{p}_2} - \phi_{{}^4\mathrm{p}_4}) \Bigg] . \end{aligned} \tag{B.6}$$

Bibliography

[Ack98] K. Ackerstaff et al. Phys. Lett. B, **444**(1998) 531.

[Alv57] L. W. Alvarez et al. Phys. Rev., **105**(1957) 1127.

[And77] D. A. Andrews and G. Newton. J. Phys. D, **10**(1977) 845.

[Are88] H. Arenhövel, G. Kreβ, R. Schmidt, and P. Wilhelm. Nucl. Phys., **A631**(1988) 612.

[Arr84] A. Arriaga and F. D. Santos. Phys. Rev. C, **39**(1984) 1945.

[Aye95] Z. Ayer, H. J. Karwowski, B. Kozlowska, and E. J. Ludwig. Phys. Rev. C, **52**(1995) 2851.

[Bas72] R. Bass, S. Brinkmann, C. von Charzewski, and H. Hanle. NIM, **104**(1972) 33.

[Bet50] H. A. Bethe and C. Longmire. Phys. Rev., **77**(1950) 647.

[BH71] H. H. Barschall and W. Haeberli, editors. *Polarization Phenomena in Nuclear Reactions*, page xxv. University of Wisconson Press, Madison, Wisconsin, 1971.

[Bra69] B. H. Bransden and C. J. Joachain. *Introduction to Quantum Mechanics.* Longman Scientific & Technical, New York, 1969.

[Bro90] R. E. Brown and N. Jarmie. Phys. Rev. C, **41**(1990) 1391.

[Che91] C. R. Chen, C. L. Payne, J. L. Friar, and B. F. Gibson. Phys. Rev. C, **44**(1991) 50.

[Cle90] T. B. Clegg. Rev. Sci. Instr., **61**(1990) 385.

[Coe83] H. T. Coelho, T. K. Das, and M. R. Robilotta. Phys. Rev. C, **28**(1983) 1812.

[Coh60] S. Cohen, D. L. Judd, and R. J. Riddell. Phys. Rev., **119**(1960) 384.

[Del72] L. M. Delves. In M. Baranger, editor, *Advances in Nuclear Physics*, volume 5, pages 1–224. Plenum Press, New York, 1972.

[Dre66] S. D. Drell and A. C. Hearn. Phys. Rev. Lett., **16**(1966) 908.

[Eis85] R. Eisberg and R. Resnick. *Quantum Physics of Atoms....* John Wiley & Sons, New York, 1985.

[Eva55] R. D. Evans. *The Atomic Nucleus.* McGraw-Hill, New York, 1955.

[Fad60] L. D. Faddeev. Zh. Eksp. Teor. FIz., **39**(1960) 1459.

[Fer65] A. J. Ferguseon. *Angular Correlation Methods in Gamma-Ray Spectroscopy.* John Wiley & Sons, New York, 1965.

[Fol57] L. L. Foldy and W. Tobocman. Phys. Rev., **105**(1957) 1099.

[Fra47] F. C. Frank. Nature (London), **160**(1947) 525.

[Fri82] J. L. Friar, B. F. Gibson, D. R. Lehman, and G. L. Payne. Phys. Rev. C, **25**(1982) 1616.

[Fri88] J. L. Friar, B. F. Gibson, D. R. Lehman, and G. L. Payne. Phys. Rev. C, **37**(1988) 2859.

[Fri90] J. L. Friar, B. F. Gibson, and G. L. Payne. Phys. Lett., **B251**(1990) 11.

[Fri91] J. L. Friar, B. F. Gibson, H. C. Jean, and G. L. Payne. Phys. Rev. Lett., **66**(1991) 1827.

[Ger61] S. S. Gerstein. Sov. Phys. JETP, **13**(1961) 488.

[Ger66] S. B. Gerasimov. Sov. J. Nucl. Phys., **2**(1966) 430.

[Gib84] B. F. Gibson and D. R. Lehman. Phys. Rev. C, **29**(1984) 1017.

[Gri63] G. M. Griffiths, E. A. Larson, and L. P. Robertson. Can. Journ. Phys., **41**(1963) 724.

[Hay70] E. Hayward. *Photonuclear Reactions.* Center for Radiation Research, National Bureau of Standards Monograph, 1970.

[Hüb98] D. Hüber and J. L. Friar. Phys. Rev. C, **58**(1998) 674.

[Jam71] F. James and M. Roos. *MINUIT*. CERN Computer Centre Program Library, 1971.

[Jur82] E. T. Jurney, P. J. Bendt, and J. C. Browne. Phys. Rev. C, **25**(1982) 2810.

[Kie93] A. Kievsky, M. Viviani, and S. Rosati. Nucl. Phys., **A551**(1993) 241.

[Kie94] A. Kievsky, M. Viviani, and S. Rosati. Nucl. Phys., **A557**(1994).

[Kie95] A. Kievsky, M. Viviani, and S. Rosati. Phys. Rev. C, **52**(1995) R15.

[Kie96] A. Kievsky, S. Rosati, W. Tornow, and M. Viviani. Nucl. Phys., **A607**(1996) 402.

[Kie98] A. Kievsky, M. Viviani, S. Rosati, D. Hüber, W. Glöckle, H. Kamada, H. Witala, and J. Golak. Phys. Rev. C, **58**(1998) 3085.

[Kin83] S. E. King et al. Phys. Rev. Lett., **51**(1983) 877.

[Knu99] L. D. Knutson. Phys. Rev. C, **59**(1999) 2152.

[Kra92] L. H. Kramer. Ph.D. thesis, Duke University, 1992.

[Lit70] A. E. Litherland, G. T. Ewan, and S. T. Lam. Can. Journ. Phys., **48**(1970) 2320.

[Mac87] R. Machleidt, K. Holinde, and Ch. Elster. Phys. Rep., **149**(1987) 1.

[Mac89] R. Machleidt. Adv. Nucl. Phys., **19**(1989) 189.

[Mat61] A. V. Matveenko and L. I. Ponomarev. Zh. Eksp. Teor. FIz., **13**(1961) 488.

[McA94] J. E. McAninch, L. O. Lamm, and W. Haeberli. Phys. Rev. C, **50**(1994) 589.

[Ohl73] G. G. Ohlsen and P. W. Keaton. NIM, **109**(1973) 41.

[Pay86] G. L. Payne. *Faddeev Equations for Bound and Scattering States.* In *Theoretical and Experimental Investigations of Hadronic Few-Body Systems*, page 53, 1986.

[Pet91] C. Petitjean et al. Muon Catal. Fusion, **5/6**(1990/91) 199.

[Phi87] R. J. Philpott. NIM, **A259**(1987) 317–323.

[Pud95] B. S. Pudliner et al. Phys. Rev. Lett., **74**(1995) 4396.

[Ric97a] B. J. Rice and H. R. Weller. Phys. Rev. C, **55**(1997) 2700.

[Ric97b] B. J. Rice, E. A. Wulf, R. S. Canon, J. H. Kelley, R. M. Prior, M. Spraker, D. R. Tilley, and H. R. Weller. Phys. Rev. C, **56**(1997) 2917.

[Rol88] C. E. Rolfs and W. S. Rodney. *Cauldrons in the Cosmos.* University of Chicago Press, Chicago, 1988.

[Ros53] M. E. Rose. Phys. Rev., **91**(1953) 610.

[Sch92] R. Schiavilla, R. B. Wiringa, V. R. Pandharipande, and J. Carlson. Phys. Rev. C, **52**(1992) 242.

[Sch95] G. J. Schmid. Ph.D. thesis, Duke University, 1995.

[Sch96a] G. Schmid et al. Phys. Rev. Lett., **76**(1996) 3088.

[Sch96b] G. J. Schmid, R. M Chastler, C. M. Laymon, H. R. Weller, R. M. Prior, and D. R. Tilley. Nucl. Phys., **A607**(1996) 139.

[Sch97] G. J. Schmid, B. J. Rice, R. M Chastler, M. A. Godwin, G C. Kiang, L. L. Kiang, C. M. Laymon, R. M. Prior, D. R. Tilley, and H. R. Weller. Phys. Rev. C, **56**(1997) 2565.

[Sey79] R. G. Seyler and H. R. Weller. Phys. Rev. C, **20**(1979) 453.

[Shi95] S. Shimizu, H. Nakamura K. Sagara, K. Maeda, T. Miwa, N. Nishimori S. Ueno, T. Nakashima, and Morinobu. Phys. Rev. C, **52**(1995) 1193.

[Sta88] S. W. Stahler. The Astrophysical Journal, **322**(1988) 804.

[Tor83] J. Torre and B. Goulard. Phys. Rev. C, **28**(1983) 529.

[Tor98a] W. Tornow and H. Witala. Nucl. Phys., **A637**(1998) 280.

[Tor98b] W. Tornow, H. Witala, and A. Kievsky. Phys. Rev. C, **57**(1998) 555.

[Vet85] M. C. Vetterli. Ph.D. thesis, McMaster University, 1985.

[Viv96] M. Viviani, R. Schiavilla, and A. Kievsky. Phys. Rev. C, **54**(1996) 534.

[Wat54] K. M. Watson. Phys. Rev., **95**(1954) 228.

[Wel88] H. R. Weller and D. R. Lehman. Ann. Rev. Nucl. Sci., **38**(1988) 563.

[Wel94] H. R. Weller, R. M. Chasteler, B. S. Marks, R. G. Seyler, and D. R. Lehman. Atomic Data and Nucl. Data Tables, **58**(1994) 219.

[Wil74] J. R. Williams. Ph.D. thesis, North Carolina State University, 1974.

[Wir84] R. B. Wiringa, R. A. Smith, and T. L. Ainsworth. Phys. Rev. C, **29**(1984) 1207.

[Wir91] R. B. Wiringa. Phys. Rev. C, **43**(1991) 1585.

[Wir95] R. B. Wiringa, V. G. J. Stoks, and R. Schiavilla. Phys. Rev. C, **51**(1995) 38.

[Wol49] L. Wolfenstein. Phys. Rev., **75**(1949) 1664.

[Wul99] E. A. Wulf, J. Guillemette, R. G. Seyler, and H. R. Weller. Atomic Data and Nucl. Data Tables, **79**(1999) *to be published.*

Biography

Eric Alan Wulf

Personal

- Born in Fairfax, VA on July 16, 1971

Education

- B.S. Physics, University of Virginia, Charlottesville, Virginia, 1993
- A.M. Physics, Duke University, Durham, North Carolina, 1996

Positions

- Research Assistant, Naval Research Lab, Summers 1988-1991
- Research Assistant, University of Virginia, Nuclear Physics, 1992-1993
- Teaching Assistant, Duke University, 1993-1995
- Research Assistant, Duke University, High Energy Physics, Summer 1994
- Research Assistant, Duke University, TUNL, 1995-1999

Publications

Direct determination of the doublet and quartet M1 cross sections in p-d radiative capture at near-thermal energies
B. J. Rice, E. A. Wulf, R. S. Canon, J. H. Kelley, R. M. Prior, M. Spraker, D. R. Tilley, and H. R. Weller. Phys. Rev. C, **56**(1997) 2917.

Angular Distribution Coefficients for γ-ray Polarizations Produced in Polarized Capture Reactions
E. A. Wulf, J. Guillemette, R. G. Seyler, and H. R. Weller. Atomic Data and Nucl. Data Tables, **79**(1999) *to be published.*

Astrophysical S factors for the $^{9}\mathrm{Be}(\vec{\mathrm{p}},\gamma)^{10}\mathrm{B}$ *reaction*
E. A. Wulf, M. A. Godwin, J. F. Guillemette, C. M. Laymon, R. M. Prior, B. J. Rice, M. Spraker, D. R. Tilley and H. R. Weller. Phys. Rev. C, **58**(1998) 517.